
Self-Assembly and Self-Organization of Magnetic Janus-like Colloids in Three Dimensions

- A Computer Simulation Study -

VORGELEGT VON:
DIPLOMPHYSIKERIN
ARZU BAHAR YENER
AUS
ÇORUM (TÜRKEI)

*Von der Fakultät II – Mathematik und Naturwissenschaften
der Technischen Universität Berlin
zur Erlangung des akademischen Grades
Doktor der Naturwissenschaften
Dr. rer. nat.*

genehmigte Dissertation

PROMOTIONS-AUSSCHUSS:

Vorsitzende:

1. Gutachterin:

2. Gutachter:

PROF. DR. MARIA KRIKUNOVA

PROF. DR. SABINE H. L. KLAPP

DR. PATRICK ILG

TAG DER WISSENSCHAFTLICHEN AUSSPRACHE: 01.11.2016

Berlin
2017

Declaration of Authorship

Ich versichere hiermit eidesstattlich, dass die vorliegende Dissertation selbständig verfasst wurde, die benutzten Hilfsmittel und Quellen korrekt aufgeführt sind und im Falle von Co-Autorenschaft die Darstellung des Eigenanteils zutreffend ist.

Danksagung

An erster Stelle bedanke ich mich herzlich bei meiner Betreuerin Prof. Dr. Sabine H. L. Klapp, ohne deren Engagement und Unterstützung diese Arbeit nicht entstanden wäre. Sie führte mich in das Forschungsgebiet über komplexe Fluide und Computersimulationen ein und begleitete mich wegweisend während meiner Promotion stets mit konstruktiver Kritik, Lob und unerschöpflicher Motivation. Dank ihrer wertvollen fachlichen Beiträge war sie für mich stets der Ausweg aus scheinbar aussichtslosen Situationen.

Weiterhin möchte ich mich bei Dr. Patrick Ilg bedanken, für seine unkomplizierte Bereitschaft und Zeit, diese Arbeit zu bewerten.

Mein Dank gilt ebenfalls Prof. Dr. Christian Holm und Dr. Rudolf Weeber für die unterstützende Diskussion zu den Bewegungsgleichungen der in dieser Arbeit betrachteten Teilchen.

Erleuchtende Diskussionen mit meinem Bürokollegen Dr. Florian Kogler, mit Dr. Rodrigo Lugo Frias, Dr. Stavros Peroukidis, Dr. Thomas Heinemann, Dr. Nicola Kleppmann und Dr. Robert Gernert gaben mir wertvolle Anstöße für meine Arbeit, für die ich mich ebenfalls herzlich bedanke. Die Arbeit in der AG Klapp "Computersimulationen und Theorie komplexer Fluide" hat mir große Freude bereitet und ich bedanke mich bei allen Mitgliedern für die sehr angenehme Arbeitsatmosphäre und Unterhaltungen während der Pausen.

An letzter Stelle möchte ich meinen endlosen Dank an meine Eltern Murat und Necla aussprechen, für die die Erziehung und Bildung ihrer Kinder stets an erster Stelle kamen. Ohne sie hätte ich diese Arbeit nicht einmal in Angriff nehmen können. Insbesondere bin ich meiner Mutter sehr verbunden für ihren aufopfernden und selbstlosen Einsatz, den sie zeitlebens für mich und meine Geschwister gezeigt hat.

Zusammenfassung

In dieser Arbeit untersuchen wir das Modell dipolarer Kugeln mit seitlich verschobenem Dipolmoment, d.h. das Dipolmoment ist innerhalb der Kugel dezentral lokalisiert, im Hinblick auf Strukturbildung und kollektive Dynamik im dreidimensionalen Raum, sowohl im Gleichgewicht als auch in einem rotierenden Magnetfeld. Die Untersuchungen erfolgen bei jenen thermodynamischen Zuständen, für die das betrachtete Modell kolloidale Flüssigkeiten darstellt. Die Verschiebung, d.h. der Abstand des Dipolmoments zum Teilchenzentrum, ist ein Kontrollparameter in der Untersuchung der Selbstassemblierung in Gleichgewichtssystemen bei endlichen Temperaturen und hat einen entscheidenden Einfluss auf die Bewegungsgleichungen. Diese werden hergeleitet, da sie für die Untersuchungsmethoden, nämlich Molekulardynamik- bzw. Langevindynamiksimulationen, die in dieser Arbeit zum Einsatz kommen, erforderlich sind. Um den grundsätzlichen Einfluss der Verschiebung auf die Selbstassemblierung zu verstehen, beginnen wir unsere Untersuchungen mit der Betrachtung von Grundzustandsstrukturen, die von wenigen harten Kugeln mit verschobenen Dipolen gebildet werden, wobei die Verschiebung jeweils variiert wird. Im ersten Hauptteil dieser Arbeit werden dann Untersuchungen zum Vielteilchensystem bei veränderlichen Temperaturen und Teilchendichten angestellt. Es ergeben sich spezifische Strukturen für unterschiedliche Verschiebungen. Diese Strukturen reichen von kettenartig über ringförmig bis hin zu dichtgepackt, wenn das Dipolmoment sukzessive aus dem Teilchenzentrum entfernt wird, wobei der genannte strukturelle Übergang ein fundamentales Verhalten dieses Modellsystems ist, welches wir für alle betrachteten thermodynamischen Zustandspunkte beobachten. Durch das Anlegen eines äußeren rotierenden Magnetfeldes wird das System aus dem Gleichgewicht getrieben. Es ist bekannt, dass sich im Falle von zentrierten Dipolen einfache Teilchenschichten parallel zur Rotationsebene des angelegten Feldes bilden. Dieses Phänomen ist Folge eines zeitgemittelten Dipolpotentials zwischen zwei Teilchen, welches wirkt, falls die Teilchen durch das äußere Feld synchronisiert werden. Die Synchronisation erfordert sowohl ein ausreichend starkes Feld als auch passende Rotationsfrequenzen, für die die Teilchenrotationen trotz der Reibung mit dem Lösungsmittel den Feldrotationen folgen können. Ausgehend von dem zentrierten System, welches als Referenzsystem dient, untersuchen wir das System für zwei spezifische Verschiebungen und finden einen strukturellen Übergang der ausgebildeten Teilchenschichten, der mit der Wahl der Feldfrequenz zusammenhängt. Und zwar beobachten wir die zunehmende Ausbildung von Doppelschichten für zunehmende Frequenzen, falls auch die Verschiebung ausreichend groß ist. Die Doppelschichtstruktur ist in Übereinstimmung mit den Ergebnissen des zeitgemittelten Dipolpotentials, das wir für die verschobenen Dipole herleiten. Die Schichtbildung für verschobene Dipole wird in Zustandsdiagrammen dargestellt, welche außerdem mit dem des Referenzsystems verglichen wird. Weiterhin zeigen wir, dass der Übergang von einfachen zu Doppelschichten einhergeht mit qualitativer Änderung des kollektiven Translations- als auch Rotationsverhaltens der Teilchen.

Abstract

In this thesis, we investigate the recent model of laterally shifted dipoles, i.e. spherical particles carrying a magnetic dipole moment in a non-central position, with a view to self-assembly as well as to the collective dynamics and the related pattern formation in three-dimensional bulk systems in equilibrium and in the presence of a rotating magnetic field. The shift, i.e. the distance of the dipole moment from the particle centre, is a control parameter in the investigation of the equilibrium systems and its crucial effect on the equations of motion, which are required for the Molecular or Langevin dynamics simulations that we use as method of investigation, is demonstrated. Preparatory examinations of ground states of few particle systems for several values of the shift precede the examination of the bulk systems studied at finite temperature and serve to understand the principles of self-assembly of this model. In the first main part of this work, we present the self-assembly structures formed by the particles depending on the amount of the shift, for several temperatures and particle densities corresponding to the liquid state. We find that the structural transition from chainlike to close packed aggregates upon the increase of the shift is a fundamental behaviour observed for all state points considered. By applying a rotating magnetic field, the system is driven out of equilibrium and in the case of conventional dipolar systems, for appropriate field strengths and frequencies, the dipolar rotations of the particles synchronize with the external field which is why the particles experience an averaged dipolar potential being attractive in the rotating plane and repulsive in the direction perpendicular to it. As a consequence, the particles organize in layered patterns which span parallel to the rotating plane. We show that sufficiently shifting the dipole moment crucially affects the formation of layers by enabling double layer formation instead of conventional, i.e. single layers. Deriving the averaged dipolar potential for shifted dipoles, we find that aside the condition of synchronization, double layer formation is based on the condition of locking of the particles' orientations such that the vectors pointing from the centre to the location of the dipole moment point either parallel or antiparallel to the direction perpendicular to the rotating plane. The formation of double layers is also observed in experiments and here, we demonstrate that not only the field strength but also the field frequency is decisive for their formation. Calculating the appropriate state diagram, we show that layer formation passes from single layers to double layers if the frequency is increased. This is accompanied by transitions of the collective translational as well as orientational behaviour of the particles.

Publications

Parts of this work is based on the publications listed below. Texts are partially rewritten and some extensions are introduced. Contributions from Co-Authors presented in this work are indicated in the text.

Self-assembly of three-dimensional ensembles of magnetic particles with laterally shifted dipoles Arzu B. Yener and Sabine H. L. Klapp, *Soft Matter* **12**, 2066, (2016), DOI: 10.1039/C5SM02648B

Double layer formation of magnetic Janus colloids in rotating magnetic fields Arzu B. Yener and Sabine H. L. Klapp, *in preparation*

Contents

1. Introduction	1
2. Model and Equations of motion	9
2.1. Model of dipolar spheres with shifted dipoles	9
2.2. Particle interactions	10
2.2.1. Hard sphere potential	10
2.2.2. Soft sphere potential	11
2.2.3. Dipolar potential	11
2.2.4. Total pair potential	12
2.3. Equations of motion	12
2.3.1. Translational equations of motion	12
2.3.2. Rotational equations of motion	13
3. Simulation methods	17
3.1. Molecular Dynamics Simulation	17
3.1.1. Leapfrog algorithm	17
3.1.2. Leapfrog algorithm for the isokinetic equations of motion	19
3.2. Langevin Dynamics Simulation	21
3.3. Monte Carlo Simulation	22
3.4. Simulation details	24
3.4.1. Periodic Boundary Conditions	24
3.4.2. Long Range Interactions	24
3.4.3. Reduced Units	25
4. Ground states of few particles	27
4.0.4. Analytical expression for the pair energy	28
4.0.5. Ground state pair configurations	29
4.0.6. Configurations for $N > 2$	31
4.0.7. Conclusion	36
5. Equilibrium Self-assembly	37
5.1. Classification of the Occurring Structures	38

Contents

5.2. Structural Analysis	39
5.2.1. Radial distribution function	39
5.2.2. Cluster analysis	43
5.3. Conclusion	47
6. Nonequilibrium pattern formation	49
6.1. Time-averaged Dipolar Potential U^{ID} for Shifted Dipoles	50
6.2. Numerical Results for U^{ID}	51
6.3. Layering of the Shifted Dipoles	56
6.3.1. Synchronized Quantities in the Shifted System	58
6.3.2. Effective Single Particle Theory Applied to Shifted Dipoles	60
6.3.3. Conclusion	61
6.4. Behaviour of the Shift Vectors in the Layered States	61
6.4.1. Static Behaviour	62
6.4.2. Dynamic Behaviour	65
6.5. Double Layer Formation	69
6.5.1. Explanation via U^{ID}	75
6.5.2. Double Layer formation in Experiments	78
6.6. Low frequency regime	79
6.7. Comparison to radial shifts	84
6.8. Summary	86
7. Conclusion and Outlook	87
Appendices	93
A. Centred Dipoles: Layer formation in the reference system	95
Bibliography	96

1

Introduction

Colloidal suspensions belong to the class of colloidal systems that appear in a large variety in everyday life such as foams, aerosols or gels, to name a few. First systematic examinations of colloidal suspensions hark back to the work of Thomas Graham (1861) who distinguished between solutions which completely diffuse through a membrane and those which he called "colloids": These suspensions comprised particles ("colloids") that could not penetrate through the membrane due to their large dimensions. Thus, a colloidal suspension consists of a solvent, like e.g. water or oil, in which solid particles are dispersed. One of the the main features making a colloidal suspension is Brownian motion of the particles in the solvent, which is provided for particle sizes of the order $10^{-9} - 10^{-6}m$. It should be emphasized that the allegedly simple system consisting of pollen grains suspended in water opened the door to the theoretical description of one of the most fundamental phenomena in nature, namely diffusion. Based on the observations of the botanist Robert Brown, who examined the system in 1827, Einstein derived in 1905 [1] the famous relation stating that the mean squared displacement of a Brownian particle grows linearly with time, on sufficiently large time scales.

Colloidal suspensions encompass a variety of representatives such as milk and blood as naturally appearing systems, or paints and lubricants which are synthetic systems.

A particular class of colloidal suspensions is constituted by ferrofluids. Developed in the mid of the 1960s [2], ferrofluids consist of permanent ferromagnetic particles, usually iron oxides such as magnetite (Fe_3O_4) or hematite (Fe_2O_3), dispersed in a polar or apolar liquid (water or oil, e.g.). Thereby, the crucial quantity in order to obtain ferromagnetic

colloids is the size of the particles, specifically a diameter of about 10nm ensures that the particles are magnetic single domains, i.e. the magnetization does not change across the particles. It is necessary to stabilize the colloids against agglomeration due to van der Waals and magnetic (and also gravitation) interactions because usually, thermal energy of the colloids being of the order of $k_B T$ is not sufficiently high to prevent their sticking. Thus, preparing the particles' surface with surfactant molecules or with an ionic shell ensures stability of the ferrofluid.

To the most important features of ferrofluids belong (i) that the system is superparamagnetic, i.e. the particles are aligned in an homogeneous external field yielding a polar system, while the total magnetization vanishes if the field is switched off (although the colloids are ferromagnetic), which thus makes the system highly controllable, (ii) that the viscosity of the ferrofluid alters under the application of an external field, allowing viscosity control, and (iii) its high qualities in terms of heat conduction. These made ferrofluids convenient for a large variety of applications. Their standardized use as e.g. ferrofluidic seals in rotary shafts [3], or as heat dissipators in loud speakers [4] is long-established, and beyond technical applications, ferrofluids are also found in e.g. medical applications as targeted drug delivery systems in cancer treatment [5, 6] or as contrast agents [7] in medical imaging. For an overview of further applications we refer to recent reviews The structural and thermodynamic properties of conventional ferrofluids are usually described by the models of dipolar hard (DHS) or soft (DSS) spheres which have been the object of intensive investigations since the 1970s. In these models, spherical particles carry a point dipole at their centres of mass and the anisotropy of the dipolar potential results in a very rich and complicated phase behaviour of dipolar spheres. Therefore, in the past decades, extensive debates concentrated e.g. on the question whether there is a gas-liquid coexistence in the DHS system, which was negated finally by the work of Sciortino *et al.* [8]. On the other hand, it is known that the Stockmayer fluid - a theoretic model consisting of the dipolar potential and the Lennard-Jones-potential - is the model which describes the vapour-liquid phase transition observed in ferrofluids correctly [9, 10], unlike the DSS or HSS [11, 9], and is thus the more convenient model for ferrofluid.

In the isotropic phase, the main feature of the dipolar systems is the self-assembly of the particles into chainlike structures. The occurring individual chains have a local order in that the particles arrange in head-to-tail orientation along the chain (see inset of Fig. 1.1, left), being enabled due to the anisotropy of the dipolar potential which favours this head-to-tail orientation. Yet, globally, the chains are disordered. The mean chain length decreases with increasing temperature, while passing to lower densities (and temperatures), the self-assembled structures become rings. In contrast, if the density is increased, a transition to the polar ferroelectric state is observed and at very high densities, the systems exhibit solid states with several lattice structures such as face or body centred. As a result of extensive theoretical and computer simulation studies of the last decades [12, 13, 14, 15, 16, 17, 18, 19], as well as of experimental examinations [20], the

phase behaviour of dipolar systems is rather good understood.

Figure 1.1, left, shows the first experimental verification of chain formation in real ferrofluids, obtained by cryogenic transmission electron microscopy [21]. The self-assembly is highly affected by the application of external magnetic fields whose particular character highly determines self-organisation of the particles. For example, a constant homogeneous field aligns the chains along the field direction [22], while structure formation driven by alternating fields such as triaxial ones for which the field vector describes a cone around a specified direction (z -axis of a reference frame), is wide ranged including networks of particle chains [23], self-healing membranes of colloidal magnetic particles [24, 25] and sheetlike [23] (see an example in Fig. 1.1, right) or honeycomb [24] structures. Definitely, the structure formation of dipolar systems goes far beyond than the few examples shortly mentioned here, and an overview of this topic can be found in the reviews [26, 27, 19, 23].

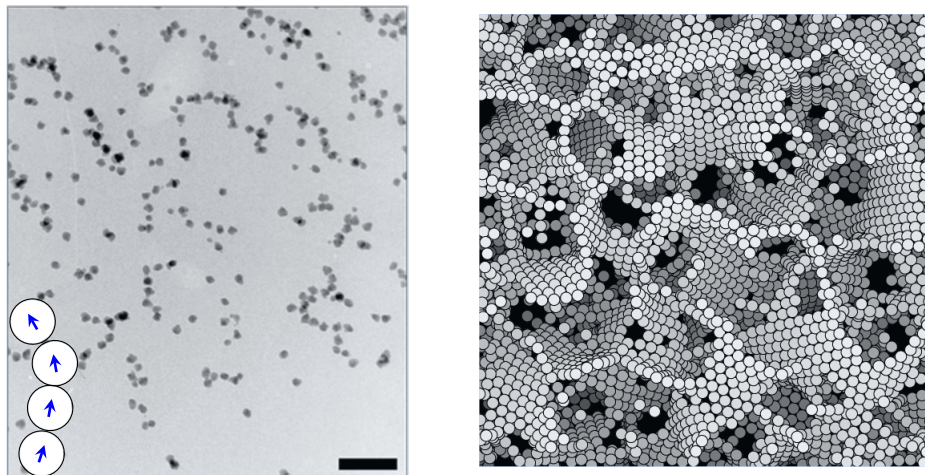


Figure 1.1.: *Left:* Cryogenic transmission electron microscopy image of iron dispersion, scale bar = 100nm. The image was taken from Ref. [21]. *Right:* Simulation results showing an open-cell foam built by walls of hexagonal sheets. The image was taken from Ref. [23]

The permanent need for novel materials meeting more and more specialized requirements entailed the development of functionalized particles with specific features, and as a result of progress in chemical engineering in the past decades, particle synthesis provided a new generation of complex colloidal particles with specific design. Complexity is generated by anisotropic shapes, i.e. beyond spherical shapes, as well as by anisotropic interactions having their origin in chemical or physical sources. To date, the combination of shape and interaction anisotropy yielded a plethora of novel, designed particles. Thus, additional to

spherical ones, one finds cubic, ellipsoidal, rod-like or dumbbell-like shaped colloidal particles. Besides, their surfaces may exhibit particular features such as so-called patches which are docking sites allowing interparticle bonding, or they can be Janus-like. In this case, one side of the particles has different character than the other one. An overview of the existing synthetic particles can be found in the reviews [28, 29, 30]. Clearly, the large variety of complexity has far reaching consequences on the self-assembly of complex colloids and it belongs to the topic of current research to find the key for directing self-assembly based on the controlled design of the particles' attributes [31, 32, 33, 34, 35, 36].

Specifically, novel types of *magnetic* colloids comprise, aside anisotropic [37, 38] shapes, spherical particles with a magnetic cap [39], micrometer-sized silicon balls carrying a magnetic cube beneath their surface [31] and magnetic Janus particles [40, 41] which are silica spheres with nickel coating of one of their hemispheres. The listed spherical magnetic colloids have in common that they consist of a carrier material such as silica and a magnetic material (iron oxide) which is situated in an asymmetric manner w.r.t. centre of the carrier particle. In Fig.1.2, sketches of these asymmetric magnetic colloids can be seen. The particles are micron sized, while the dimensions of their magnetic components are in the nanometre range and thus still can be treated as single domains. Thus, suspensions of these particles differ from conventional ferrofluids by particle symmetry and size.

All of these colloids show particularly interesting features if an external field is applied, such as controllable binding and unbinding of the particles [31] or chiral organization along chain-like structures [39]. Specifically in the case of janus particles, tubular structures [40] of tunable cross section geometry can be generated by a precessing magnetic field whose opening angle determines the particular type of the occurring tubes. This phenomenon is based on the complex magnetic response of the thin nickel coating. Its magnetic response has components parallel and perpendicular to the janus interface leading to synchronous rotation as well as oscillation of the particles, induced by the rotation and precession of the field. The rich variety of the occurring self-assembled and self-organized structures known from conventional ferrofluids is even enlarged in dipolar systems with these types of magnetic colloids. Essential is thereby the off-centred location of the magnetic component which is not covered by conventional model dipolar systems which consider centred locations of the dipole moments. Thus, the synthesis of these novel types of magnetic colloids did not only open a new era in experiments but also in the theoretical modelling of magnetic colloids. A first and successful model incorporating the shifted location of the magnetic component was proposed by Holm *et al.* [43] who shifted the dipole moment radially, i.e. parallel to the particle radius, out of the centre towards the particle surface. Ground state calculations [44] as well as the study of bulk systems [45] of such particles yielded that the shift of the dipole has an immense consequence on the self-assembly in these systems. Besides, the proposed model reproduces the behaviour of real particles with a magnetic cap studied by Baraban *et al.* [46]. However, the model is not convenient

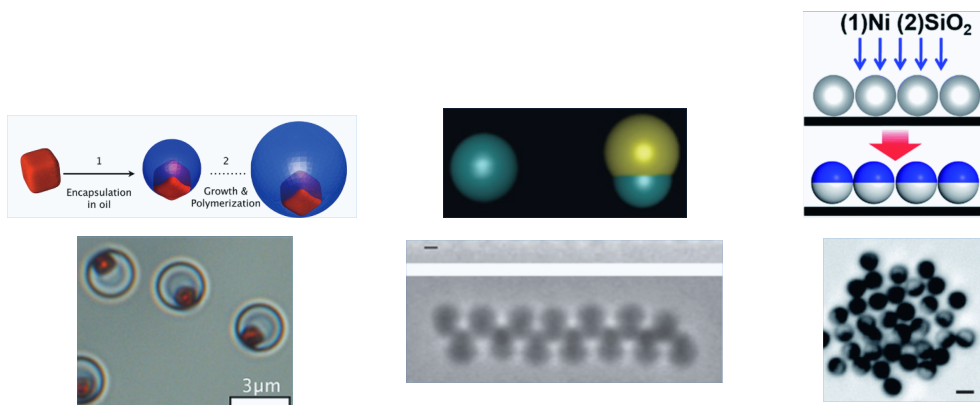


Figure 1.2.: *Left:*[31] The upper presentation schematically shows the encapsulation of a hematite microcube (red) into silicon balls which carry the magnetic cubes beneath their surfaces and thus forming particles with "magnetic patches". Below, a picture of the real particles, gained by optical microscopy, is shown. *Middle:* (top) Sketch of an isotropic paramagnetic particle (green) and of a capped particle consisting of a non magnetic material (yellow) carrying the magnetic material on its surface [39]. (bottom) Optical microscope image of real capped particles in the presence of an external magnetic field [39], scale bar = $1\mu m$. *Right:* Janus particles [42]. The upper scheme sketches the coating of non magnetic micron-sized silica spheres with nickel using electron beam deposition, yielding spherical particles with a magnetic and a non magnetic hemisphere. Below, the microscopic image of the Janus particles [42]. Scale bar = $2\mu m$.

for the description of magnetic patchy particles as well as magnetic Janus particles. For the former, Abricosov *et al.* [47] suggested to study the model of shifted dipoles with two variations of the orientation of the dipole moment vector, while keeping a fixed distance to the centre, and succeeded to describe the self-assembly correctly.

A shifted model in which the dipole moment vector is oriented perpendicular to the radius of the sphere is usually used to reproduce the behaviour of magnetic Janus particles [40]. The motivation to model such new types of particles is obvious: Only the detailed knowledge of the mechanisms governing particle interactions on the microscopic length scale allows to control the particles in a precise way. Besides, this knowledge also directs the way in the design of functionalized particles which are to fulfil specific requirements claimed by the needs in e.g. material science, technical applications or medicine. Yet, it is not only the application of these systems which makes them catching much and even increasing interest; Serving as model systems, they are also interesting and promising from a fundamental point of view, e.g. to study problems related to phase transitions [48, 49], entropy [50, 51, 52, 53], chirality [54, 55, 56] or synchronization [57, 58, 59, 60, 61], all belonging to fundamental phenomena in nature.

A powerful tool for the investigation of dipolar systems are Monte Carlo simulation, for the static properties, and classic Molecular Dynamics (MD), Langevin Dynamics (LD) or Brownian Dynamics (BD) simulations, which especially serve for the study of dynamic properties and unravel the time evolution of the systems under consideration. The latter three methods are based on solving the equations of motion for single particles, and specifically in LD and BD simulations, one considers stochastic differential equations originating from non-overdamped (LD) or overdamped (BD) Langevin equations. Difficult are the computations of dipolar systems because of time-consuming calculations due to long range interactions coming from the dipolar interactions. Yet, several methods were developed in the past decades to handle these, being the reaction field or the fast multipole methods [62]. The most popular method however is the Ewald summation technique which is not only numerically efficient but also yields the correct calculation of the dipolar interactions.

Aside computational methods, we mention the (dynamic) density functional theory [63, 64, 65, 66] as a theoretical mean for the examination of dipolar systems. This theory is based on finding the density distribution of systems in thermal equilibrium and also enables the calculation of the Helmholtz free energy of the system under consideration.

In the following, we concretise the motivation and goals of this thesis and outline its structure. Motivated by the expectation that not only the distance but also the orientation of the dipole moment within the particle has a crucial role on the self-assembly, we aim to understand the self-assembly in a system of spherical particles with laterally shifted dipoles as a function of the distance of the dipole from the centre. A similar study of this model was recently published [67], however, the authors only consider a quasi-twodimensional

system. We investigate the system in three-dimensions of translation and rotation and to our knowledge, this study is the first of this type. The shift of the dipole moment directly affects the equations of motion which we derive in chapter 2, after having introduced the model in detail. This is followed by chapter 3 in which we present the simulation methods used in this thesis.

The model under consideration is a relatively new proposal and thus, its exploration only recently started. We start our study by the calculation of ground state structures of systems of few particles (see chapter 4) in order to understand the principles of self-assembly upon the increase of the lateral shift of the dipole. Also in Ref. [67], ground states were proposed for this model, however, our results for the three-particle system slightly differs from those suggested by the authors.

Driving a bulk system of conventional DSS particles out of equilibrium by applying a rotating magnetic field, the collective dynamic behaviour of the particles, specifically the synchronized rotation of the dipole vector with the external field, leads to the phenomenon of layer formation of the particles for specific field parameters. This phenomenon was observed in former computer simulations [68, 69, 70, 71] as well as in experiments [72, 73] and was explained [74] by a time-averaged dipolar potential U^{ID} which acts if the particles synchronously rotate with external field. It was shown that this synchronization is a crucial prerequisite for layer formation [71]. Thus, a further motivation of this work is to answer the question to which extend the dynamic collective behaviour of shifted dipoles, specifically the synchronization, is affected if the system is driven out of equilibrium by rotating fields. Also, the new geometry of the particles indicate the formation of new patterns as well as new or additional non-equilibrium phenomena beyond synchronization, under the effect of the external driving field. The non-equilibrium system of laterally shifted dipoles will be considered in chapter 6. Yet, before, we first study the equilibrium behaviour of the system in chapter 5 which is indispensable for a thorough understanding of the non-equilibrium. We conclude the thesis with a conclusion and outlook in chapter 7.

2

Model and Equations of motion

2.1. Model of dipolar spheres with shifted dipoles

Our model consists of N spherical particles which can translate and rotate in all three dimensions. Each of the particles carries a permanent dipole moment $\boldsymbol{\mu}_i$, ($i = 1, \dots, N$) whose position within the particle is shifted with respect to the particle centre. Thereby, the fixed location of $\boldsymbol{\mu}_i$ within the particle is determined by the shift vector \mathbf{d}_i , as sketched in Fig. 2.1. In three dimensions, the specifications of the orientations of $\boldsymbol{\mu}_i$ and \mathbf{d}_i requires a body-fixed reference frame (in the following denoted by the subscript b) because, according to our choice, $\boldsymbol{\mu}_i$ and \mathbf{d}_i are not collinear and thus the particles are not uniaxial anymore. Specifically, we choose $\mathbf{d}_i^b = d(1, 0, 0)$ and $\boldsymbol{\mu}_i^b = \mu(0, 0, 1)$, with d and μ being constant for all particles. Hence, \mathbf{d}_i and $\boldsymbol{\mu}_i$ are oriented perpendicular to one another and we call this arrangement a lateral shift. With this choice, our particles differ from those considered in Ref. [44] where \mathbf{d}_i and $\boldsymbol{\mu}_i$ are arranged parallel and hence $\boldsymbol{\mu}_i$ is shifted radially.

Further on, in the laboratory reference frame, \mathbf{r}_i is the position vector of the particle centre while the position vector of $\boldsymbol{\mu}_i$ is given by $\mathbf{r}'_i = \mathbf{r}_i + \mathbf{d}_i$, where \mathbf{d}_i now denotes the shift vector in the laboratory frame. For $d = 0$, \mathbf{r}'_i coincides with \mathbf{r}_i yielding conventional dipolar systems with centred dipoles. A discussion of typical values of the relative shift $\delta = |\mathbf{d}|/2|\mathbf{R}|$ with $|\mathbf{R}|$ being the particle radius is given in section 5.

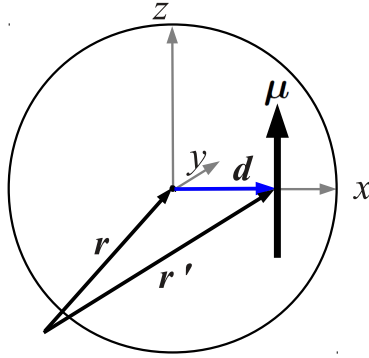


Figure 2.1.: Sketch of a dipolar sphere with a laterally shifted dipole moment. Also shown are the axes of the body-fixed coordinate system.

2.2. Particle interactions

To model the particle interactions in the colloidal suspension under consider, we use pairwise particle interactions where three-, four- and higher-particle interactions are neglected. While four- and higher particle contributions are small compared to two- and three-particle interactions, the latter has non-vanishing contributions to the energy. However, they require time consuming computations which is why they are not taken into account in computer simulations. This is justified as considering only pairwise interactions reproduce the properties of the liquid state sufficiently well [62]. Frequent idealised potentials used for colloidal systems are the hard sphere and soft sphere potentials, which also serve in this thesis to mimic the short-ranged repulsion of the particles in suspension. The magnetic interaction of the particles are modelled by the long-ranged dipolar potential. In the following, we present and shortly discuss the used potentials.

2.2.1. Hard sphere potential

The hard sphere potential is purely repulsive and is defined as

$$u_{HS}(r_{ij}) = \begin{cases} \infty, & r_{ij} \leq \sigma \\ 0, & r_{ij} > \sigma \end{cases} \quad (2.1)$$

with $r_{ij} = |\mathbf{r}_{ij}| = |\mathbf{r}_i - \mathbf{r}_j|$ being the centre-to-centre distance of particles i and j and σ is the particle diameter. Thus, $u_{HS}(r_{ij})$ is effective only when two particles come in contact where overlaps are not possible. Therefore, this potential is convenient when Monte Carlo simulations, described in section 3.3, are performed.

2.2.2. Soft sphere potential

In real molecular systems, the pair potential consists of an attractive part, due to van-der-Vaals interactions, and of a repulsive part. In the case of liquid argon e.g., the Lennard-Jones potential which includes an attractive and a repulsive term, reproduces very well this real behaviour of the atoms. For colloidal systems, the attractive part of the potential can be neglected if the particles are prevented to approach beyond distances for which van-der-Vaals attraction is relevant. This can be achieved by mechanism of steric repulsion, where the surfaces of the particles are prepared, e.g. via surfactants [2]. In this case, the soft sphere potential being defined as

$$u_S(r_{ij}) = \epsilon \left(\frac{\sigma}{r_{ij}} \right)^n \quad (2.2)$$

can be used to model the steric repulsion. Here, ϵ and n , are parameters for potential depth and steepness, respectively.

Shifted soft sphere potential

The soft sphere potential is short-ranged which allows to cut the potential at a certain cut-off distance r_c in computer simulations. The truncation has to be performed such that the potential and its first derivative, thus the force, is continuous. Otherwise, energy would not be conserved. The convenient truncation is accounted for by the shifted soft sphere potential

$$u_{SS}(r_{ij}) = \epsilon \left(\frac{\sigma}{r_{ij}} \right)^n - \epsilon \left(\frac{\sigma}{r_c} \right)^n + (r_c - r_{ij}) \left. \frac{du_{SS}(r_{ij})}{dr_{ij}} \right|_{r_{ij}=r_c}. \quad (2.3)$$

The second term on the right hand side shifts the potential achieving that it continuously vanishes at $r = r_c$ while the third term ensures that also the force vanishes continuously. The soft sphere potential usually is truncated at $r_c = 2.5\sigma$.

2.2.3. Dipolar potential

As our model comprises a non-central location of the point dipole within the particle, the centre-to-centre distance of two particles differs from their dipolar distance given by $r'_{ij} = |\mathbf{r}'_{ij}| = |\mathbf{r}_{ij} + \mathbf{d}_{ij}|$, with $\mathbf{d}_{ij} = \mathbf{d}_i - \mathbf{d}_j$ and the dipolar energy between two dipoles $\boldsymbol{\mu}_i$ and $\boldsymbol{\mu}_j$ is given by

$$u_{DD}(i, j) = \frac{\boldsymbol{\mu}_i \cdot \boldsymbol{\mu}_j}{r_{ij}^3} - \frac{3(\boldsymbol{\mu}_i \cdot \mathbf{r}'_{ij})(\boldsymbol{\mu}_j \cdot \mathbf{r}'_{ij})}{r_{ij}'^5}. \quad (2.4)$$

2.2.4. Total pair potential

The main goal of this thesis is to investigate a bulk system of a colloidal suspension of shifted dipoles (ferrofluid) at finite temperature. To model the total pair interaction $u(i, j)$ of the particles i and j , we combine the shifted soft sphere potential 2.3 for the steric interaction and the dipolar potential 2.4 for the magnetic ones which thus yields

$$u(i, j) = \epsilon \left(\frac{\sigma}{r_{ij}} \right)^n - \epsilon \left(\frac{\sigma}{r_c} \right)^n + (r_c - r_{ij}) \left. \frac{du_{SS}(r_{ij})}{dr_{ij}} \right|_{r_{ij}=r_c} + \frac{\boldsymbol{\mu}_i \cdot \boldsymbol{\mu}_j}{r_{ij}^3} - \frac{3(\boldsymbol{\mu}_i \cdot \mathbf{r}'_{ij})(\boldsymbol{\mu}_j \cdot \mathbf{r}'_{ij})}{r_{ij}^5}. \quad (2.5)$$

Moreover, we also perform ground-state calculations of few particles. In this case, we use the hard sphere potential 2.1 instead of Eq. 2.3 in Eq. 2.5.

2.3. Equations of motion

For conventional dipolar system in which the particles carry the dipole moment at the centre of mass, the equations of motion are straight forward, once the forces are known. In this case, the particles are uni axial and the rotational dynamics can be described by a single unit vector s_i which is collinear with the orientation of the vector of dipole moment. However, shifting the dipole moment out of the centre crucially affects the rotational dynamics of the particles. In the following, we write down the forces and torques on the particles and derive the equations of motion in the absence of a solvent.

2.3.1. Translational equations of motion

Following from the total pair interaction (see section 2.2.4) which consists of a short-ranged potential u_{short} (Eq. 2.1 or 2.3) and the dipolar potential (Eq. 2.4), particle i experiences the total force $\mathbf{F}_i = \mathbf{F}_i^{short} + \mathbf{F}_i^{DD}$ at its centre of mass. More precisely, the forces are obtained by

$$\mathbf{F}_i^{short} = - \sum_{j \neq i} \nabla_{\mathbf{r}_{ij}} u^{short}(r_{ij}) \quad (2.6)$$

and

$$\mathbf{F}_i^{DD} = - \sum_{j \neq i} \nabla_{\mathbf{r}'_{ij}} u^{DD}(\boldsymbol{\mu}_i, \boldsymbol{\mu}_j, \mathbf{r}'_{ij}), \quad (2.7)$$

where the sum is due to interactions with all other particles j , respectively. The first consequence of the shift manifests in the fact that the dipolar distance now differs from the centre-to-centre distance, as stated in section 2.2.3, and thus, the dipolar force \mathbf{F}_i^{DD} is obtained by the derivative with respect to \mathbf{r}'_{ij} . The second consequence is the fact that, unlike conventional dipolar systems, \mathbf{F}_i^{DD} does not act on the centre of mass any more but at the location of the dipole moment, \mathbf{r}'_i . However, the particle in our model is regarded to be rigid which thus yields that \mathbf{F}_i^{DD} also acts at \mathbf{r}_i and, altogether, \mathbf{F}_i effects a translation of the centre of mass. The Newtonian equations of motion for translation then are given by

$$m\ddot{\mathbf{r}}_i = \mathbf{F}_i \quad (2.8)$$

with $m = m_i \forall i$ being the mass of the particles.

2.3.2. Rotational equations of motion

While for translation, the second consequence of the shift does not change the particles' translation, it crucially determines the particles' rotational motion. More precisely, the dipolar force on the particle does not act at the particle centre anymore but at the location of the dipole moment, i.e. at \mathbf{r}' (see Fig. 2.1). Therefore, the shift \mathbf{d}_i generates the torque

$$\mathbf{T}_i^d = \mathbf{d}_i \times \mathbf{F}_i^{DD} \quad (2.9)$$

acting at \mathbf{r}_i , which supplements the torque

$$\mathbf{T}_i^\mu = \boldsymbol{\mu}_i \times \mathbf{G}_i^{DD} \quad (2.10)$$

stemming from angle dependent dipolar forces [75]. Here,

$$\mathbf{G}_i^{DD} = - \sum_{j \neq i} \nabla_{\boldsymbol{\mu}_i} u^{DD}(\boldsymbol{\mu}_i, \boldsymbol{\mu}_j, \mathbf{r}'_{ij}). \quad (2.11)$$

Thus, the total torque on the particle centre is given by

$$\mathbf{T}_i = \mathbf{T}_i^\mu + \mathbf{T}_i^d. \quad (2.12)$$

For $d = 0$, i.e. $\mathbf{r}'_i = \mathbf{r}_i$, the additional torque \mathbf{T}_i^d vanishes and the forces and torques reduce to the expressions familiar for centred dipoles (e.g. [62]). We also note that our treatment of the forces and torques in a system of shifted dipoles is equivalent to the virtual sites method introduced by Weeber *et al.* [44].

In the case of an external magnetic field

$$\mathbf{B} = B_0(\cos(\omega_0 t)\mathbf{e}_x + \sin(\omega_0 t)\mathbf{e}_y), \quad (2.13)$$

which we apply to drive the system out of equilibrium, the particles experience the torque

$$\mathbf{T}_i^{ext} = \boldsymbol{\mu}_i \times \mathbf{B}, \quad (2.14)$$

which is added to the total torque given in Eq. 2.12.

In order to describe the orientation of the body-fixed coordinate system w.r.t the laboratory frame, the rotation matrix [62]

$$\mathbf{R} = \begin{pmatrix} \cos \phi \cos \psi - \sin \phi \cos \theta \sin \psi & \sin \phi \cos \psi + \cos \phi \cos \theta \sin \psi & \sin \theta \sin \psi \\ -\cos \phi \sin \psi - \sin \phi \cos \theta \cos \psi & -\sin \phi \sin \psi + \cos \phi \cos \theta \cos \psi & \sin \theta \cos \psi \\ \sin \phi \sin \theta & -\cos \phi \sin \theta & \cos \theta \end{pmatrix} \quad (2.15)$$

can be defined such that any vector \mathbf{u}^b expressed in the body-fixed frame can be transformed to the laboratory frame via the relation

$$\mathbf{u} = \mathbf{R}^{-1} \cdot \mathbf{u}^b. \quad (2.16)$$

Here, ϕ , θ and ψ are Euler angles defined as following:

Starting from the configuration $\phi = \theta = \psi = 0$, i.e. the reference frames are congruent, ϕ is the angle which specifies the first rotation of the body-fixed frame about the laboratory frame's z -axis, θ gives the second rotation by tilting the laboratory frame's z -axis and ψ defines the final rotation about the laboratory frame's new z -axis.

The body-fixed coordinate system is chosen such that the inertia tensor $\mathbf{I}_i = \mathbf{I} \forall i$ is diagonal. Besides, for spherical particles, for the non-vanishing entries of \mathbf{I} , $I_{xx} = I_{yy} = I_{zz} = I$ holds.

Under these conditions and given the torque (Eq. 2.12), the equations of motion for the angular velocity $\boldsymbol{\omega}_i$ is obtained by [62]

$$\mathbf{T}_i^b = I\dot{\boldsymbol{\omega}}_i. \quad (2.17)$$

Moreover, if the orientation of the particle i is to be obtained, an equation of motion for the rotation matrix \mathbf{R}_i is needed. To this end, it is most convenient to describe orientation through the concept of quaternions in stead of through Eulerian angles. This is because appropriate equations of motion for ϕ , θ and ψ include terms of \sin^{-1} which cause numerical problems if these terms vanish.

A quaternion is given by four scalar numbers, $\mathbf{Q} = (q^0, q^1, q^2, q^3)$ which has to satisfy the condition

$$(q^0)^2 + (q^1)^2 + (q^2)^2 + (q^3)^2 = 1 \quad (2.18)$$

if they are to be used in order to represent rotation. Defining [62]

$$q^0 = \cos \frac{\theta}{2} \cos \frac{\phi + \psi}{2} \quad (2.19)$$

$$q^1 = \sin \frac{\theta}{2} \cos \frac{\phi - \psi}{2} \quad (2.20)$$

$$q^2 = \sin \frac{\theta}{2} \sin \frac{\phi - \psi}{2} \quad (2.21)$$

$$q^3 = \cos \frac{\theta}{2} \sin \frac{\phi + \psi}{2} \quad (2.22)$$

makes the connection to the Eulerian angles in the above defined convention and the rotation matrix of Eq. 2.23 takes the form

$$\mathbf{R} = \begin{pmatrix} (q^0)^2 + (q^1)^2 - (q^2)^2 - (q^3)^2 & 2(q^1q^2 + q^0q^3) & 2(q^1q^3 - q^0q^2) \\ 2(q^1q^2 - q^0q^3) & (q^0)^2 - (q^1)^2 + (q^2)^2 - (q^3)^2 & 2(q^2q^3 + q^0q^1) \\ 2(q^1q^3 + q^0q^2) & 2(q^2q^3 - q^0q^1) & (q^0)^2 - (q^1)^2 - (q^2)^2 + (q^3)^2 \end{pmatrix}. \quad (2.23)$$

Finally, the quaternion for each particle i can be obtained by the equation of motion

$$\dot{\mathbf{Q}}_i = \frac{1}{2} \mathbf{W} \boldsymbol{\Omega}_i^b. \quad (2.24)$$

Here, the quantity $\dot{\mathbf{Q}}_i$ is the time derivative of the quaternion and the matrix \mathbf{W} is defined as (see [62])

$$\mathbf{W} = \begin{pmatrix} q_i^0 & -q_i^1 & -q_i^2 & -q_i^3 \\ q_i^1 & q_i^0 & -q_i^3 & q_i^2 \\ q_i^2 & q_i^3 & q_i^0 & -q_i^1 \\ q_i^3 & -q_i^2 & q_i^1 & q_i^0 \end{pmatrix}, \quad (2.25)$$

2. Model and Equations of motion

while the quaternion $\mathbf{\Omega}_i^b = (0, \omega_{ix}^b, \omega_{iy}^b, \omega_{iz}^b)$ corresponds to the x , y and z components of the angular velocity.

Altogether, Eqs. 2.17 and 2.24 present the equations of motion for rotation and a procedure how they are used in Molecular dynamics simulation is presented in the next section.

3

Simulation methods

3.1. Molecular Dynamics Simulation

Molecular dynamics (MD) simulation is a method to generate particle trajectories by integrating the Newtonian equations of motion (see Eqs. 2.8, 2.17, 2.24) at successive time steps Δt , starting from a certain initial configuration. This procedure yields solutions where the total energy is conserved and constant while kinetic and potential energies are subject to fluctuations. That means, the obtained trajectories correspond to the microcanonical ensemble. Besides, the influence of the solvent is not taken into account. However, for the simulation of a liquid in a more realistic way, one has to include the effect of a solvent. In the most simple way, this can be done by constraining the temperature to a fixed value by e.g using the Gaussian isokinetic thermostat. In this case, the generated trajectories which are obtained from solving the isokinetic equations of motion instead of the Newtonian ones, differ from the Newtonian trajectories minimally. The isokinetic equations of motion sample the isokinetic ensemble which in equilibrium corresponds to the canonical ensemble [76]. Several algorithms exist to solve the equations of motion and we choose one of the most frequently used ones being the Leapfrog algorithm which is described below for both cases, the Newtonian as well as the isokinetic. In addition, we also describe the Gaussian isokinetic thermostat in more detail.

3.1.1. Leapfrog algorithm

This procedure yields the current positions $\mathbf{r}(t)$ of the the particles at full time steps t and the velocities $\dot{\mathbf{r}}(t)$ at half a time step later, $t + \Delta t/2$,

$$\dot{\mathbf{r}}_i(t + \Delta t/2) = \dot{\mathbf{r}}_i(t - \Delta t/2) + \Delta t \cdot \mathbf{F}_i(t)/m \quad (3.1)$$

$$\mathbf{r}_i(t + \Delta t) = \mathbf{r}_i(t) + \Delta t \cdot \dot{\mathbf{r}}_i(t + \Delta t/2). \quad (3.2)$$

One simulation step then starts with proceeding the velocities via Eq. 3.1, proceeding the positions via Eq. 3.2 and finally calculating the forces from the Newtonian equations of motion (see Eq. 2.8) for the next time step. The velocities at full time steps can be calculated by

$$\dot{\mathbf{r}}_i(t) = \frac{\dot{\mathbf{r}}_i(t - \Delta t/2) + \dot{\mathbf{r}}_i(t + \Delta t/2)}{2}. \quad (3.3)$$

This is the general scheme of the Leapfrog algorithm and the treatment of particle orientations for linear molecules is equivalent.

In the case of quaternions, the equations to be solved read

$$\mathbf{l}_i(t + \Delta t/2) = \mathbf{l}_i(t - \Delta t/2) + \Delta t \cdot \mathbf{T}_i(t) \quad (3.4)$$

$$\mathbf{Q}_i(t + \Delta t) = \mathbf{Q}_i(t) + \Delta t \cdot \dot{\mathbf{Q}}_i(t + \Delta t/2), \quad (3.5)$$

where \mathbf{l}_i is the angular momentum and $\dot{\mathbf{Q}}_i$ and \mathbf{T}_i are obtained from Eqs. 2.17 and 2.24, respectively. The direct application of the Leapfrog algorithm to these equations involve the difficulty that the calculation of the derivatives $\dot{\mathbf{Q}}_i$ require the knowledge of $\mathbf{Q}_i(t + \Delta t/2)$ which is not yet given at that time. In order to address this problem, a modified Leapfrog scheme can be used [62, 77]. Accordingly,

1. Calculate the momenta at time t

$$\mathbf{l}_i(t) = \mathbf{l}_i(t - \Delta t/2) + \Delta t/2 \cdot \mathbf{T}_i(t) \quad (3.6)$$

2. Transform these to the body-fixed system using Eq. 2.23 and calculate the angular velocities

$$\mathbf{l}_i^b(t) = \mathbf{R} \cdot \mathbf{l}_i(t) \quad (3.7)$$

$$\boldsymbol{\omega}_i^b(t) = \mathbf{l}_i^b(t)/I \quad (3.8)$$

3. Calculate $\dot{\mathbf{Q}}_i(t)$ from Eq. 2.24 and advance the quaternions to time $t + \Delta t/2$

$$\mathbf{Q}_i(t + \Delta t/2) = \mathbf{Q}_i(t) + \Delta t/2 \cdot \dot{\mathbf{Q}}_i(t) \quad (3.9)$$

This step is an auxiliary step which estimates the $\mathbf{Q}_i(t + \Delta t/2)$ needed for the determination of the rotation matrix at time $t + \Delta t/2$.

4. Perform the integration of Eq. 3.4 and convert these then to the body-fixed system
5. Finally, obtain $\dot{\mathbf{Q}}_i(t + \Delta t/2)$ and perform the integration in Eq. 3.5.

3.1.2. Leapfrog algorithm for the isokinetic equations of motion

In this work, we use the isokinetic equations of motion and thus, we describe in detail how the Gaussian thermostat is used for translation as well as for rotation.

Translation

The isokinetic equations of motion [62]

$$\dot{\mathbf{r}}_i = \mathbf{p}/m \quad (3.10)$$

$$\dot{\mathbf{p}}_i = \mathbf{F}_i - \xi(\mathbf{r}_1, \dots, \mathbf{r}_N, \mathbf{p}_1, \dots, \mathbf{p}_N) \mathbf{p}_i$$

procure that the temperature of the system is kept constant by the "friction coefficient ξ " with the relation

$$\xi = \frac{\sum_i \mathbf{F}_i \cdot \mathbf{p}_i}{\sum_i |\mathbf{p}_i|^2}. \quad (3.11)$$

The equations 3.10 can be solved using the Leapfrog algorithm in the following way [62]:

1. Make an unconstrained half step and determine the velocities at time t

$$\dot{\mathbf{r}}_i(t) = \dot{\mathbf{r}}_i(t - \Delta t/2) + 1/2 \Delta t \cdot \mathbf{F}_i(t)/m \quad (3.12)$$

2. Calculate herefrom the actual temperature in the system by $\mathcal{T}_{trans} = 1/(3Nk_B T) \sum_{i=1}^N m \dot{\mathbf{r}}_i^2$. Further, calculate $\chi_{trans} = \sqrt{T/\mathcal{T}_{trans}}$, where T is the desired temperature.
3. Complete the calculation for the velocity by

$$\dot{\mathbf{r}}_i(t + \Delta t/2) = (2\chi_{trans} - 1) \cdot \dot{\mathbf{r}}_i(t - \Delta t/2) + \chi_{trans} \cdot \Delta t \mathbf{F}_i(t)/m. \quad (3.13)$$

Obviously, the scaling factor χ_{trans} accelerates the particles if the actual temperature is less than the desired one and vice versa. This is the principle of the Gaussian thermostat. Having calculated the thermostatted velocities in Eq. 3.13, the positions can be calculated by Eq. 3.2.

Rotation

The treatment of the thermostatted rotational motion happens in a similar way as for translation, modifying the procedure in section 3.1.1 [77]. More precisely, after having performed step 1, the scaling factor $\chi_{rot} = \sqrt{T/\mathcal{T}_{rot}}$ is calculated with the unmodified rotational kinetic temperature of the system being $\mathcal{T}_{rot} = 1/(3Nk_B T) \sum_{i=1}^N I\omega_i^2$. In order to keep the temperature constant, Eq. 3.6 is multiplied with χ_{rot} . During the further performance of the procedure, Eq. 3.4 is replaced by

$$\mathbf{l}_i(t + \Delta t/2) = (2 - 1/\chi_{rot}) \mathbf{l}_i(t) + \Delta t/2 \mathbf{T}_i(t). \quad (3.14)$$

3.2. Langevin Dynamics Simulation

Aiming at a more realistic modelling of the colloidal suspension under consider, i.e. the ferrofluid, we use Langevin dynamics simulations. Langevin dynamics describes the motion of the colloid by two additional terms added to the Newtonian's equation of motion. The first additional terms is a friction term which decelerates the colloid during its motion in the solvent. The second one mimics the random kicks of the solvent particles with the colloid, making sure that the particle does not stop but fulfils Brownian motion. Thus, the equations of motion for Langevin dynamics [78, 62] are given by

$$m\ddot{\mathbf{r}}_i = \mathbf{F}_i - \xi_t \dot{\mathbf{r}}_i + \mathbf{F}_i^{Gauss} \quad (3.15)$$

for translation, and

$$I\dot{\boldsymbol{\omega}}_i^b = \mathbf{T}_i^b - \xi_r \boldsymbol{\omega}_i^b + \mathbf{T}_i^{bGauss} \quad (3.16)$$

for rotation. Here, ξ_t and ξ_r are the translational and rotational friction coefficients, respectively, and \mathbf{F}_i^{Gauss} and \mathbf{T}_i^{bGauss} are random Gaussian forces and torques, respectively, with zero mean

$$\langle \mathbf{F}_i^{Gauss}(t) \rangle = 0 \quad (3.17)$$

$$\langle \mathbf{T}_i^{bGauss}(t) \rangle = 0 \quad (3.18)$$

whose variance satisfy [79]

$$\langle \mathbf{F}_{i\alpha}^{Gauss}(t) \mathbf{F}_{j\beta}^{Gauss}(t') \rangle = 6k_B T \xi_t \delta_{ij} \delta_{\alpha\beta} \delta(t - t') \quad (3.19)$$

$$\langle \mathbf{T}_{i\alpha}^{bGauss}(t) \mathbf{T}_{j\beta}^{bGauss}(t') \rangle = 6k_B T \xi_r \delta_{ij} \delta_{\alpha\beta} \delta(t - t') \quad (3.20)$$

with α and β denoting the Cartesian components x , y and z .

Equations 3.15 and 3.16 can be solved using the Leapfrog algorithm described in section 3.1.1.

3.3. Monte Carlo Simulation

In this work, we consider a many particle system with fixed particle number N in a fixed volume V and at fixed temperature T . In statistical mechanics, such system corresponds to the canonical one of the statistical ensembles in the Gibbs ensemble theory, in which the average of a quantity A is given by

$$\langle A \rangle = \frac{\int_{\Gamma} d\Gamma' A(\Gamma') \exp -\beta H(\Gamma')}{\int_{\Gamma} d\Gamma' \exp -\beta H(\Gamma')}. \quad (3.21)$$

Here, $H(\Gamma)$ denotes the Hamiltonian of the total system and

$\Gamma = \Gamma(\mathbf{r}_1, \dots, \mathbf{r}_N, \mathbf{p}_1, \dots, \mathbf{p}_N, \boldsymbol{\omega}_1, \dots, \boldsymbol{\omega}_N, \mathbf{l}_1, \dots, \mathbf{l}_N)$ is a point in the phase space being spanned by the positions, linear momenta, orientations and angular momenta of the particles $i \dots N$, respectively. Thus, Γ specifies the microscopic state of the system. For a many particle system, usually it is not possible to numerically integrate the partition function, i.e. the denominator of Eq. (3.21), more precisely the configurational part of it, due to the high dimensionality of configuration space of such systems. Yet, this is required for the calculation of the averages of quantities of interest. In a Monte Carlo (MC) simulation, the configurational space is stochastically sampled through the generation of random configurations of the accessible states. However, even in a computer simulation based on a sampling with a uniform distribution, this calculation is not possible. Instead, the so-called importance sampling is applied by choosing a sampling with a distribution which is equivalent to the distribution function of the ensemble considered [80], which is in our case the canonical distribution ρ_{NVT} . For a realisation of the importance sampling, Metropolis *et al.* [80] suggested a procedure for which the calculation of the partition function is not required. In the following, we summarize the Metropolis scheme according to Ref. [62].

In order to sample the configurational phase space, i.e. in order to generate a trajectory in this space, a Markov chain is build, consisting of the states within this space. Thereby, the transition from state m to state n in its vicinity is governed by a transition matrix α fulfilling $\alpha_{mn} = \alpha_{nm}$ (condition for detailed balance) and being of the form

$$\alpha_{mn} = f(\rho_n/\rho_m) \text{ for } \rho_n < \rho_m, \quad (3.22)$$

while otherwise, α_{mn} has a positive value. For both cases, $m \neq n$ holds and ρ_m and ρ_n are the probabilities for the states m and n to occur, respectively. For these choices, the transition matrix fulfils $\sum_n \alpha_{mn} = 1$ and the probability for the system to stay in its initial state is given by the element $\alpha_{mm} = 1 - \sum_{n \neq m} \alpha_{mn}$. In particular, with this choice, the knowledge of the partition function is not needed.

Specifically, the system is carried from state m to n by trial moves within a defined range, and, for a transition for which this range is exceeded, $\alpha_{mn} = 0$ holds. For a trial move resulting in a negative change of the potential energy of the total system, $\delta U_{mn} \leq 0$, the new configuration belonging to state n will be more probable than the old one m . In this

case, the new configuration is accepted. On the other hand, for $\rho_n < \rho_m$, i.e. the change of potential energy is positive, this leads to an acceptance of the trial move with probability

$$\rho_n/\rho_m = \exp\left(-\frac{\delta U_{mn}}{k_B T}\right), \quad (3.23)$$

where δU_{mn} is the difference in the potential energy of the states m and n . If the trial move is not accepted, the system stays in its old state m .

This procedure runs through an iterative algorithm and the above presented choice of the transition matrix ensures that at the end of the algorithm, each state m , generated by trial moves, will have occurred with probability $\rho_m = \rho_{NVT}(m)$. Finally, the average quantity of interest is obtained by averaging the quantity over its values after each trial move, i.e. over all configurations generated.

3.4. Simulation details

The MD and LD simulations were carried out with a time step of $\Delta t^* = 0.0025$ and mostly with $N = 864$ particles and lasted for 3×10^6 steps. Larger scale simulations with $N = 1372$ and simulation times up to 8×10^6 steps confirmed the results were conducted for nicer snap shots shown in chapter 6.

We start all simulations with random initial configuration, avoiding overlaps, and random dipolar orientations. Quantities of interest were measured after an equilibration time of 2×10^6 time steps.

3.4.1. Periodic Boundary Conditions

In this work, we study 3D bulk systems and do not consider any surface effects. In simulations, this is typically realized by applying periodic boundary conditions. Specifically, the cubic simulation box of side length L is periodically replicated in space in such a way that if a particle leaves the box at one side, it enters the periodic image of the box which borders on the box at that side. This image is then shifted onto the original box such that the particle is located again in the simulation box.

3.4.2. Long Range Interactions

To account for the long range dipolar interaction u_{DD} , we apply the three-dimensional Ewald summation technique [75]. Accordingly, the dipolar potential consists of contributions calculated in real space (Eq. (3.24)), in Fourier (Eq. (3.25)) space and of a correction due to the interaction of a particle with itself (Eq. (3.26)). Details can be found in several text books such as [62, 76, 75]. Thus, the dipolar potential is given by [81, 62]

$$u_{DD}^{Ewald} = \frac{1}{2} \sum_{i \neq j} ((\boldsymbol{\mu}_i \cdot \boldsymbol{\mu}_j) B(r'_{ij}, \alpha) - (\boldsymbol{\mu}_i \cdot \mathbf{r}'_{ij})(\boldsymbol{\mu}_j \cdot \mathbf{r}'_{ij}) C(r'_{ij}, \alpha)) \quad (3.24)$$

$$+ \frac{1}{2L^3} \sum_{\mathbf{k} \neq 0}^{k_{max}} \frac{4\pi}{k^2} \exp\left(-\frac{k^2}{4\alpha^2}\right) (\boldsymbol{\mu}_i \cdot \mathbf{k})(\boldsymbol{\mu}_j \cdot \mathbf{k}) \cos(\mathbf{k} \cdot \mathbf{r}'_{ij}) \quad (3.25)$$

$$- \frac{2\alpha^3}{3\sqrt{\pi}} N \mu^2, \quad (3.26)$$

where the functions B and C are defined as

$$B(r, \alpha) = \left(\frac{2\alpha r}{\sqrt{\pi}} \exp(-\alpha^2 r^2) + \text{erf}(\alpha r)\right) / r^3 \quad (3.27)$$

$$C(r, \alpha) = \left(\frac{2\alpha r}{\sqrt{\pi}} (3 + 2\alpha^2 r^2) \exp(-\alpha^2 r^2) + 3\text{erf}(\alpha r)\right) / r^5 \quad (3.28)$$

This expression applies for conducting boundaries and if the convergence parameter α of the real space part is chosen large enough which allows to consider only interactions within the simulation box. The parameter α chosen to be $\alpha = 6.0/L$. For the Fourier part of the

Ewald sum we consider wave vectors \mathbf{k} up to $(\mathbf{k})^2 = 54$, giving a total number of wave vectors $n_k = 1500$.

3.4.3. Reduced Units

For convenience, in the MD simulations, we use reduced units, denoted by a “*” and summarized in table 3.1. Thereby, all units are referred to the unit of length being the particle diameter σ and to the unit of energy being the depth of the repulsive potential (see Eq. (2.2)), ϵ . The mass is set to unity.

Table 3.1.: Reduced units.

Quantity	Reduced unit
distance r	$r^* = \frac{r}{\sigma}$
density ρ	$\rho^* = \sigma^3 \rho$
temperature T	$T^* = \frac{k_B T}{\epsilon}$
dipole strength μ	$\mu^* = \frac{\mu}{\sqrt{m\sigma^2\epsilon}}$
moment of inertia I	$I^* = \frac{I}{m\sigma^2}$
time t	$t^* = t\sqrt{\frac{m\sigma^2}{\epsilon}}$
field strength B_0	$B_0^* = B_0\sqrt{\frac{\sigma^3}{\epsilon}}$
field frequency ω_0	$\omega_0^* = \omega_0\sqrt{\frac{m\sigma^3}{\epsilon}}$
friction coefficient for translation ξ_t	$\xi_t = \xi_t\sqrt{\frac{\sigma^2}{m\epsilon}}$
friction coefficient for rotation ξ_r	$\xi_r = \xi_r\sqrt{\frac{1}{m\epsilon\sigma^2}}$
torque \mathbf{T}	$\mathbf{T}^* = \frac{\mathbf{T}}{\epsilon}$

4

Ground states of few particles

The dipolar potential (Eq. (2.4)) can be minimized via the minimization of the dipolar distance and at the same time via optimal relative dipolar orientations, which is head-to-tail for two spheres with central dipoles. For these, the minimal dipolar distance, i.e. the centre-to-centre distance, cannot be underrun. In contrast, two spheres with shifted dipoles incorporate the feasibility of minimizing their dipolar distance beyond their centre-to-centre distance by attaining convenient configurations. This is true because shifting the dipole causes asymmetry of the particles such that the dipole moment has a smaller distance to one hemisphere than to the other. This yields an important consequence, namely, the new geometry of the particles entails new configurations (and also new relative dipolar orientations) pertaining to the appropriate minimal dipolar energy. This is why the self assembly of such particles will be highly affected by the shift of the dipoles and in order to understand self assembly, we first have to understand which mechanisms drive the minimization of the dipolar potential of shifted dipoles, thus to find the ground state configurations for the according values of δ .

To investigate ground state configurations of small clusters of particles interacting via the pair potential $u(i, j) = u_{HS} + u_{DD}$ (see Eqs. (2.4), (2.5) and (2.1)), we employ a simulated annealing procedure [44] which involves a Monte Carlo simulation using the Metropolis algorithm, which is described in section 3.3. Within this method, we choose initial states with comparable dipolar and thermal energies, i.e. $u_{DD}/k_B T \approx 1$. Here, u_{DD} is the dipolar energy of two hard spheres in contact with central dipoles having head to tail orientation. We then lower the temperature stepwise to zero. At each temperature, 10^6 trial moves are performed while conducting the usual Metropolis scheme involving

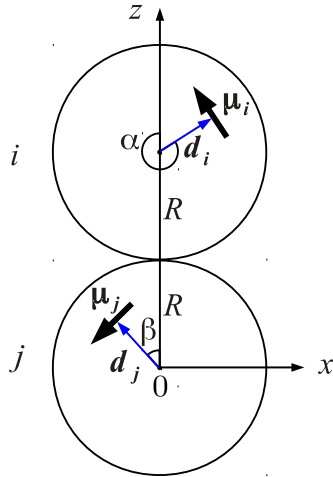


Figure 4.1.: Sketch of two dipolar hard spheres i and j and the orientations of their shift and dipole vectors in the x - z -plane.

translational and rotational trial moves. We realize an acceptance ratio of 60% by regularly adjusting the absolute value of the translational displacement during the simulation. New orientational configurations are generated by rotating the particles with a constant angle of $d\phi = \pi/18$ around one of the three axes of the laboratory fixed frame. In order to ensure that we reach the state with lowest energy, we start several simulations for each set of parameters and choose those results with the lowest energy as the minimum energy state.

4.0.4. Analytical expression for the pair energy

As a first step towards understanding the impact of the lateral shift, we study the dipolar energy of two hard spheres with shifted dipoles (see Eq. (2.5) with $u_{short} = u_{HS}$). Specifically, we derive an analytical expression for the pair energies as function of the relative shift δ . A similar derivation (leading to the same result) was very recently presented in [67].

The basis of the derivation is the coordinate system shown in Fig. 4.1. Note that this is a two-dimensional system (x - z -plane) where the orientations of the dipoles along the y -axis, i.e. out-of-plane orientations, are neglected. This assumption is confirmed by simulation studies of q2D dipolar systems showing that out-of-plane fluctuations vanish for decreasing temperatures [82]. In Fig. 4.1, the angles α and β describe the orientations of the shift vectors \mathbf{d}_i and \mathbf{d}_j with respect to the z -axis. As a result of the fixed orthogonal orientation of the the shift vector to the dipole vector, the orientations of $\boldsymbol{\mu}_i$ and $\boldsymbol{\mu}_j$ with respect to the z -axis are found by $\alpha + \pi/2$ and $\beta + \pi/2$. With these definitions of the angles, the results for our lateral shift can be directly compared to those for the radial shift given in Ref. [44]. Being in accordance with the above discussions, the sketch in Fig. 4.1 clearly demonstrates that the distance $|\mathbf{r}'_{ij}|$ varies with α , β and δ , which yields, after some

algebraic transformations,

$$\begin{aligned}
u_{DD}(\delta, \alpha, \beta) = & \frac{\mu^2}{\sigma^3} \left[\frac{\cos(\alpha - \beta) - 3 \sin \alpha \sin \beta}{[2\delta^2(1 - \cos(\alpha - \beta)) + 1 + 2\delta(\cos \alpha - \cos \beta)]^{3/2}} \right. \\
& - \frac{3\delta^2 \cos(\alpha + \beta)(\sin \beta - \sin \alpha)^2}{[2\delta^2(1 - \cos(\alpha - \beta)) + 1 + 2\delta(\cos \alpha - \cos \beta)]^{5/2}} \\
& \left. - \frac{3\delta(\sin \beta - \sin \alpha)(1 + \delta(\cos \alpha - \cos \beta)) \sin(\alpha + \beta)}{[2\delta^2(1 - \cos(\alpha - \beta)) + 1 + 2\delta(\cos \alpha - \cos \beta)]^{5/2}} \right] \quad (4.1)
\end{aligned}$$

for the dipolar potential u_{DD} in terms of the parameters α , β and δ . This expression is equivalent to that of Ref. [67] (as can be seen after some rewriting.) We now aim at finding the minimum energy states, E_G , of two dipolar hard spheres as a function of δ . To this end, we minimize Eq. (4.1) with respect to α and β and compare the results with simulated annealing calculations in three dimensions, as described above. As the plot in Fig. 4.2 clearly shows, the analytically gained results perfectly fit the numerical ones. Furthermore, it can be seen that the ground state energy $E_G(\delta)$ (which agrees with that calculated in [67]) is a quantity which decreases with increasing shift. Initially, $E_G(\delta)$ changes slowly and is comparable to that of non shifted dipoles suggesting that in this region, shifting the dipole moments out of the centres does not have a significant effect on the system. Upon further increase in δ , $E_G(\delta)$ starts to rapidly decrease. This is a result of the fact that shifting the dipoles out of the centres enables them to reduce their distance compared to the case with zero shift. This effect becomes more and more pronounced with growing δ as the dipolar potential of Eq. (2.4) follows a power law of the dipolar distance.

In the derivation of Eq. (4.1), configurations with one of the dipoles, e.g. i , having a mirror-inverted orientation w.r.t. the z -axis, are not included, however, this orientation would be described by $\alpha - \pi/2$, resulting in a change of some signs in Eq. (4.1) and does not yield configurations with energies lower than those found and discussed in Fig. 4.2. This is as also confirmed by the simulation results which were conducted in three-dimensional space. When the results shown in Fig. 4.2 are compared to the corresponding results of radially shifted dipoles of Ref. [43], a qualitative agreement of the function $E_G(\delta)$ can be seen. Yet, in the case of lateral shifts, the reduction of energy sets in earlier, i.e. for smaller shifts δ than those of radial shifts for which the energy starts to decrease only at $\delta \approx 0.25$. Further light on this issue is shed by inspecting the ground state configurations presented in the next section.

4.0.5. Ground state pair configurations

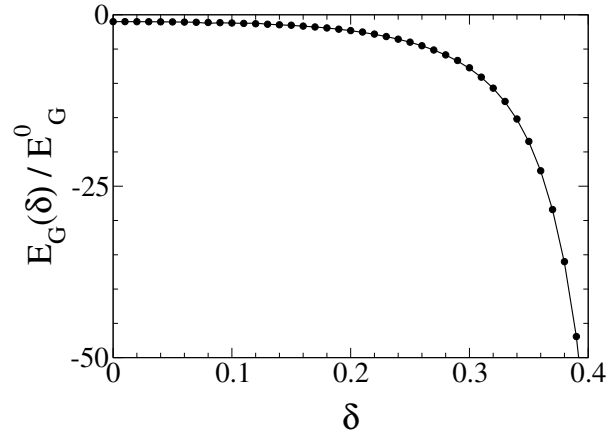


Figure 4.2.: Ground state pair energy E_G normalized by the corresponding ground state energy $E_G^0 = -2\mu^2/\sigma^3$ of centred dipoles. The results are obtained by simulated annealing (circles) and by minimization of Eq. (4.1) (solid line).

The ground state configurations pertaining to a given shift δ are determined by those values for the angles α and β that minimize Eq. (4.1). In Fig. 4.3, the angles α and β , as well as the cosine of the enclosed angle $\Delta(\delta) = \angle(\boldsymbol{\mu}_1, \boldsymbol{\mu}_2)$ between the dipoles in their ground state arrangements at different shifts are shown. For $\delta = 0$, $\cos(\Delta = 0) = 1$ holds. We also note that for $\delta = 0$, the two sets $\alpha = \beta = \pi/2$ and $\alpha = \beta = 3\pi/2$ both describe the ground state configuration (see Fig. 4.1) of non shifted dipoles, which is the parallel

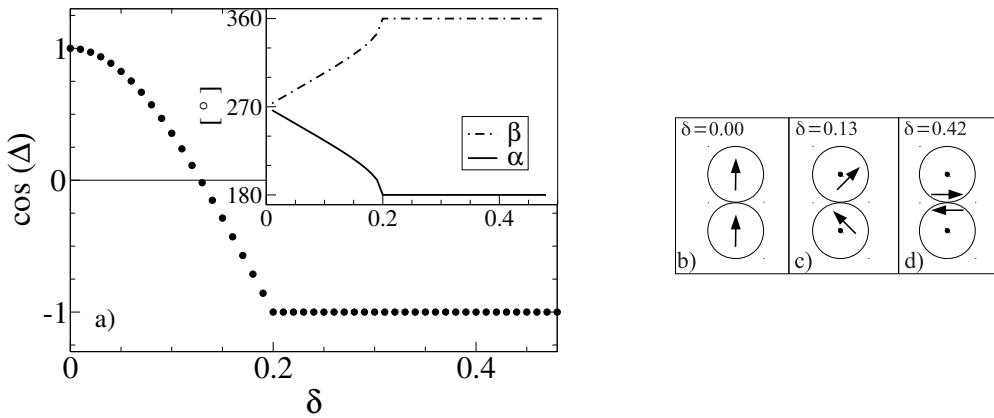


Figure 4.3.: (a) Simulated annealing results for the enclosed angle between the two dipoles in their ground states. The solid line indicates the zero line. The inset shows α and β as defined in Fig. 4.1 and gained by minimizing Eq. (4.1). (b)-(d) Ground state configurations of two dipoles for several shifts.

head-to-tail orientation. Here, we choose the latter set of initial values, $\alpha = \beta = 3\pi/2$, as a starting point for our examination.

Shifting the dipoles out of the centres, the parallel orientation of the dipoles is gradually abandoned in favour of reducing the dipolar distance. In detail, upon increasing δ from zero, α is reduced until it reaches the value π (see inset of Fig. 4.3 (a)). Correspondingly, β grows with increasing shift towards 2π , as shown in the inset of Fig. 4.3. In other words, with increasing shift, the upper particle in Fig. 4.3 (b) rotates clockwise while the lower one rotates counter-clockwise and α and β evolve in a completely symmetric manner. Thereby, Δ increases and $\cos(\Delta)$ decreases, reflecting that the dipoles more and more deviate from their parallel orientation. At the value $\delta \approx 0.13$, $\cos(\Delta)$ passes the zero line where $\Delta \approx \pi/2$ and the dipoles attain a perpendicular orientation. Finally, $\cos(\Delta)$ reaches its lowest value $\cos(\Delta) = -1$ (and thus $\Delta = \pi$) at $\delta = 0.2$. This corresponds to an antiparallel configuration of $\boldsymbol{\mu}_i$ and $\boldsymbol{\mu}_j$ relative to each other, and to a perpendicular orientation of each of the dipoles relative to the connecting line between the particle centres. For all higher shifts, the antiparallel orientation is kept and only the dipolar distance is further reduced. Interestingly, the value of $\delta = 0.2$ does not point any significance in the energy plot of Fig. 4.2 but is highly significant for the preferred orientation of the dipoles. Thus we conclude that $\delta = 0.2$ represents the border between the two regimes of parallel (small shifts) and anti-parallel (high shifts) orientations (consistent with [67]).

Compared to radially shifted dipoles of Ref. [43], the main difference in the ground state structures is that radially shifted dipoles keep their parallel head-to-tail orientation for small shifts. For large shifts, the two radially shifted dipoles also attain an antiparallel oriented relative to each other whereas at the same time, each dipole is orientated along the connecting line between the centres of the particles. This demonstrates that not only the location but also the orientation of the dipole vector within the particle plays a crucial role for the ground states of the particles as also confirmed in Ref. [83] in which the authors study the influence of shape and geometric anisotropy of the particles on their interaction.

4.0.6. Configurations for $N > 2$

The principle impact of shifting the dipoles out of the particles' centres, namely, the decrease of the ground state energy and a preferred non-parallel orientation of the dipoles with increasing shift, becomes even more pronounced in systems of three and four dipolar hard spheres.

For a detailed investigation, we have performed simulated annealing calculations to determine the ground state configurations of three-dimensional systems with three and four hard spheres for different shifts.

Three-particle configurations We first consider the three-particle case and sketch the obtained configurations in Figs. 4.4 (a)-(d).

For three particles, shifting the dipole has the same effect on the ground state energies and

configurations as for two particles. Thus, the former also rapidly decreases with increasing shift qualitatively in the same way as shown in Fig. 4.2 (and the same holds for the case $N = 4$).

Regarding the ground state configurations, starting from the chainlike head-to-tail orientation known for non shifted dipoles, the particles first organize into slightly curved chainlike geometries (Fig. 4.4 (b)). This occurs for very small shifts up to $\delta \approx 0.03$. Our simulation results show that the corresponding ground state energies for this curved chain configuration is slightly lower (see Table 4.1) than those for the corresponding structure proposed in Ref. [67] which the authors call a "zipper". In a "zipper" configuration the dipoles have head-to-tail orientation and are organized in a staggered manner.

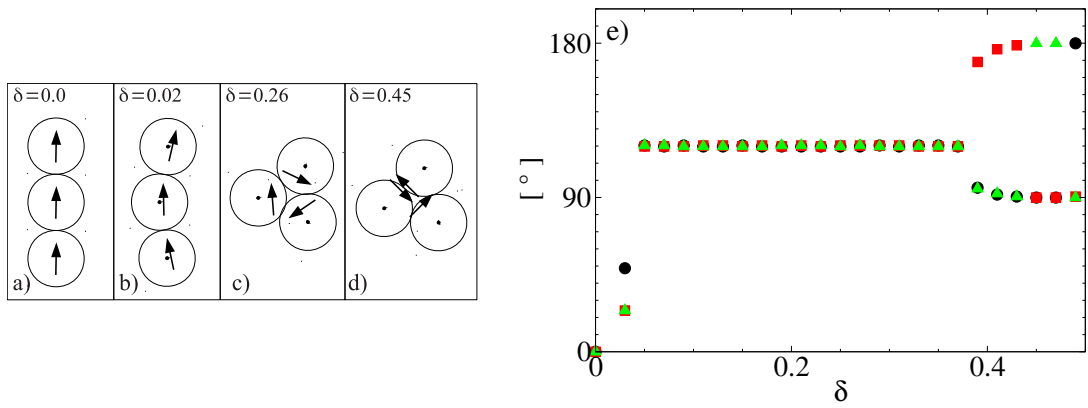


Figure 4.4.: (a)-(d) Ground state configurations of three particles. (e) Simulation results for the three pair angles occurring between each of the three dipolar pairs in the ground state configurations. Each symbol represents one pair angle, respectively. For rectangular dipolar configurations, e.g at $\delta = 0.45$ (see (d)), two of the angles approach 90° and the remaining one, accordingly, 180° .

When the shift takes values above $\delta \approx 0.03$, the two particles at the ends of the chain approach each other in such a way that they form a planar triangular arrangement. This behaviour remains for all higher shifts (Fig. 4.4 (c) and (d)), in agreement with the results of Ref. [67].

Table 4.1.: Ground state energies E_{gs} in a.u. for three dipolar hard spheres gained by simulations for very small shifts. The corresponding ground state configurations are sketched in Fig. 4.4 (b).

δ	E_{gs} in a.u.
0.0125	-4.2556
0.01875	-4.2667
0.02	-4.2722
0.025	-4.2911

In terms of the orientations of the dipoles within the particles, in the case of chainlike geometries, the dipoles show head-to-tail orientation. On the other hand, within the triangular geometries (Figs. 4.4 (c) and (d)), there are two qualitatively different types of dipolar orientations. The first type is likewise triangular with all the pair angles (i.e. the angles between the three dipolar pairs) attaining the value of 120° for shifts up to $\delta \approx 0.38$,

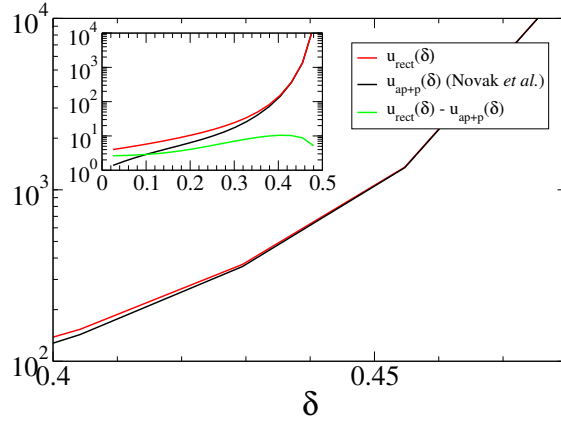


Figure 4.5.: Absolute values for $u_{rect}(\delta)$, $u_{ap+p}(\delta)$ [67] and for the difference $|u_{rect}(\delta)| - |u_{ap+p}(\delta)|$, in a.u., respectively.

as confirmed by the plot in Fig. 4.4 (e). The second type is a rectangular orientation in which two of the dipoles form an antiparallel pair and the third one joins the pair in a perpendicular manner (Fig. 4.4 (d)). Correspondingly, two of the three pair angles have a value of 90° and the third one of 180° , as shown in Fig. 4.4 (e). We note that at higher shifts $\delta > \approx 0.4$, we again find a difference to the results in [67]. The authors propose a configuration containing an antiparallel pair which is joined by the third particle via a head to tail orientation with one of the dipoles of the antiparallel pair. To clarify this issue, we have derived an analytical expression for the rectangular configuration shown in Fig. 4.4 (d). It is given by

$$u_{rect}(\delta) = -\frac{1}{(1-2\delta)^3} - \frac{3(1-2\delta)(\frac{\sqrt{3}}{2} - \delta)}{\sqrt{(1+2\delta^2 - \delta(1+\sqrt{3}))}^5}.$$

Evaluating this energy, we find that the rectangular configuration is energetically slightly more favourable than that of Ref. [67]. Figure 4.5 shows the results for the absolute values of $u_{rect}(\delta)$, the results for the absolute values of Eq. (7) of Ref. [67], $u_{ap+p}(\delta)$, and the difference $|u_{rect}(\delta)| - |u_{ap+p}(\delta)|$, which is positive for all values considered.

Configurations of Four Particles Finally, in the case of four particles, the non shifted ground state configuration is a ring geometry with rectangular, cyclic orientation of the dipoles, as it is known from other ground state studies [44] (see Fig. 4.6 (a)). This configuration remains for small shifts where only the dipolar distances are reduced while the orientations are maintained. In this arrangement, the dipolar interaction of the two nearest neighbours in the ring is equal in absolute value but of opposite sign. As soon as the shift takes values for which it is energetically favourable if opposing dipoles rather than

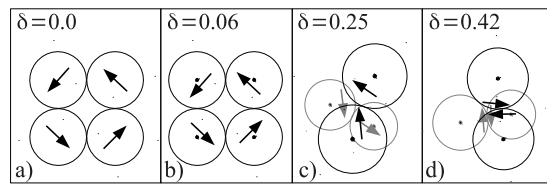


Figure 4.6.: Ground state configuration of four particles for several shifts δ .

neighbouring ones in the rectangular planar geometry reduce their distances, these opposing dipoles form a pair of antiparallel dipoles and move out of the plane, as sketched in Fig. 4.6 (c). If the shift is further increased, the dipoles of each of the two antiparallel pairs more and more approach. Finally, the particles of each pair are in close contact and the four particles form a tetrahedron consisting of two antiparallel pairs which are perpendicular oriented to each other (Fig. 4.6 (d)). Clearly, this is only possible in 3D. Thus, in the four particle system, we observe for the first time a cross-over from planar to 3D configurations. In q2D, the ground state configuration for all shifts is the ideal ring [67].

In conclusion, the four-particle system is the smallest system for which the dimensionality of the system is crucial for the resulting ground state structure at high shifts. While two and three particles always lie in a plane, four particles can arrange in a 3D structure.

4.0.7. Conclusion

The results for the ground state behaviour of the cases $N = 2$, $N = 3$ and $N = 4$ upon the increase of the shift has shown that shifting the dipole out of the particle centre has a crucial effect on the ground state configurations. These are determined by the relative arrangements of the particle centres, for specific values of δ , as well as by the relative organization of the dipoles. Thereby, the former is driven by the latter as a result of energy minimization via the minimization of the dipolar distance on the one hand and through the stepwise abandoning of the parallel head-to-tail orientation of the dipoles on the other hand.

While the arrangement for the case $N = 2$ does not change upon the increase of δ (only the orientations of the dipoles within the particles change), for $N = 3$, qualitatively new arrangements are generated, i.e. a structural transition from chainlike to triangular is observed. Finally, for $N = 4$, the shift yields an additional feature of the upcoming structures, namely, while for $N < 4$, all occurring structures are exceptionally planar, $N = 4$ is the smallest system in which the generation of 3D structures (i.e. tetragonal ones) are feasible for the first time, if the shift is sufficiently large.

5

Equilibrium Self-assembly

Having understood the main features of the effect of the shift on the ground state configurations, we now aim at studying the effect of δ on the self-assembly of shifted dipoles in more realistic systems. Thus, in this section, we investigate three-dimensional bulk systems of shifted dipoles at finite temperatures with soft-sphere repulsive interactions, which seem more realistic for the real colloidal particles mentioned in the introduction. To this end, we set in Eq. (2.5) the parameters $\epsilon = 50$ and $n = 38$.

Due to the fact that the magnitude of the ground state energy $E_G(\delta)$ is an increasing function of the shift (see previous discussions), also the dipolar coupling strength λ , which is defined as the ratio of the half ground state energy and the thermal energy, $\lambda(\delta) = |E_G(\delta)|/2k_B T$, becomes an increasing function of the shift. This yields an irreversible agglomeration of the particles, which cannot be counteracted by the soft-core potential. For the present choices for ϵ and n , this situation occurs if the shift exceeds the value of $\delta = 0.33$. We examined higher shifts than $\delta = 0.33$ by appropriate choices for ϵ and n but did not gain any new insights of the system beyond those already observed for smaller shifts. Therefore, instead of adjusting $\lambda(\delta)$, e.g. by appropriate reduction of μ^* with increasing shifts, or instead of enhancing the soft-sphere potential values ϵ and n , we limit the shift at $\delta_{limit} = 0.33$ in order to prevent agglomeration. In this way the structural properties of the system can be directly related to the amount of shift which hence is the parameter of interest in our examinations.

In order to roughly estimate which value for δ corresponds to real magnetic Janus particles such as studied in Ref. [84], we conducted test simulations of particles with various shifts in a static magnetic field (corresponding to the experimental situation considered in

Fig. 1c of Ref. [84]). There, the particles organize in a staggered chain configuration with head-to-tail orientation of the dipoles. The angle θ between neighbouring centre-to-centre distance vectors in the staggered chain configuration was measured as a function of the offset of the dipole moment from the particle centres [84]. Evaluating snapshots of our test simulations, we found, by comparing with the measurements of Ref. [84], that values in the range between $\delta \approx 0.25$ and $\delta \approx 0.3$ qualitatively describe Janus particles. In a perfect staggered-chain-configuration, one has $\cos(\theta/2) = 2\delta$. For $\theta \approx 110^\circ$ [84], corresponding to the smallest thickness [84] of nickel coating, this expression yields the value $\delta \approx 0.287$. This confirms that considering shifts larger than our limiting value $\delta > 0.33$, does not have experimental relevance.

In the following, we consider a strongly coupled system with $\mu^* = 3$ with the densities $\rho^* = 0.07$, $\rho^* = 0.1$ and $\rho^* = 0.2$ and at the two temperatures $T^* = 1.0$ and $T^* = 1.35$, respectively. This yields coupling strengths ranging from $\lambda(\delta = 0) = \mu^2/(k_B T \sigma^3) = 9$ to $\lambda(\delta = 0.33) = 72$ for $T^* = 1.0$, and $\lambda(\delta = 0) \approx 6.67$ to $\lambda(\delta = 0.33) \approx 53.33$ for $T^* = 1.35$. For a thorough investigation of the equilibrium properties of the shifted system, we performed MD simulations as described in Sec. 3.1 and calculated various structural properties which we specify in the appropriate sections.

5.1. Classification of the Occurring Structures

For a first overview, we present in Fig. 5.1 representative MD simulation snapshots illustrating typical self assembling structures. Specifically, we consider systems at $T^* = 1.0$ and $\rho^* = 0.1$ for $\delta = 0$, $\delta = 0.21$ and $\delta = 0.33$.

Qualitatively, the structures appearing for the considered values of δ can be divided into four groups. These are chains (A), staggered chains (B), rings built by staggered chains (C) and small clusters (D) of the types presented in Figs. 4.2 (d), 4.4 (c) and 4.6 (c). Structures of type (A) can consist of a few (e.g. 2 – 5) as well as of many (more than e.g. 10) particles, i.e., the chains can be short or long. Structures of types (B) and (C) always consist of more than e.g. 10 particles (Fig. 5.1 (d), (e)). In accordance with the ground state configurations (see Figs. 4.4 and 4.6), the structures found in the finite temperature systems for different shifts pass from chainlike geometries to circular close-packed clusters upon the increase of δ . Accordingly, structures of the first group are formed for zero and small shifts in the range $\delta = 0.01 - \delta \approx 0.1$ (Fig. 5.1 (a) and (d)). In this shift region, the overall chainlike structure with head-to-tail orientation as formed by non shifted dipoles is maintained. Yet, the shift causes more and more curved structures compared to the non shifted particles. As is generally known for dipolar systems, the chain length, i.e. the number of particles within a chain, has a poly disperse distribution [26]. This holds also for the shifted system (see also the discussion of the cluster analysis in Sec. 5.2.2).

For intermediate shifts, e.g. $\delta = 0.24$, Fig. 5.1 (b) and (e), the particles within the chains become staggered and we observe coexistence of structures of the types (B), (C) and (D).

Structures of group (D) are consistent with the ground state configurations of this and higher shifts. Although groups (B) and (C) are not observed for zero temperature, they can be understood as a modification of chains, as they appear for small δ , and of rings which occur at zero temperature.

If δ takes values near 0.33, all large aggregates (B) and (C) vanish and only small clusters (D) remain, as shown in Figs. 5.1 (c) and (f).

The same structural behaviour at the different shift regions is observed for the other state points considered. Thus we conclude that the described self-assembly of the particles at different shifts is a quite general behaviour which results from the increasing dipolar coupling strength for increasing shifts. The latter causes more and more close-packed structures as we already confirmed in the case of hard spheres.

5.2. Structural Analysis

5.2.1. Radial distribution function

As a first quantitative measure of the structure formation, we consider the radial distribution function

$$g(r) = \frac{\langle \sum_{i \neq j} \delta(r - r_{ij}) \rangle}{N\rho 4\pi r^2}$$

for several shifts.

The plots in Fig. 5.2 show $g(r)$ for $\delta = 0$, $\delta = 0.19$ and $\delta = 0.33$ for $T^* = 1.0$ and $T^* = 1.35$. The $g(r)$ at zero shift is dominated by first and second neighbour correlations. This is a typical feature of strongly coupled dipolar systems [85, 81] and reflects the formation of chain-like structures. Slightly different from conventional dipolar systems is the locations of the first and second peaks which indicates that the distances between the particles within the chains are increased compared with conventional non-shifted dipolar soft spheres (e.g. [86, 85, 87, 81]). Clearly, the reason for that is our choice of the parameters ϵ and n of the soft-sphere potential which prevents the particles of further approaching each other. For increasing density as well as at the higher temperature $T^* = 1.35$, the ability to build chains decreases which is consistent with known works on dipolar systems [86, 88].

When we successively increase the shift, the second peak of $g(r)$ for $\delta = 0$ wanders towards the first one by gradually becoming diminished in size as shown in Figs. 5.2 (a) and (b). The plots also show that the first peak is enhanced for increasing shifts, displaying that chains, more specifically larger aggregates, in the small shift region are step by step given up when the intermediate shift region is reached.

Noticeably, the results for the higher temperature $T^* = 1.35$ completely coincide with those of $T^* = 1.0$ in the high shift region (Fig. 5.2 (b) and (d)). This is because for sufficiently high shifts, the increase of the dipolar coupling strength is already enhanced and thus, the

increase of temperature does not affect the self-assembly.

Finally, in the high shift region (Figs. 5.2 (c) and (f)), the first peak of $g(r)$ is further enhanced compared to the preceding shift regions and is located at $r^* = 1$ signifying closely attached particles within the clusters, which is equivalent with the presence of only nearest neighbour correlations. This in turn reflects the presence of only small and close-packed clusters (D) shown in the snap shots of Fig. 5.1 (c). Overall, the observation that the system passes from a state with large structures to small clusters by increasing δ (see Fig. 5.1) is confirmed by the results of $g(r)$.

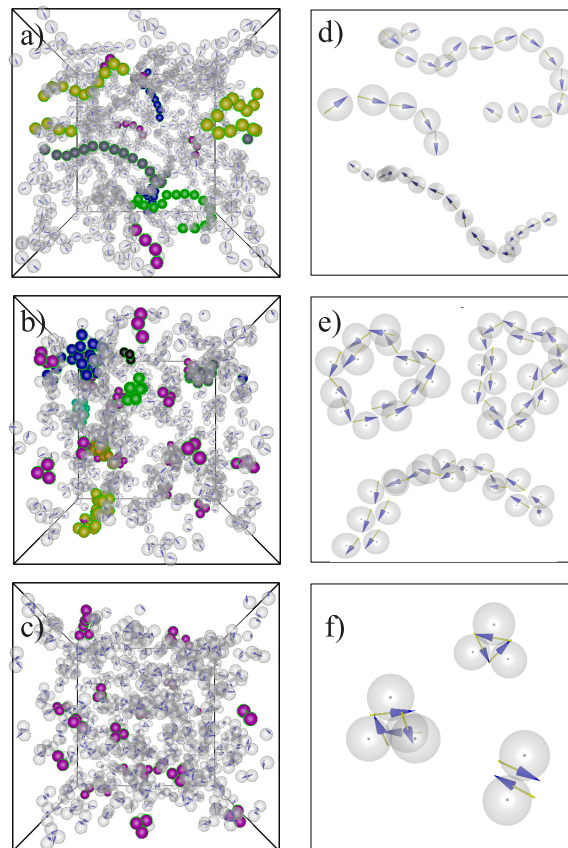


Figure 5.1.: Snapshots for $\delta = 0$ (a), $\delta = 0.21$ (b) and $\delta = 0.33$ (c) with revealing structures of the group (A) (a), the groups (B), (C) and (D) (b) and only (D) (c). In each snapshot, some randomly chosen clusters are coloured for a better visibility. Particles of the same colour besides magenta belong to the same cluster. Magenta coloured clusters represent small single clusters (D). (d)-(f) Magnification of randomly chosen clusters of the snapshots in the left column.

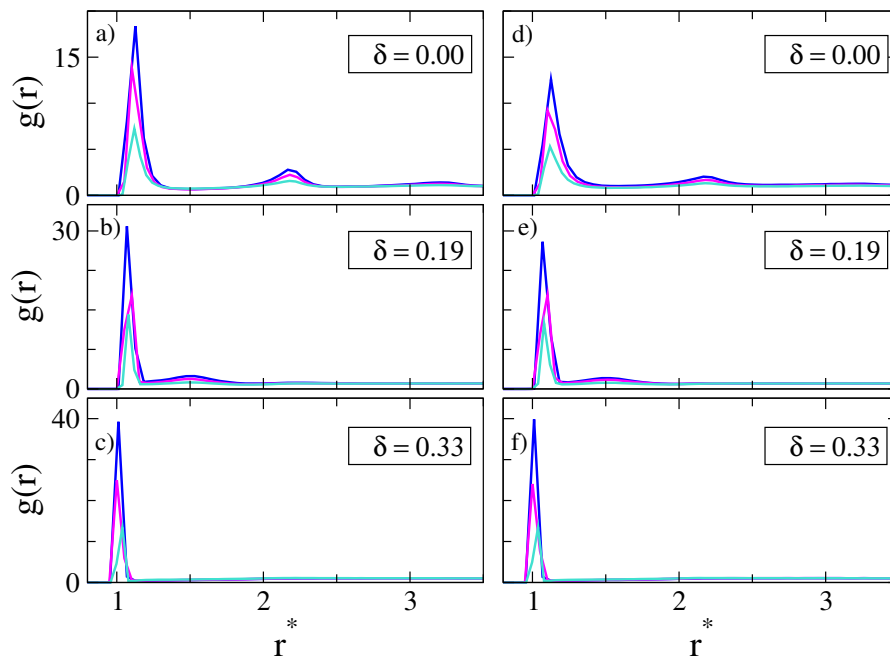


Figure 5.2.: Radial distribution functions $g(r)$ for densities $\rho^* = 0.07$ (blue), $\rho^* = 0.1$ (magenta) and $\rho^* = 0.2$ (turquoise) at two temperatures $T^* = 1.0$ ((a)-(c)) and $T^* = 1.35$ ((d)-(f)).

5.2.2. Cluster analysis

To further characterize the aggregates, we perform a cluster analysis. In particular, we are interested in the cluster size distribution for several shifts, the mean cluster size and the mean cluster magnetization as a function of δ . The basis of this analysis are distance and energy criteria. Specifically, all particles with a distance lower than $r_c = 1.3\sigma$ and binding energy $u_c = \sum_{i,i'>i} u_{DD}^{ii'} < 0$ are regarded as being clustered. Here, $u_{DD}^{ii'}$ denotes the dipolar energy (see Eq. (2.4)) between all pairs i, i' within the critical distance r_c .

The detected clusters were collected in a histogram in which the number of clusters with size S , $n(S)$, is counted and normalized by the total number of clusters, $N_c = \sum_{S \geq 2} n(S)$, such that

$$h(S) = \left\langle \frac{n(S)}{N_c} \right\rangle,$$

gives the normalised cluster size distribution. Only $S \geq 2$ enters to the sum, i.e., single particles are disregarded.

Based on the function $n(S)$, the mean cluster magnetization is calculated by

$$\langle M \rangle = \left\langle \frac{\sum_{S \geq 2} n(S) \cdot M_c(S)}{N_c} \right\rangle,$$

where $M_c(S) = \left| \sum_{i=1}^S \boldsymbol{\mu}_i / (\boldsymbol{\mu} \cdot S) \right|$ gives the normalized magnetization of a cluster with size S . The quantity $M_c(S)$ is a measure of parallel alignment of the dipole vectors within the individual clusters. Specifically, values of $M_c(S)$ near to one reflect a high degree of head to tail orientation, while vanishing values of this quantity indicate antiparallel or triangular orientation. Therefore, the mean cluster magnetization gives inside into the organization of the dipoles within the formed structures and thus allows to evaluate if a given assembly is chainlike (types (A) and (B)) or closed (types (C) and (D)). Note that the total magnetization, which is usually calculated by summing over all particles, has vanishing values as the system is globally isotropic at the state points considered here.

Finally, the mean cluster size is obtained from

$$\langle S \rangle = \left\langle \frac{\sum_{S \geq 2} n(S) \cdot S}{N_c} \right\rangle.$$

Normalised cluster size distribution The results for $h(S)$ for different characteristic shifts, namely for $\delta = 0.1$ (small shift), $\delta = 0.16$ (intermediate shift) and $\delta = 0.27$ (high shift) are presented in Fig. 5.3. The figures 5.3(a) and (d) show that mostly large aggregates, that can contain up to 25 – 30 particles, are formed. On the other hand, Figs. 5.3 (c) and (f) indicate the formation of only small assemblies with 3 – 4 particles. However, in Fig. 5.3 (b) and (e), although there is a preferential emergence of small

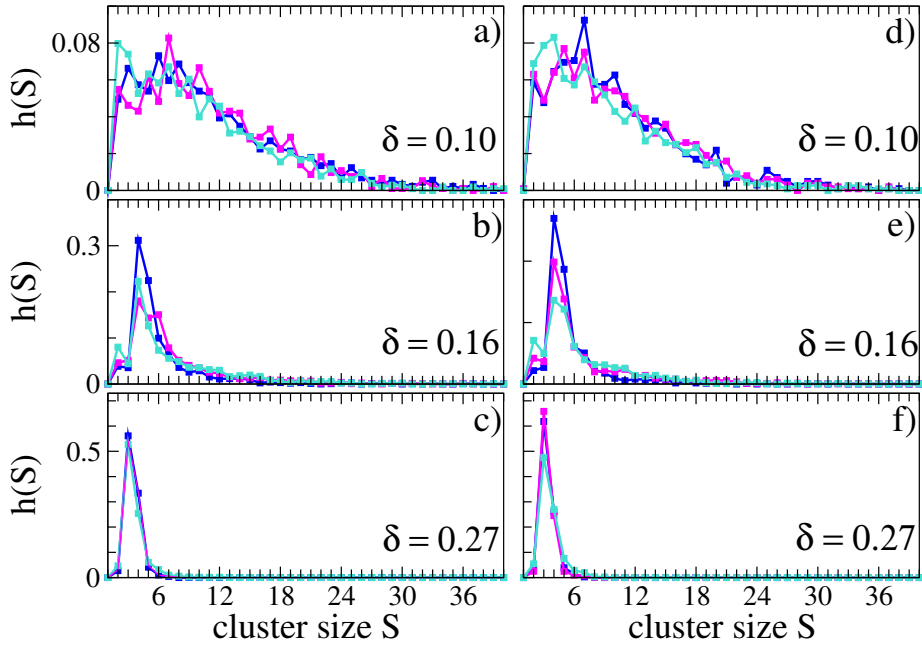


Figure 5.3.: Normalized cluster size distribution for the same densities and colours as in Fig. 5.2. (a)-(c): $T^* = 1.0$. (d)-(f): $T^* = 1.35$.

assemblies, large aggregates of up to 20 particles are present in a non-negligible number and secondary peaks at e.g. $S = 15$ (for $T^* = 1.0$) and $S = 13$ (for $T^* = 1.35$) are visible. Evidently, for this and comparable shifts, small and large assemblies can coexist.

One also finds that for higher temperature, large aggregates are less often formed than for the smaller temperature. This is indicated by the fact that the peaks in Figs. 5.3 (e) and (f) are enhanced compared to those in Figs. 5.3 (b) and (c).

Means of the cluster size and cluster magnetization

(a) *Mean cluster magnetization.* In order to evaluate the types of the occurring structures for a given shift, we determine $\langle M \rangle$ as a function of the shift and plot the results in Figs. 5.4 (b) and (d).

For zero and initial shifts, $\langle M \rangle$ takes the value ≈ 0.7 , reflecting predominantly parallel orientation of the dipoles within their aggregates. From this and from the cluster size distribution (Fig. 5.3 (a),(d)) we conclude that for small shifts (up to $\delta \approx 0.1$), mainly short and long polar chains of type (A) or (B) are formed.

If the shift is further increased, $\langle M \rangle$ decreases, indicating that polar chains occur less often. Instead, the aggregates become more and more closed structures of the types (C) or (D) with increasing shifts. Hence, the decrease of $\langle M \rangle$ implies the coexistence of types (B), (C) and (D) (see Figs. 5.1 (b) and (e)). At the high shift end, $\langle M \rangle$ drops down to vanishing

values indicating only pairwise antiparallel or triangular arrangements of the dipoles within the clusters, which is also consistent with the results shown in Fig. 5.3 (c) and (f). The fact that the mean cluster magnetization has vanishing values at large δ also suggests that the clusters poorly interact.

Note that for all values of δ , the according aggregates are isotropically oriented such that the total magnetization is zero for all shifts (not shown here).

(b) *Mean cluster size.* Finally, we examine the influence of the shift on the mean cluster size and plot in Figs. 5.4 (a) and (c) $\langle S \rangle$ as a function of the shift.

Starting at $\delta = 0$, the mean cluster size grows to its maximum with about 17 particles for $T^* = 1.0$ and about 13 particles for $T^* = 1.35$. The maximum is reached at $\delta \approx 0.05$, respectively. This increase can be understood by the effective increase of the dipolar coupling strength λ (see preceding discussion) such that initial shifts result in the formation of longer chains of type (A). If δ exceeds this value, $\langle S \rangle$ starts to gradually decrease because with increasing shift, smaller aggregates are formed more frequently (see Fig. 5.3). Finally, $\langle S \rangle$ attains the value of about 3 particles in the high shift end, which is a highly representative value for both temperatures considered (Figs. 5.3 (c) and (f)). Significant differences between the results of the two temperatures can be seen only for shifts smaller than $\delta \approx 0.1$ where mainly chainlike aggregates are formed. Here, the increase of temperature, which involves the decrease of the coupling strength from $\lambda = 9$ to $\lambda \approx 6.67$, causes the formation of chains with less particles. Moreover, for these values of δ , shifting the dipoles does not impose fundamentally different self-assembly patterns compared to non shifted dipoles. Therefore, small shifts can be regarded as perturbation of the non shifted system.

On the other hand, high shifts impose significantly different structures: the particles exclusively form structures of type (D) that correspond to ground state configurations of two, three and four hard spheres (see Figs. 4.2 (d), 4.4 (c) and 4.6 (c)). This is possible due to the large values of $\lambda = 72$ for $T^* = 1$ or $\lambda \approx 53.33$ for $T^* = 1.35$.

Finally, for intermediate shifts, where large aggregates as well as small clusters are formed, the decrease of $\langle S \rangle$ (and at the same time of $\langle M \rangle$) can be interpreted as a transition region in which large aggregates gradually dissolve into small clusters until no large structures appear at all. Within this region, the competition between energy minimization and entropy maximization results in the coexistence of both, small and large aggregates. With increasing shift (i.e., effectively increasing $\lambda(\delta)$), the particles accomplish to form structures equivalent to ground state configurations.

To summarize, in the bulk systems at the finite temperatures and densities considered here, we can qualitatively distinguish between three shift regions (small, intermediate and high) each of which is characterized by it's own structural characteristics. By contrast, in the ground states of two particles, we determined only a small (with head-to-tail dipolar order) and a high (with antiparallel dipolar orientation) shift region. The intermediate shift region,

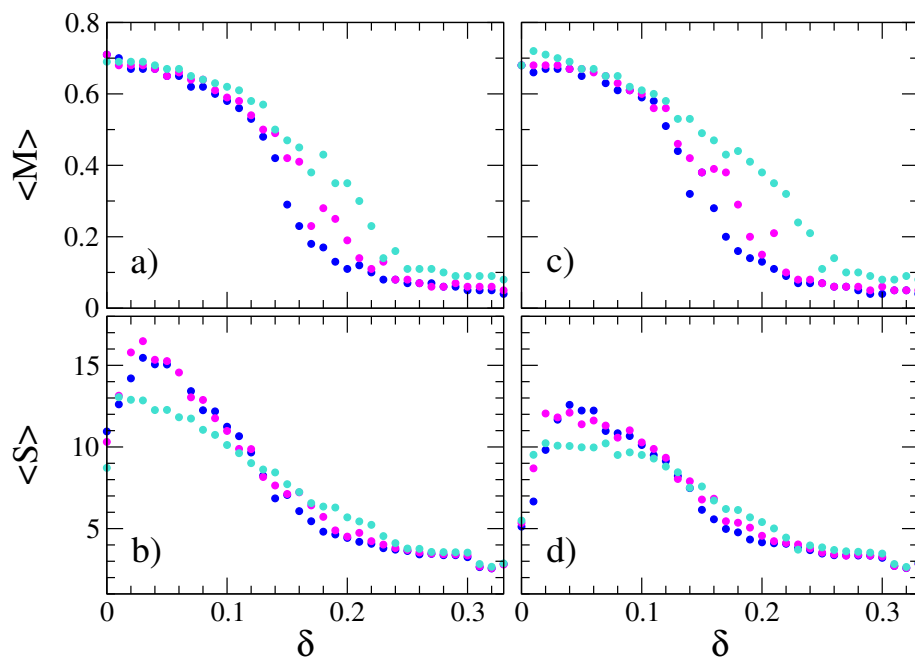


Figure 5.4.: Mean cluster size $\langle S \rangle$ and mean cluster magnetization $\langle M \rangle$ as a function of the shift at two temperatures $T^* = 1.0$ ((a),(b)) and $T^* = 1.35$ ((c),(d)). Colours are the same as in Fig. 5.2.

observed for the bulk systems is not detected for zero temperature. This is consistent with the fact that the corresponding structures of types (B) and (C) are not observed in the ground state calculations.

5.3. Conclusion

Self-assembly in a three-dimensional system of shifted dipoles is highly determined by the amount of shift δ . Thus, the occurring aggregates can be divided in three groups being chainlike for very small shifts, closed rings for intermediate shifts and small and close-packed clusters of dimers, trimers and tetramers for shifts near the limit value $\delta = 0.33$. This decrease of the mean cluster size and the decay of the mean cluster magnetization with increasing shifts is a result of the increase of the dipolar coupling strength $\lambda(\delta)$, which thus directs the clusters from large to small ones. Specifically in the small shift region up to $\delta \approx 0.1$, the shift can be overcome easily and the aggregates do not much differ from that of the non shifted system. Thus, the small shift region can be recognized as a perturbation of the non shifted system. Consequently, shifting the dipoles only becomes noticeable in the intermediate shift region and definitely fundamentally affects self-assembly in the high shift region, by the generation of qualitatively new types of self-assembly (e.g. closed rings or small clusters, respectively). Thereby, it is an interesting observation that the asymmetry of the particles, caused by the offset of the dipole moment, is compensated in the high shift region by building symmetric aggregates such as dimers, trimers and tetramers.

6

Nonequilibrium pattern formation

In this chapter, we apply an external rotating magnetic field (see Eq. (2.13)) to the three-dimensional system of shifted dipoles which we studied in the previous chapter. The external field drives the system far out of equilibrium and for the non shifted system, former studies [71] yielded that a steady state, being characterized by a layered structural order of the particles parallel to the rotating plane, is established through the synchronization of the dipoles with the external field.

Thus, we now go one step further and study in the non equilibrium system the effect of shifting the dipoles on pattern formation as well as on synchronization, which is a non equilibrium phenomenon.

To this end, we use LD simulations, as described in section 3.2 in order to take the solvent into account in a more realistic way. Specifically, we consider a strongly coupled system with $\mu^* = 3$ with the fixed density $\rho^* = 0.1$ and at the temperature $T^* = 1.35$. This state point belongs to the isotropic state in the phase diagram of the non shifted system in equilibrium and was considered in the earlier study of this system, which is why we use this state point as a starting point. For the coupling strengths, this yields values ranging from $\lambda(\delta = 0) \approx 6.67$ to $\lambda(\delta = 0.33) \approx 53.33$. To our knowledge, our study of three-dimensional systems with laterally shifted permanent dipoles in a time-dependent external field is the first of this type.

6.1. Time-averaged Dipolar Potential U^{ID} for Shifted Dipoles

The first question which arises if an external rotating magnetic field is applied to a system of shifted dipoles is whether layer formation, known from centred dipoles in a rotating magnetic field [71], is still possible if the dipoles are shifted out of the particles' centres. The crucial mechanism leading to layer formation in the centred system is the behaviour of the time-averaged dipolar pair potential U^{ID} of *synchronized* dipoles [71]. Therefore, in order to examine the question how layer formation is affected by the shift of the dipole, we derive U^{ID} for shifted dipoles, i.e., as a function of δ . This is done equivalently to the centred system which we refer to as "reference system" in the following.

Like in the case of a pair of centred dipoles (see appendix A), also for a pair of dipolar spheres with synchronized shifted dipoles $\boldsymbol{\mu}_i$ and $\boldsymbol{\mu}_j$, Eq. (A.1) holds. However, unlike centred dipoles, the relation $\mathbf{r}' = \mathbf{r}$ for the dipolar distance vector is not necessarily valid. Thus, it is essential to study the influence of the shift on \mathbf{r}' for the synchronized case. To this end, we first exemplarily consider a single synchronized shifted dipolar particle i .

For a shifted synchronized dipole, the perpendicular geometry of $\boldsymbol{\mu}_i$ and \mathbf{d}_i restricts the shift vector \mathbf{d}_i to the plane perpendicular to the direction of the field, in the following called "perpendicular field plane" (see Fig. 6.1). Yet, within this plane, the orientation of the shift vector is a degree of freedom because it does not change the orientation of $\boldsymbol{\mu}_i$ and thus does not prevent its synchronization with the external field. To cover this condition, we introduce a field-fixed coordinate system, $K^{\mathbf{B}}$, the z -axis of which coincides with the field vector \mathbf{B} at any time such that it rotates w.r.t. the laboratory frame with the field frequency ω_0 . The unit vectors of $K^{\mathbf{B}}$ in the laboratory frame are then given by

$$\mathbf{e}_x^{\mathbf{B}} = (-\sin \omega_0 t, \cos \omega_0 t, 0) \quad (6.1)$$

$$\mathbf{e}_y^{\mathbf{B}} = (0, 0, 1) \quad (6.2)$$

$$\mathbf{e}_z^{\mathbf{B}} = (\cos \omega_0 t, \sin \omega_0 t, 0), \quad (6.3)$$

where the vectors $\mathbf{e}_x^{\mathbf{B}}$ and $\mathbf{e}_y^{\mathbf{B}}$ span the perpendicular field plane. This yields for the shift vector in the laboratory frame

$$\mathbf{d}_i^L = d_{ix}^{\mathbf{B}} \cdot \mathbf{e}_x^{\mathbf{B}} + d_{iy}^{\mathbf{B}} \cdot \mathbf{e}_y^{\mathbf{B}} \quad (6.4)$$

with $d_{ix}^{\mathbf{B}2} + d_{iy}^{\mathbf{B}2} = d^2 = |\mathbf{d}_i|^2$.

Furthermore, the shift vector in $K^{\mathbf{B}}$ is given by

$$\mathbf{d}_i^{\mathbf{B}} = d \cdot (\cos \Phi_i, \sin \Phi_i, 0) = (d_{ix}^{\mathbf{B}}, d_{iy}^{\mathbf{B}}, 0),$$

where Φ_i is the polar angle of \mathbf{d}_i in $K^{\mathbf{B}}$.

With these relations, the dipolar distance $\mathbf{r}' = \mathbf{r} + \mathbf{d}_j^L - \mathbf{d}_i^L$ between a pair of dipoles i and j reads as

$$r'^2 = r^2 \cdot [1 + 2\epsilon^2(1 - \cos(\Phi_i - \Phi_j)) + 2\epsilon \sin \theta (\cos \Phi_i - \cos \Phi_j) \sin(\omega_0 t - \phi) - 2\epsilon \cos \theta (\sin \Phi_i - \sin \Phi_j)] \equiv r^2 \cdot \tilde{r}^2 \quad (6.5)$$

with $\epsilon = d/r$ and $r' = |\mathbf{r}'|$, and the angles θ and ϕ are defined in Fig. A.1 in the appendix. Consequently, it turns out that for a fixed particle distance vector \mathbf{r} and fixed shift vectors $\mathbf{d}_i^{\mathbf{B}}$ and $\mathbf{d}_j^{\mathbf{B}}$, the dipolar distance varies in time such that $\mathbf{r}' = \mathbf{r}'(t)$. In Fig. 6.2 (a), this is illustrated for an exemplary situation.

Although the dipolar distance is time-dependent in general, there are configurations which remove this time dependency, as Eq. (6.5) shows. These are

(I) $\Phi_i = \Phi_j$

(II) $\Phi_i = \frac{\pi}{2}$ and $\Phi_j = \frac{3\pi}{2}$

(III) vice versa of (II),

for which $\mathbf{d}_i = \mathbf{d}_j$ holds (I) and thus $\mathbf{r}' = \mathbf{r}$, or which correspond to (parallel or antiparallel, respectively) orientations of \mathbf{d}_i and \mathbf{d}_j along the laboratory's z -axis ((II) and (III)). As an example, the configuration (II) is illustrated in Fig. 6.2 (b). Having derived the expression for the dipolar distance (Eq. (6.5)), the dipolar potential for a pair of perfectly synchronized shifted dipoles at a fixed centre-to-centre distance of the particles finally can be written as

$$u_{DD}(\tilde{r}(t), t) = \frac{\mu^2}{r^3} \left(\frac{1}{\tilde{r}^3(t)} - \frac{3 \sin^2 \theta \cos^2(\omega_0 t - \phi)}{\tilde{r}^5(t)} \right) \quad (6.6)$$

which yields for U^{ID} (see Eq. (A.2)) the modified expression

$$U^{ID} = \tau^{-1} \int_{t_0}^{t_0 + \tau} u_{DD}(\tilde{r}(t), t) dt = U^{ID}(\epsilon, \Phi_i, \Phi_j, \theta). \quad (6.7)$$

The average dipolar potential U^{ID} , that means after performing the integration in Eq. (6.7), is a function of the independent parameters ϵ , Φ_i , Φ_j and θ .

6.2. Numerical Results for U^{ID}

Accept for the special cases (I), (II) and (III) (see above), the integration in Eq. (6.7) involves some difficulties which arise from the time-dependency of the dipolar distance

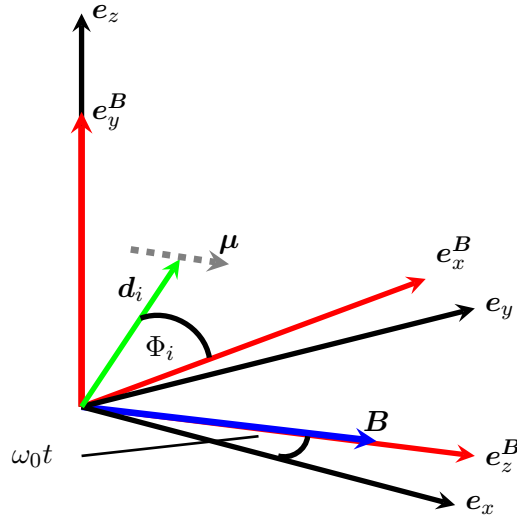


Figure 6.1.: Illustration of the field-fixed coordinate system K^B (red axes) and the configuration of the shift vector \mathbf{d}_i in K^B . The dipolar vector (dashed arrow) is for any value of Φ_i parallel to \mathbf{B} , thus, the orientation of \mathbf{d}_i in the "perpendicular field plane", spanned by e_x^B and e_y^B , is a degree of freedom.

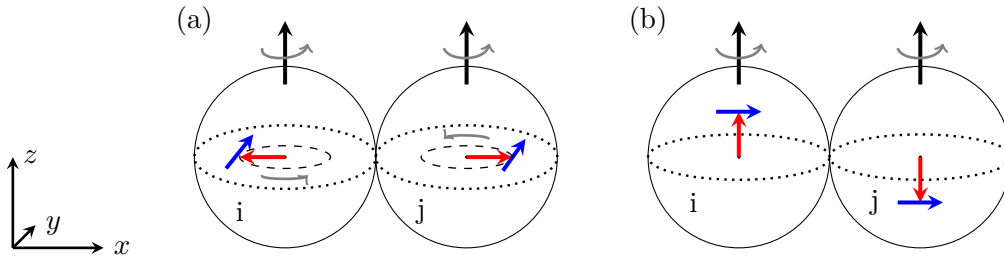


Figure 6.2.: Two pairs with $\theta = 90^\circ$. The surface normal of the "perpendicular field-plane" is parallel to the dipole vectors (blue). Black arrows indicate particle axes and the shift vectors are symbolized by red arrows, respectively. For perfect synchronization, the dipole vectors are always parallel to the field (not drawn). The gray arrows indicate the rotational direction of the particles due to synchronized rotations of the dipoles. (a) Configuration with $\Phi_i = 0$, $\Phi_j = \pi$, i.e. maximum dipolar distance (see Eq. (6.5)) becoming minimal after a half rotation. (b) Configuration (II), thus constant dipolar distance during the course of rotations.

appearing in the denominator of the two terms of Eq. (6.6). In order to avoid these, we perform the integration numerically for several sets of the free parameters ϵ , Φ_i , Φ_j and θ for a pair of shifted particles in close contact, i.e. with $r = 1\sigma$, thus $\epsilon = \delta$. In the following, we discuss the different dependencies of U^{ID} on its free parameters and show the results in Fig. 6.3.

We start the discussion with the dependency on θ . As Fig. 6.3 shows, configurations of the particle centres with $\cos(\theta)$ near zero correspond to exceptionally positive values for U^{ID} (repulsion) while configurations with $|\cos(\theta)| \approx 1$ or equal one are exceptionally attractive for all Φ_i and Φ_j , respectively (see the figures in the top and bottom lines of Fig. 6.3). For values of θ at medium level, e.g. $\theta = 60^\circ$, U^{ID} is attractive or repulsive depending on the values of Φ_i and Φ_j .

As discussed in the previous section (see Eq. (6.7)), Φ_i and Φ_j , i.e. the orientations of the shift vectors of a pair of synchronized dipoles in the perpendicular field plane, are free parameters. However, their relative values q.r.t each other is crucial for the value of the dipolar interaction between the pair (see Eqs. (6.5) and (6.6)). This yields an anisotropy of U^{ID} w.r.t. the mutual orientations of the shift vectors in addition to that q.r.t θ . Thus, U^{ID} is especially attractive or less repulsive for certain combinations of Φ_i and Φ_j (for θ fixed). For example for $\theta = 60^\circ$ and $\delta = 0.1$, U^{ID} is most attractive if the particles i and j orient antiparallel along the \mathbf{e}_y^B -axis thus with $\Phi_i = 270^\circ$ and $\Phi_j = 90^\circ$. For these values, the shift vectors point towards each other, i.e the dipolar distance is minimized, and the dipoles have an almost head-to-tail orientation which minimizes the dipolar potential (staggered chain configuration). Moreover, this configuration matches case (III), i.e. the dipolar distance is time-independent, and thus indicates a stable configuration. On the other hand, if Φ_i and Φ_j are exchanged (case (II)), the orientation of the dipolar distance vector \mathbf{r}' becomes unfavourable for the dipolar interaction.

Finally, a variation of δ enhances the anisotropy of the potential mentioned above such that, given a fixed value of θ in the intermediate range, the region of preferred orientations in the Φ_i/Φ_j -space enlarges while at the same time U^{ID} for these orientations is strengthened (Fig. 6.3).

Conclusion Compared to the reference system, the θ -dependency of the time-averaged dipolar potential, more specifically the anisotropy of U^{ID} w.r.t. θ , for the shifted system is qualitatively the same as for the reference system. That means, also for the shifted case, two particles attract or repel each other for appropriate values of θ . Therefore, we expect that systems with $\delta > 0$ generally also show layer formation if the particles are perfectly synchronized with the rotating field.

Furthermore, the additional degrees of freedom inherent to the shifted system, namely the orientations of the shift vectors in the perpendicular field plane, create an additional anisotropy of U^{ID} in such a way that specific mutual orientations of the shift vectors of a pair are energetically favoured. These orientations correspond to configurations which

cancel or reduce the time-dependency of the dipolar distance of a pair.

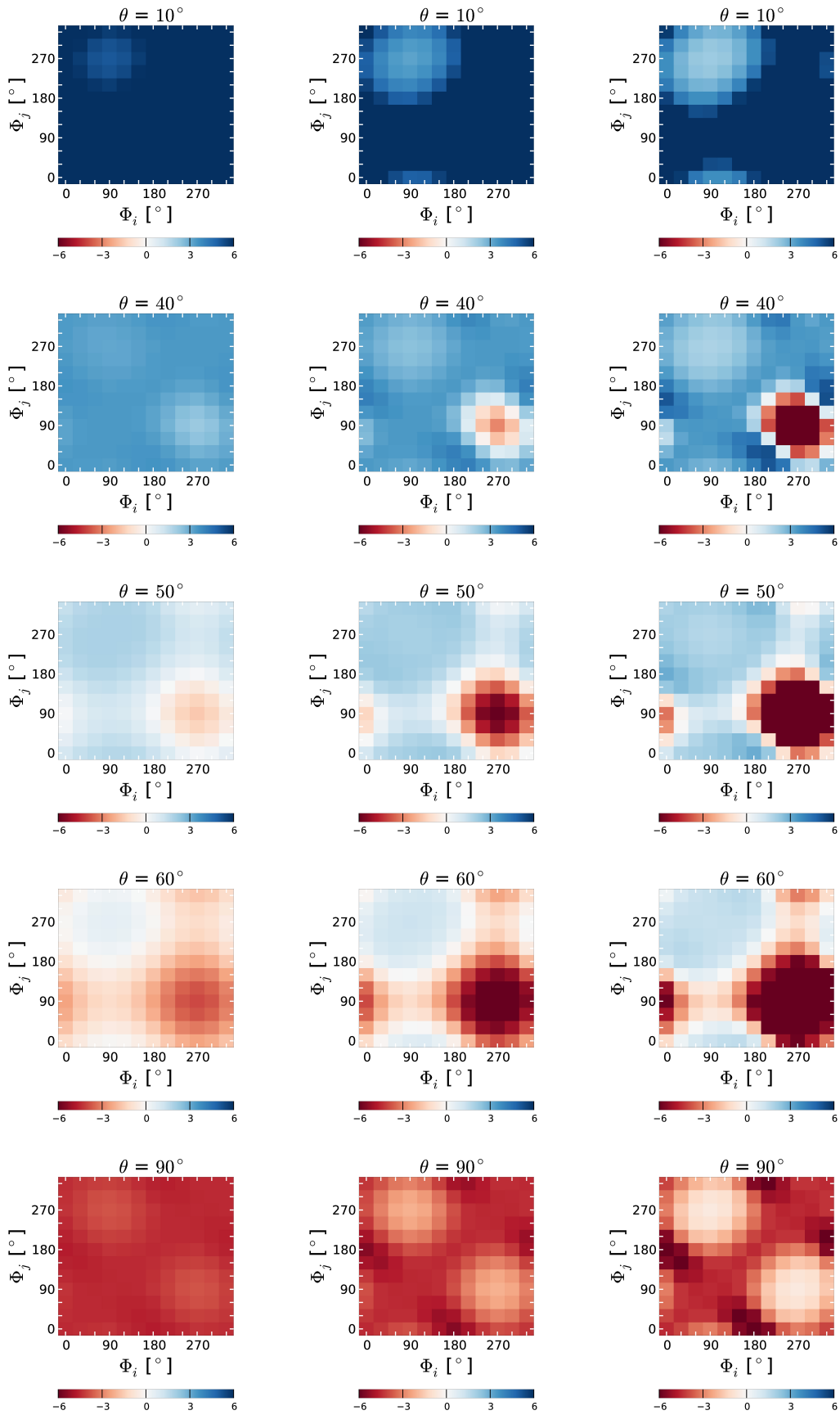


Figure 6.3.: Numerically calculated results of Eq. (6.7) for $\delta = 0.1$ (left column), $\delta = 0.2$ (middle column) and $\delta = 0.3$ (right column) and with $r = 1\sigma$. The colour bar shows the range of U^{ID} in a.u. 55

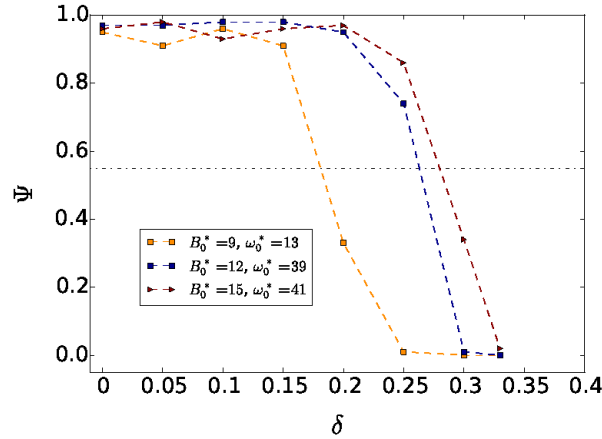


Figure 6.4.: Order parameter for layer formation as a function of the shift. The broken line marks the threshold value for layering $\Psi^{th} = 0.55$. The increase of the shift entails the break-down of layers, yet, adjusting the field parameters enables layer formation for higher shifts (compare the yellow symbols with e.g. the blue ones).

6.3. Layering of the Shifted Dipoles

To test the predictions of the numerically calculated averaged potential U^{ID} , we conduct Langevin dynamics simulations (see sections 3.2 and 3.4) and indeed find layered states for several sets of parameters being the shift δ , the field strength B_0^* and the field frequency ω_0^* .

For a quantitative characterization of the layered states, i.e. to check if layers are formed or not, we use an order parameter Ψ which was introduced in Ref. [71]. For our shifted systems, we found the threshold value of $\Psi^{th} = 0.55$ to be appropriate to detect layer formation by qualitatively evaluating simulation snapshots. Accordingly, if $\Psi \geq \Psi^{th}$, layers are formed. Moreover, the order parameter is very sensitive to the range r_c (see appendix) considered for the calculation of Ψ . It turned out that the value $r_c = 5\sigma$ is appropriate to consistently quantify the layered states.

The effect of the shift on layering Given the definition of Ψ , we systematically examine the influence of the shift on the formation of layers by successively increasing δ for fixed values of the field strength and frequency which we chose on the basis of the values found in Ref. [71] to be appropriate for layer formation in the reference system. As the results in Fig. 6.4 show, for all the sets of field parameters considered, the increase of the shift results in the break-down of layer formation. However, the value of δ beyond which layers do not form anymore depends on the field parameters and lies for e.g. $B_0^* = 9$ at

$\delta \approx 0.15$ while for the stronger fields considered, layers still form for at least $\delta = 0.25$. It is not possible to examine all the layered states for all shifts, because shifting the dipole immensely enlarges the richness of the parameter space, i.e. the number of combinations of δ , B_0^* and ω_0^* . Therefore, we limit the examination of layer formation in the shifted system exemplary to the values $\delta = 0.1$ and $\delta = 0.2$ which are as far as our experience goes relevant in order to understand the influence of the shift on pattern formation in more detail.

State diagrams Layered states are recapped in state diagrams shown in Fig. 6.5 for the reference system (solid squares) and for the shifted systems with $\delta = 0.1$ (dots) and $\delta = 0.2$ (triangles). Comparing the state diagrams, the range of layering in the shifted

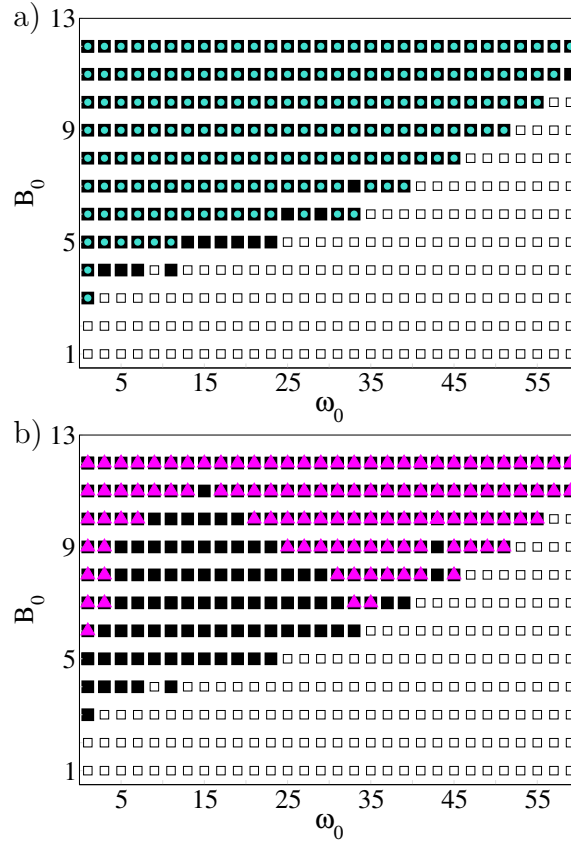


Figure 6.5.: State diagrams for $\delta = 0$ (solid squares in (a) and (b)), (a) $\delta = 0.10$ (dots) and (b) $\delta = 0.20$ (triangles). Solid symbols indicate layered states. The ensemble of all the squares shows the total range of states considered.

systems is similar to that in the reference system. While this is especially true for the lower

shift for which layering occurs for nearly the same values of B_0^* and ω_0^* (see Fig. 6.5 (a)), as well as for the high frequency ends for the higher shift, the state diagram for $\delta = 0.2$ shows a significant difference passing to lower frequencies for which no layers form at all. We will discuss this "gap" in the state diagram in more detail in section 6.6.

6.3.1. Synchronized Quantities in the Shifted System

A required condition for layer formation in the reference system is the synchronization of the dipoles with the driving field [71], i.e. for states, where the dipoles do not synchronously follow the field, layering is not observed. In the synchronized states, the assumption given in Eq. A.1, which was made for the derivation of U^{ID} (see appendix), is confirmed in practise and the particle interaction is described by U^{ID} whose specific dependency on θ yields the overall layering behaviour. The same assumption holds for the derivation of U^{ID} for the shifted case and thus, it is expected that synchronization plays the same role as in the reference system, as also indicated by the similarities of the state diagrams.

A convenient quantity to measure synchronization is the total magnetization \mathbf{M}

$$\mathbf{M}(t) = \frac{1}{N\mu} \sum_i^N \boldsymbol{\mu}_i(t), \quad (6.8)$$

whose Cartesian components $M_x(t)$, $M_y(t)$ and $M_z(t)$ are shown in Fig. 6.6 for the two shifts of interest with frequencies of the layered states, respectively. As expected, in the layered states, the total magnetization follows the field with a constant phase shift $\Delta\phi$, as known from the reference system [71], and confirms that also in the shifted system, synchronization is a crucial prerequisite in terms of layer formation as it is in the reference system. Also on the single particles level, this is confirmed, thus the distribution of the phase shift $\Delta\phi$ between the dipole vectors and the field vector attests that in the layered states, the majority of the particles organise in such a manner that their dipoles orient with a fixed angle to the external field, in the average (see Fig. 6.7). The distribution is calculated via a normalized histogram of the general form

$$n(x) = \frac{1}{N\Delta x} \left\langle \sum_{i=1}^N \Theta[(k + 0.5)\Delta x - (k - 0.5)\Delta x - x_i] \right\rangle, \quad (6.9)$$

which we use in the remainder of this work to calculate the distribution of any quantity of interest x . Then, Δx is the width of the bins into which the range of x -values is divided and Θ is the Heaviside function. Finally, k is an integer. The brackets denote a time average. Hence, for the calculation of the distribution of phase shifts, we set $x = \Delta\phi$ and $\Delta x = \pi/48$.

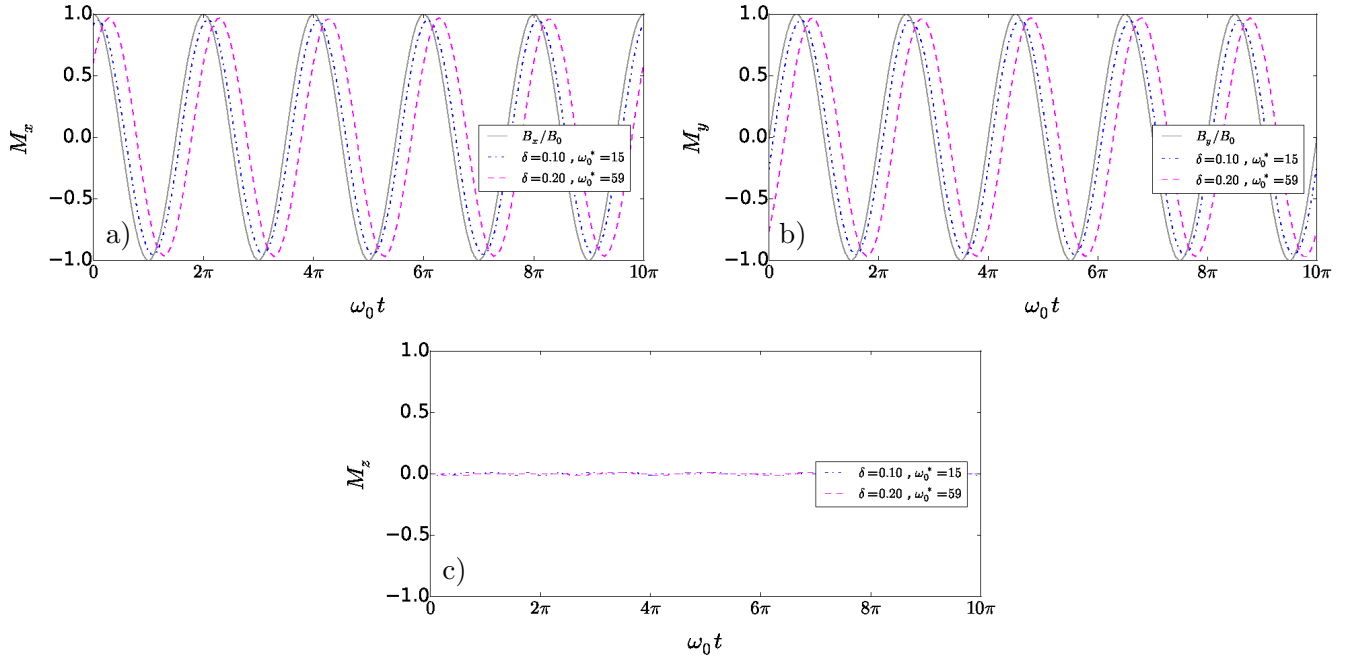


Figure 6.6.: Cartesian components of the magnetization (Eq. 6.8) as a function of time for the two shifts $\delta = 0.1$ and $\delta = 0.2$ in the layered states, respectively.

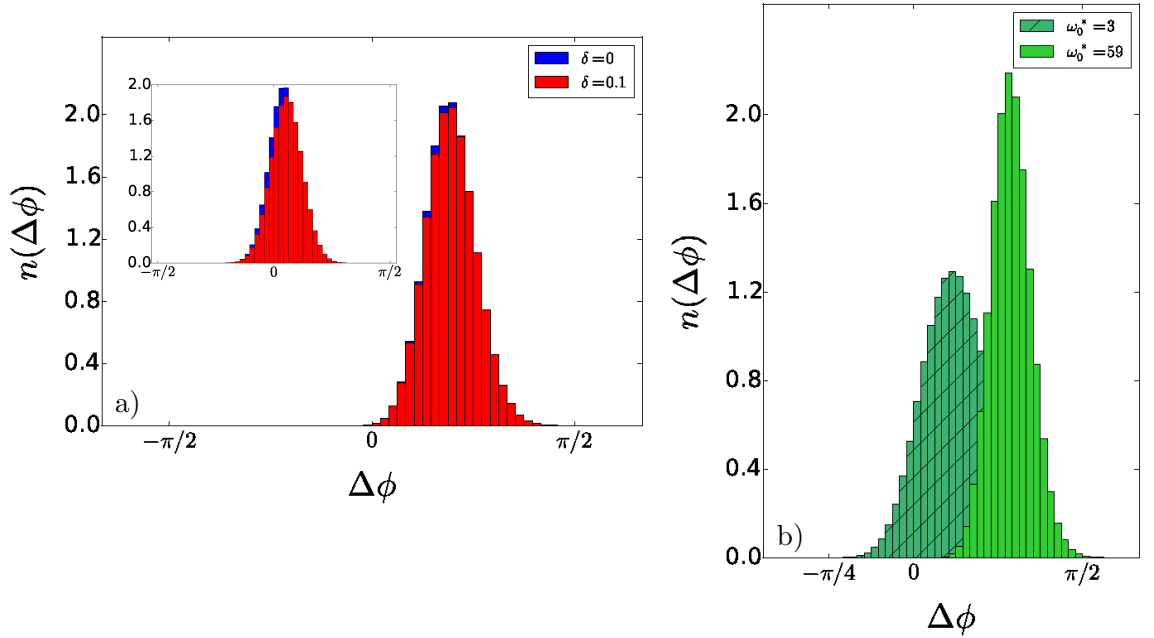


Figure 6.7.: Phase shifts with $B_0^* = 12$. (a) $\omega_0^* = 42$ and $\omega_0^* = 3$ (in the inset). (b) $\delta = 0.2$.

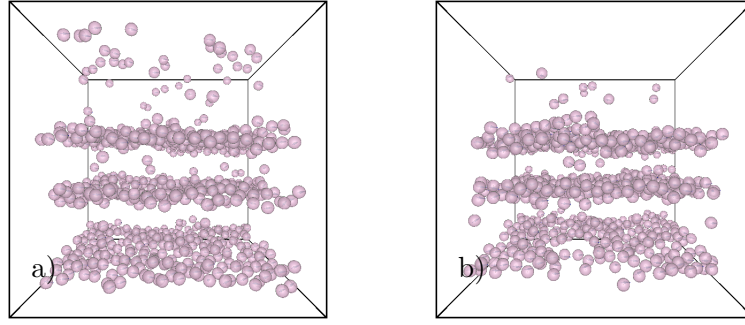


Figure 6.8.: Snapshots for (a) $\delta = 0.10$ and (b) $\delta = 0.20$ with $B_0^* = 12$, $\omega_0^* = 3$. Although the $n(\Delta\phi)$ for $\delta = 0.20$ shows a small discrepancy from the reference system, this does not disturb overall layering.

Comparing the shifted and reference systems, the results for the smaller shifts perfectly coincide with those of the reference system (Fig. 6.7 (a)). For the increased shift $\delta = 0.2$ (Fig. 6.7 (b)), the location of the peak of the distribution for $\omega_0^* = 3$ is comparable to that of the reference system but its height is decreased and accordingly, the distribution is slightly broader. Yet, this does not disturb the overall layering, as Fig. 6.8 shows, and thus suggests that the layered states might have an inherent tolerance towards an increased phase lag of single particles. The small discrepancy of $n(\Delta\phi)$ observed for $\delta = 0.2$ and $\omega_0^* = 3$ is not observed for the higher frequency.

6.3.2. Effective Single Particle Theory Applied to Shifted Dipoles

Finally, we discuss the high frequency border of the state diagrams of Fig. 6.5. For the reference system, this border was described by a single particle theory [71] which considers the rotational dynamics of a single particle immersed in a viscous medium with friction constant γ . Balancing the viscous torque on the particle with the torque due to the external field, yields an equation of motion for the phase shift $\phi = \phi_B - \phi_\mu$, where ϕ_B and ϕ_μ are the phases of the field vector and the particle w.r.t. the lab frame, respectively,

$$I\ddot{\phi} = -\gamma\dot{\phi} + \mu B_0 \sin \phi. \quad (6.10)$$

Thereby, the particle is assumed to have only rotations in the layering plane. With $\dot{\phi}_B = \omega_0$, the equation of motion without inertia for the particle w.r.t. the field vector \mathbf{B} is given by [71]

$$\frac{d\phi}{d\tau} = \frac{\omega_0}{\omega_c} - \sin \phi, \quad (6.11)$$

with $\omega_c = \mu B_0 / \gamma$ and $\tau = \omega_c t$. This equation is a so called Adler equation describing the synchronization of autonomous oscillators with an external perturbation [89, 90] and has stable solutions only for $\omega_0 < \omega_c$. It was shown [71] that the critical frequency $\omega_c(B_0)$

reproduces the high frequency border in the state diagram. In other words, if the field frequency is comparable to the critical frequency ω_c , viscous friction prevents the particles to synchronize with the field and layer formation thus breaks down.

Applying the single particle theory to the shifted dipoles, the results does not change. This is because the torques in Eq. (6.10) on the single particle are not affected by the shift of the dipole and thus the discussion proceeds in the same way as for the reference system. Practically, this is confirmed by the fact that the high frequency border in the state diagrams of the shifted systems perfectly coincide with that in the reference system (see Fig 6.5) independently of the value of δ . Moreover, this point was also confirmed in an experiment of Janus particles in a rotating magnetic field [42].

6.3.3. Conclusion

The numerical results of the time-averaged dipolar potential U^{ID} for shifted dipoles predicted that the shift does not contradict necessarily the formation of layers. Simulation results confirmed that layer formation is in principle possible in the shifted systems. Yet, it strongly depends on the amount of shift and on the field parameters. Thereby, once layer formation is present in the system, the mechanisms of it are the same as in the reference system, that is, the single particles are synchronized with the driving field, being a necessary condition. Besides, also as soon as frictional forces prevent the single particles to follow the field rotations at the high frequency border in the state diagrams, layers cannot build up anymore, which is true independently of the shift. In contrast, passing to lower frequencies, the shift highly affects the system with the higher shift $\delta = 0.2$ and results in the absence of pattern formation for certain field parameters within the layered states, while the smaller shift considered does not show any new results different from those of the reference system. Thus, the smaller shift can be regarded as a perturbation of the reference system, which obviously can be overcome by the system, whereas, only for $\delta = 0.2$, the shift has an appreciable effect on the system and thus promises new physics. Therefore, we mainly concentrate our investigations on the case $\delta = 0.2$ and occasionally show results for $\delta = 0.1$ for comparative purposes.

6.4. Behaviour of the Shift Vectors in the Layered States

In the layered state of the reference system, the dipolar rotations are phase-locked, i.e. the rotational motions of the particles are completely determined by the external field. In contrast, in the system of shifted dipoles each particle contributes with three additional degrees of freedom being the Cartesian components of its shift vector d_x , d_y and d_z . Clearly, the constraint on the dipoles due to synchronization also affects the shift vectors d_i as they are rigidly coupled and thus d_i is constrained to the plane perpendicular to the dipole vector (see Fig. 6.1 and related discussion). Yet, any arbitrary orientation of

\mathbf{d}_i in this plane still realises synchronous dipoles. Consequently, \mathbf{d}_i is undetermined in this plane. In terms of the discussion in section 6.1, this means that the components d_z^B of the shift vectors in the field-fixed system vanish, if the dipoles are perfectly synchronous and if thus the system is in a layered state. Therefore we expect that the distribution $n(d_z^B/d)$ shows a peak which is located at zero. Concerning the other two components of the shift vectors, the numerical results of the averaged dipolar potential U^{ID} yielded that some mutual orientations of *pairs of shift vectors* in the field-perpendicular plane are energetically more favourable than others, for certain sets of the appropriate parameters. However, no restrictions lay on the *single* shift vectors in this plane, in principle. In the following, we examine the distributions $n(d_z^B/d)$, $n(d_x^B/d)$ and $n(d_y^B/d)$ in order to get insight of the static and dynamic behaviour of the shift vectors in the layered states. To this end, we determine the appropriate distributions as well as explore time series of the shift vector components. Details of the considered quantities are given in the according paragraphs.

6.4.1. Static Behaviour

Static Field As a starting point we first check the distributions of the shift vector components, gained by Eq. (6.9) with $x = d_\alpha^B/d$ (with $\alpha = x, y, z$) and $\Delta x = 0.05$, in the static field, i.e. with $\omega_0^* = 0$. This situation represents perfectly aligned dipoles (for appropriately chosen field strengths) which allows to confirm the expectations for $n(d_z^B/d)$, and which gives a first impression of the orientation of the shift vectors in the plane to which they are constrained. The results for $\delta = 0.2$ are shown in Fig. 6.9 for exemplary field strengths. As expected, $n(d_z^B/d)$ shows a peak located at zero which increases with increasing field strength (see Fig. 6.9 (a)). Furthermore, in the field-perpendicular plane, the shift vectors rather prefer pointing along the x^B - and y^B -axes of the field-fixed coordinate system with equal probability, while orientations in between are not unlikely. Noticeably, the distributions are perfectly symmetric q.r.t zero such that half of the particles align their shift vectors e.g. along with the positive x^B -axis and half with the negative one. The results obtained for the smaller shift $\delta = 0.1$ (not shown) are the same as for $\delta = 0.2$ indicating that they are not specific for a certain value of the shift.

Dynamic Field In a next step, we pass to the dynamic system ($\omega_0^* > 0$) and investigate the effects of field rotations on the distributions. Figure 6.10 depicts the results for $\delta = 0.2$ with three sets of field parameters chosen across the frequency range considered in the state diagram (Fig. 6.5 (b)).

To start with, the distributions $n(d_z^B/d)$ are qualitatively not influenced if we let the field rotate, whereas quantitatively, they are remarkably broadened. The reason for that lies in the phase lag of the dipoles w.r.t. the driving field, which is why the dipoles, even still synchronized, do not point to the same direction as the field vector. In this case, the

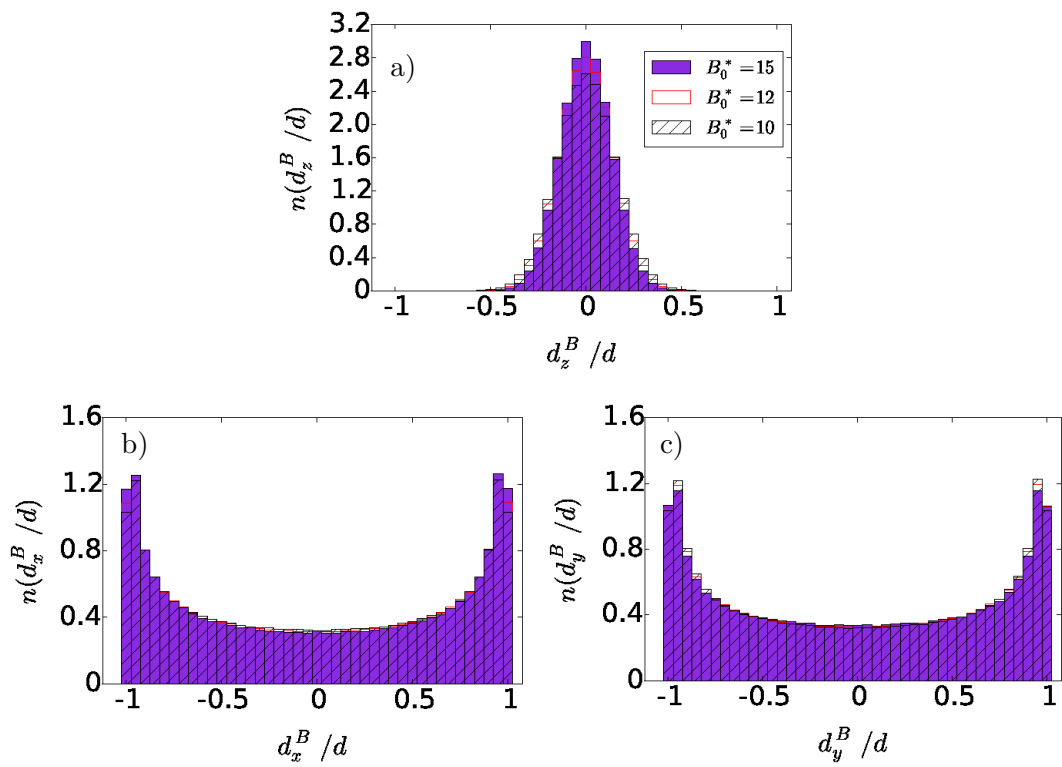


Figure 6.9.: Distributions of the components of the shift vectors for $\delta = 0.2$ in a static field ($\omega_0^* = 0$). The symbols in (b) and (c) are the same as shown in the legend in (a).

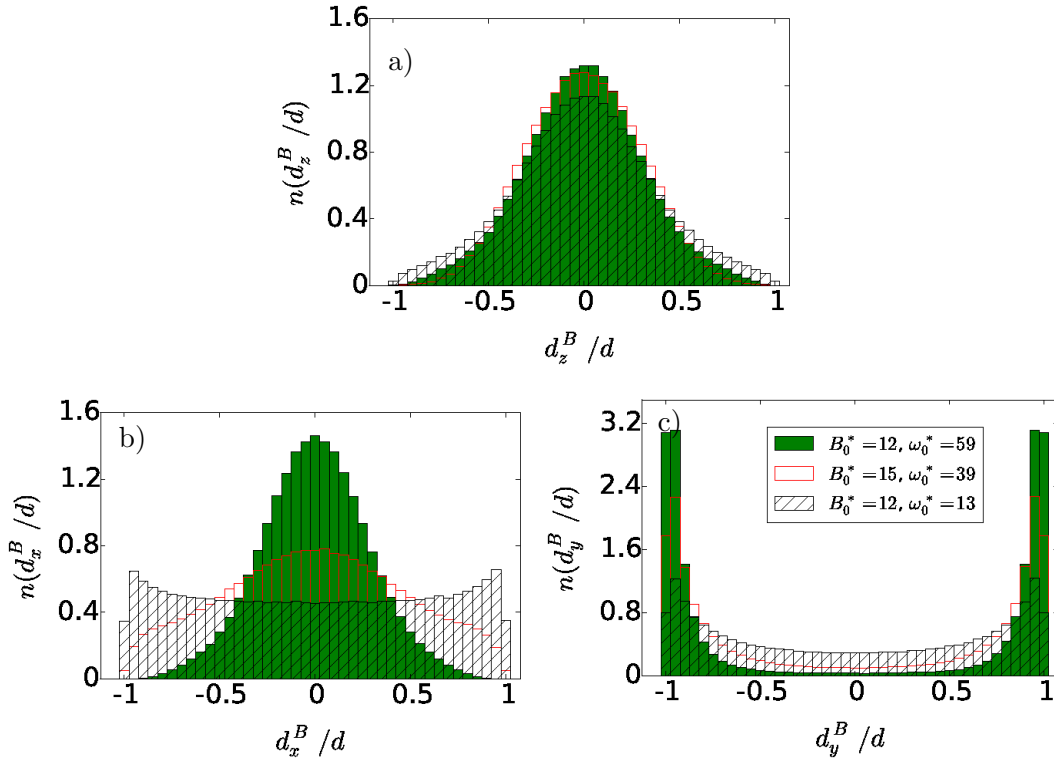


Figure 6.10.: Distributions of the components of the shift vectors for $\delta = 0.2$ in dynamic fields. The symbols in (a) and (b) are the same as shown in the legend in (c).

shift vectors may lie out of the field-perpendicular plane without violating synchronization, because indeed, the shift vector is constrained to the plane perpendicular to the dipole vector but not necessarily to the field-perpendicular plane. Due to the phase shift, these two planes are rotated w.r.t. to each other, which is why non vanishing values of d_z^B , shown in Fig. 6.10 (a), are not contradictory to all the assumptions and arguments made so far. This also explains why stronger fields, which align the dipoles more tightly and thus reduce the phase shifts, sharpens the distribution. Interesting however is that also higher frequencies sharpens the distribution. This point will become more obvious in section 6.4.2 to which we postpone its discussion.

Strikingly different is the effect of the field rotations on the remaining two components. More precisely, $n(d_x^B/d)$ (Fig. 6.10 (b)) qualitatively coincides with the static case for the lowest frequency considered, although the peaks at -1 and 1 are less distinct, which is again a consequence of the phase shift, as just discussed. The same behaviour is found for the distribution $n(d_y^B/d)$ (Fig. 6.10 (c)). However, upon increasing the frequency, $n(d_x^B/d)$ redistributes towards zero while at the same time, the existing peaks in $n(d_y^B/d)$ at -1 and 1 significantly rise. In other words, the increasing frequency of the field rotation

induces the shift vectors to point exceptionally along the positive and negative z -axis of the laboratory frame. Especially if the frequency takes values near the high frequency border in the state diagram, orientations along the d_x^B -axis are completely given up. We note that this crossover of the shift vectors is mainly a result of the increase of the frequency than of the field strength. We also state that this crossover only appears for the higher shift and is not observed for $\delta = 0.1$. Noticeably, all distributions are perfectly symmetric around zero, as in the static case, meaning that each occurring orientation has a mirror inverted counterpart. This is indicative for a behaviour of the shift vectors governed by mutual and pairwise arising orientations, as dictated by the averaged potential U^{ID} . We will discuss this point in detail in section 6.5.

6.4.2. Dynamic Behaviour

Time Evolution of the Shift Vectors The previous discussion concerning the distributions of the shift vector components in the *field-fixed coordinate system* gives a very clear picture of the preferred *static* organization of the shift vectors in the layered states. To complete the picture, we study the *dynamical* behaviour of the shift vectors. Yet, its components has to be evaluated in the *laboratory frame*, in order to gain insight about their time evolution. In this frame, one expects the shift vectors to perform an oscillating motion, stemming from the synchronized rotations of the dipole vectors (see e.g. Fig. 6.6).

The averaged and normalized components

$$\frac{\langle d_\alpha(t) \rangle}{d} \equiv \langle \hat{d}_\alpha \rangle = \frac{1}{N} \left\langle \sum_{i=1}^N \frac{d_{i,\alpha}(t)}{d} \right\rangle \quad (6.12)$$

cannot yield information about the time dependence of the shift vectors because, as discussed above (see Fig. 6.10), the shift vectors are distributed symmetrically w.r.t. the laboratory frame's x - y -plane and its z -axis, which results in time series of \hat{d}_α fluctuating around zero. This is why we map the orientations of all the shift vectors to the first octant of the coordinate system. More precisely, we consider the absolute values of the components instead, i.e. $\langle |\hat{d}_\alpha| \rangle = \frac{1}{N} \left\langle \sum_{i=1}^N \frac{|d_{i,\alpha}(t)|}{d} \right\rangle$, and thus define an averaged mapped shift vector $\langle \hat{\mathbf{d}} \rangle = (\langle |\hat{d}_x| \rangle, \langle |\hat{d}_y| \rangle, \langle |\hat{d}_z| \rangle)$. The results are shown in Fig. 6.11 together with the external field. In order to highlight the frequency and shift dependent behaviour of the shift vectors, we choose a low ($\omega_0^* = 3$) and a high ($\omega_0^* = 41$ or $\omega_0^* = 59$) frequency for the two shifts $\delta = 0.1$ and $\delta = 0.2$, respectively.

Not surprising are the oscillations of the quantities $\langle |\hat{d}_x| \rangle$ and $\langle |\hat{d}_y| \rangle$ stating that the average shift vector perpendicularly follows the external field such that $\langle |\hat{d}_x| \rangle$ is correlated with $|B_y|$ and $\langle |\hat{d}_y| \rangle$ with $|B_x|$ (see Figs. 6.11 (a) and (b)). In contrast, the average z -component of

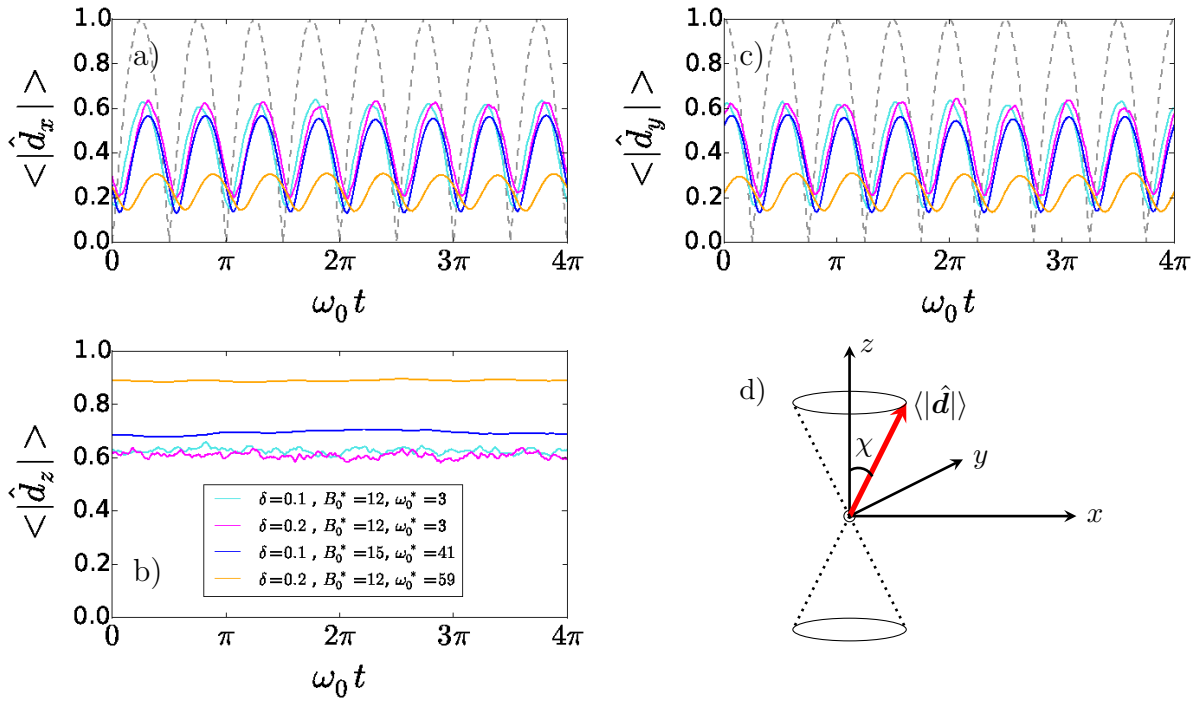


Figure 6.11.: Time evolution of the absolute values of the averaged and normalized shift vector components in the laboratory frame. The dotted lines show the time evolutions of $|B_y|/B_0^*$ (a) and $|B_x|/B_0^*$ (b), respectively. The colours are as indicated in the legend in (b). (d) Sketch of the double cone with $\chi = \chi(\delta, \omega_0^*)$, on which the shift vectors lie.

the mapped shift vectors, $\langle |\hat{d}_z| \rangle$, fluctuates about a constant value (Fig. 6.11 (c)). Consequently, during the course of the field rotation, the average shift vector $\langle \hat{d} \rangle$ describes a segment of a cone which takes course around the laboratories z -axis and whose vertex is located at the origin (Fig. 6.11 (d)). While qualitatively, this is true for all the parameters considered in Fig. 6.11, quantitatively, the shift and the field frequency specify the cone angle $\chi = \chi(\delta, \omega_0^*)$: For (i) the smaller frequency and both shifts, as well as for the higher frequency and the smaller shift, χ is rather large. On the other hand, it considerably reduces in the high frequency regime for $\delta = 0.2$ (ii). Accordingly, the amplitudes of the oscillations in Figs. 6.11 (a) and (b) decrease and at the same time the level of $\langle |\hat{d}_z| \rangle$ increases, passing from case (i) to (ii).

Autocorrelation Function The quantity $\langle \hat{d} \rangle$ is a *system averaged* quantity which, in the layered states, is restricted to the segment of a characteristic cone being specified by appropriate parameters (δ and ω_0^*). On the other hand, as discussed above, the distributions of the components of the *single* shift vectors show point-symmetry w.r.t. the origin. It thus

follows that the averaged and mapped shift vector $\langle \hat{d} \rangle$ also has a point symmetry w.r.t. the origin and the single shift vectors lie on a double cone with $\chi = \chi(\delta, \omega_0^*)$ (see Fig. 6.11(d)). In other words, this means that a single shift vector in principle can be oriented in any of the octants of the coordinate system as long as its orientation is conformal with the double cone $\chi = \chi(\delta, \omega_0^*)$. However, the results shown in Fig. 6.11 cannot resolve whether a single shift vector evolves continuously on the cone during the course of the field rotations, or if it rather flips randomly from one octant to another, i.e. permanently changes its position on the cone. Of course, this would not change the results of $\langle |\hat{d}_\alpha| \rangle$. In order to unravel the behaviour of the single particles' shift vectors, we compute the autocorrelation functions $C_{d_x d_x}$, $C_{d_y d_y}$ and $C_{d_z d_z}$ of the normalized shift vector components via the general expression[62, 91]

$$C_{AA}(\tau) = \langle A(t+\tau) \cdot A(t) \rangle = \frac{1}{N} \langle \sum_i A_i(t+\tau) \cdot A_i(t) \rangle, \quad (6.13)$$

with $A_i = d_{i,\alpha}/d$ and show the results in Fig. 6.12.

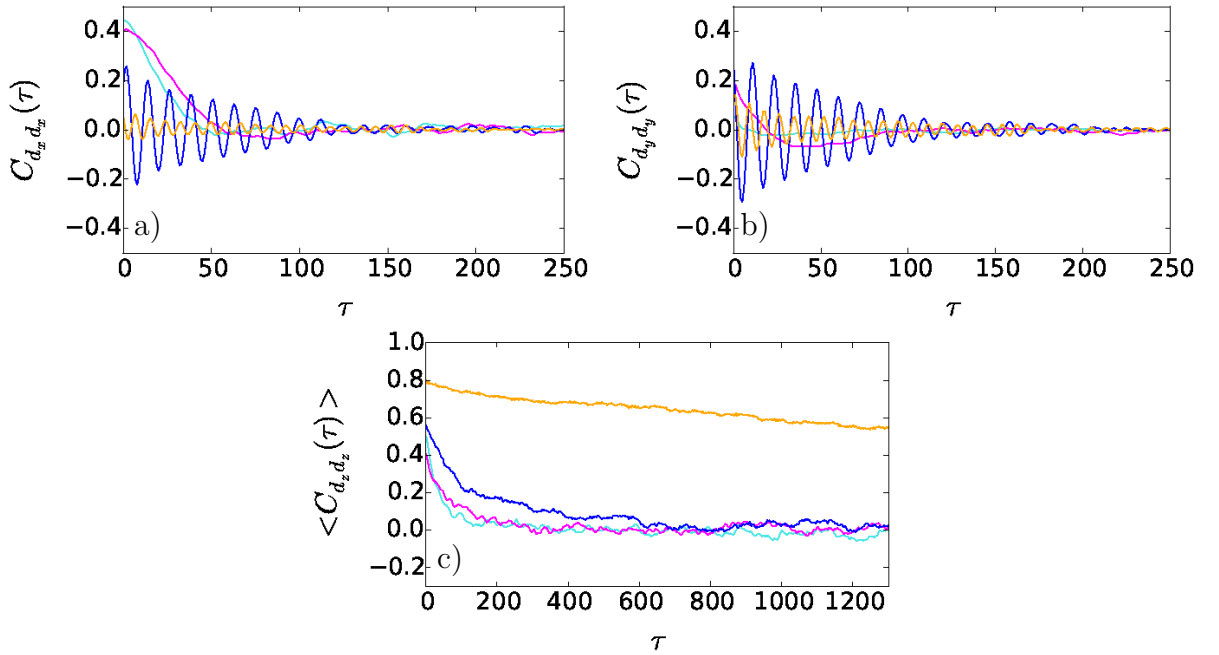


Figure 6.12.: Autocorrelation functions of the shift vectors (see Eq. 6.13) with $\tau = 5\Delta t$. The colours are the same as in Fig. 6.11.

The autocorrelations $C_{d_x d_x}$ and $C_{d_y d_y}$ show major qualitative differences for the low and the high frequencies considered. In the previous case, the correlations monotonically decay after about 100τ at the latest. Within this time span, the field with frequency $\omega_0^* = 3$ fulfils about half a period ($t^* = 100\tau = 1.25 \approx 0.60T^*$, T^* being the period). In the latter

case however, the correlations oscillate with frequency $\omega^* = \omega^*(\delta, \omega_0^*)$ about zero and significantly decrease after about $t^* = 250\tau$. This time span corresponds to $t^* \approx 20.39T^*$ (for $\omega_0^* = 41$) or $t^* \approx 29.34T^*$ (for $\omega_0^* = 59$), respectively. More specifically, we roughly estimate from the Figs. 6.12 (a) and (b) the frequencies of the oscillations as $\omega^*(0.1, 41) \approx 40.21$ and $\omega^*(0.2, 59) \approx 58.64$, denoting that the correlations essentially oscillate with the according field frequency. In contrast, the correlations of the z -components (Fig. 6.12 (c)) decay monotonically for all frequencies. Apart from that, the z -components are longer correlated than the x - and y -components. Thereby, the correlations for $\delta = 0.2$ and $\omega_0^* = 59$ (orange line in Fig. 6.12 (c)) are considerably increased compared to the other cases, such that even after $t^* = 1300\tau \approx 152.59T^*$ periods, $C_{d_z d_z}$ did not reduce significantly.

In conclusion, the results reveal that for the low frequency, the shift vectors perform random flips on the characteristic double cone, whereby flips involving a change of d_z happen less frequently than those which change d_x and d_y . By contrast, for high frequencies, the shift vectors are driven on the characteristic cone along which it rotates with the frequency of the driving field. The stronger correlations of d_z indicate that the shift vectors rather stay on one of the upper or lower halves of the double cone, but seldom changes happen. Thereby, the relation $\chi(0.1, 41) > \chi(0.2, 59)$ holds, being signified by the smaller amplitudes for the latter case (cf. the blue and orange lines in Figs. 6.12 (a) and (b)). Specifically for $\delta = 0.2$ and $\omega_0^* = 59$, the shift vectors are apparently locked along the z -axis.

6.5. Double Layer Formation

The analysis of the shift vectors yielded striking qualitative (see Fig. 6.10 (b)) and quantitative (see Fig. 6.10 (c)) differences in the shift vector distributions for $\delta = 0.2$ upon the increase of the field frequency. At the same time, also the dynamic behaviour of the shift vectors for this shift at high frequencies quantitatively (see Fig. 6.11) and/or qualitatively (see Fig. 6.12) sets itself apart from the other cases, namely from the behaviour at lower frequencies for both shifts as well as from the behaviour at higher frequencies for the lower shift $\delta = 0.1$. This indicates that also the forming layers in this case might be different from all other cases. Figure 6.13 shows snapshots of simulations with $\delta = 0.2$ for three frequencies being $\omega_0^* = 31, 39$ and 59 with different field strengths (see the caption for details). Clearly, passing to very high frequencies ($\omega_0^* = 59$), the loose and unstructured layers observed for the smaller frequencies develop towards double layers consisting of a lower and an upper sub layer (see 6.13 (c)). The regime of double layers is characterized by an organization of the particles within a seemingly rigid assembly which apparently holds higher translational order, compared to smaller frequencies. We emphasize that the transition from single to double layers happen solely by the increase of the frequency, i.e. if ω_0^* is not sufficiently high, the only increase of the field strength does not provoke the formation of double layers.

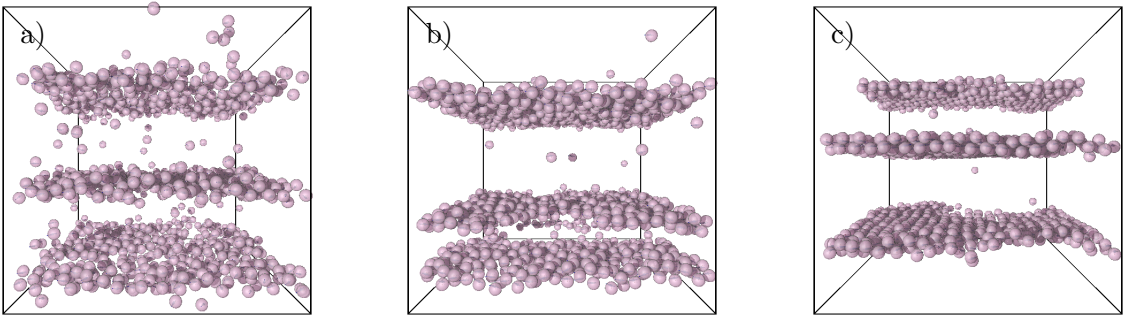


Figure 6.13.: Snapshots with $\delta = 0.20$. (a) $B_0^* = 10$, $\omega_0^* = 31$, (b) $B_0^* = 15$, $\omega_0^* = 39$, (c) $B_0^* = 12$, $\omega_0^* = 59$. The increase of the frequency provokes a transition from single to double layers for field strengths $B_0^* > 10$.

Onset of Double Layers In order to study the onset of the double layers, we introduce the order parameter Ψ_{DL} as follows: A quadratic slice of thickness $h = 1\sigma$ which is parallel to the x - y -plane is virtually drawn around particle i such that the bottom of the slice is located at $-\sigma/2$ and the top at $+\sigma/2$ w.r.t. the centre of mass of particle i . Then, we

define

$$\Psi_{DL} = 1/N \langle \sum_i^N n_i \rangle, \quad (6.14)$$

where $n_i = +1$ if the z -component of the distance vector between particle i and at least one of its nearest neighbours, \mathbf{dr}_z , fulfils $|\mathbf{dr}_z| \geq 0.5\sigma$. By definition, particles with a distance less equal 1.3σ are nearest neighbours of particle i . Further, $n_i = 0$ if $|\mathbf{dr}_z| < 0.5\sigma$, and if particle i does not have any nearest neighbour, $n_i = -1$ holds. In other words, Ψ_{DL} measures whether two nearest neighbouring particles are arranged in the same slice or in two neighbouring slices. Thus, $\Psi_{DL} = 1$ holds if all particles are arranged in double layers while $\Psi_{DL} = 0$ signifies perfect single layers. Note that these statements are valid in the overall layered states which are jointed in the state diagram in Fig. 6.5 (b). For unlayered states, Ψ_{DL} can also take in principle any positive value, or it can have negative values, essentially meaning that the particles are isolated from each other. In either case, no pattern is formed at all. With these definitions, Ψ_{DL} operates as a fine tuning parameter of the layered states which separates double from single layers. Specifically, by observing snapshots, we determined the threshold $\Psi_{DL} > 0.85$ to be appropriate to describe double layers. In practice, the order parameter Ψ_{DL} will of course deviate from these values due to e.g. fluctuations or the finite sample size in the simulations such that we test its behaviour for the reference system ($\delta = 0$) and take these results as a guideline to classify the results of the shifted system with $\delta = 0.2$ for which double layers are observed. In Fig. 6.14, we plot Ψ_{DL} as a function of ω_0^* for the reference system with $B_0^* = 12$ as well as for the shifted system with several field strengths in the range $B_0^* = 9 - 12$. Thereby, we consider the frequency range with $\omega_0^* > \approx 25$ as double layers are observed only for very high frequencies near the border to unlayered states, which is why low frequencies are irrelevant here. First of all, the results for Ψ_{DL} in the reference system in which conventional layers are observed, are comparable for all frequencies considered and lie between 0.2 and 0.3, which we thus fix as being the characteristic value for conventional layers. In terms of the shifted system, what all of the plots have in common is a monotonic increase of Ψ_{DL} which continuously reaches its maximum value right at the border to the unlayered states, respectively. Obviously, upon increasing the frequency, the particles more and more veer away from building conventional layers, characterized by values for Ψ_{DL} comparable to that of the reference system, and for sufficiently high frequency, they organise in double layers. However, only for $B_0^* > 10$, Ψ_{DL} exceeds the limit value for double layers and indeed, we did not observe double layer formation for lower field strengths. In conclusion, the crossover from conventional to double layers upon the increase of the frequency and for appropriate field strengths comes about continuously.

Structure of the Double Layers The crossover from conventional to double layers imply that this transition is accompanied by a structural change of the occurring layers.

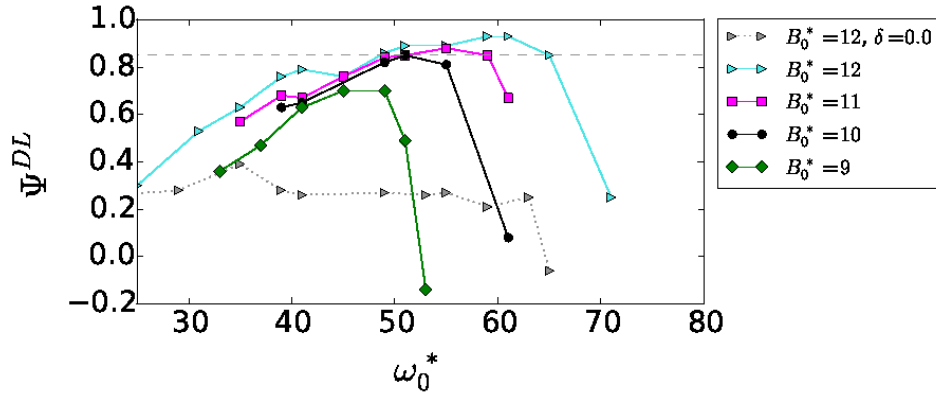


Figure 6.14.: Order parameter Ψ_{DL} as a function of ω_0^* for $\delta = 0.2$ (unless otherwise specified). The broken line marks the threshold value $\Psi_{DL} = 0.85$.

To shed light on this point, we calculate the in-plane (i.e. parallel to the x - y -plane) pair correlation function $g_{\parallel}(r)$ by

$$g_{\parallel}(r) = \left\langle \frac{\sum_i \sum_{j \neq i} \delta(h - |\mathbf{r}_{ij,z}|) \delta(r - |\mathbf{r}_{ij}|)}{N\rho\Delta V} \right\rangle, \quad (6.15)$$

with $\mathbf{r}_{ij,z}$ being the z -component of the distance vector \mathbf{r}_{ij} of particles i and j and ΔV being the volume of a cylindrical shell of height h around particle i . Choosing $h = 0.5$ then gives the pair correlation function of particles in the same sub layer. As the normalization of $g_{\parallel}(r)$ is done w.r.t. a section (i.e. the cylindrical shell of height h) of the three-dimensional system, the long range limit of $g_{\parallel}(r)$ does not necessarily approach unity.

Indeed, as the results for $\delta = 0.2$, $B_0^* = 12$ and several frequencies show (Fig. 6.15 (a)) $g_{\parallel}(r)$ is long-ranged for double layers ($\omega_0^* = 55$ and $\omega_0^* = 59$) and otherwise, i.e. for the lower frequencies, it shows typical correlations known from the liquid state. If the field strength is increased, the shape of $g_{\parallel}(r)$ basically does not change but becomes more and more pronounced, as can be seen in Fig. 6.15 (b), indicating that stronger fields sharpens the occurring structures. In particular, the shape of $g_{\parallel}(r)$ highly resembles the radial distribution function of a colloidal Yukawa-Wigner bilayer system examined in Ref. [92] (see Fig. 5(a) there) which describes staggered square lattices. A staggered organization of the two sub layers of a double layer is also apparent in our system and the similarity of the pair correlation functions of the two systems indicate that the sub layers in our system also might have square geometry. However, a full characterization of the geometries in the double layers goes beyond the scope of this work and we will refer to that point in the outlook. Moreover, in the long range limit, $g_{\parallel}(r)$ rises for increasing frequency as well as for increasing field strength, reflecting a more and more denser organisation of the particles within the layers. All in all, if the frequency is increased, the layers pass from a liquid state, in which the particles are organized without any specific structure to a crystal-like state with

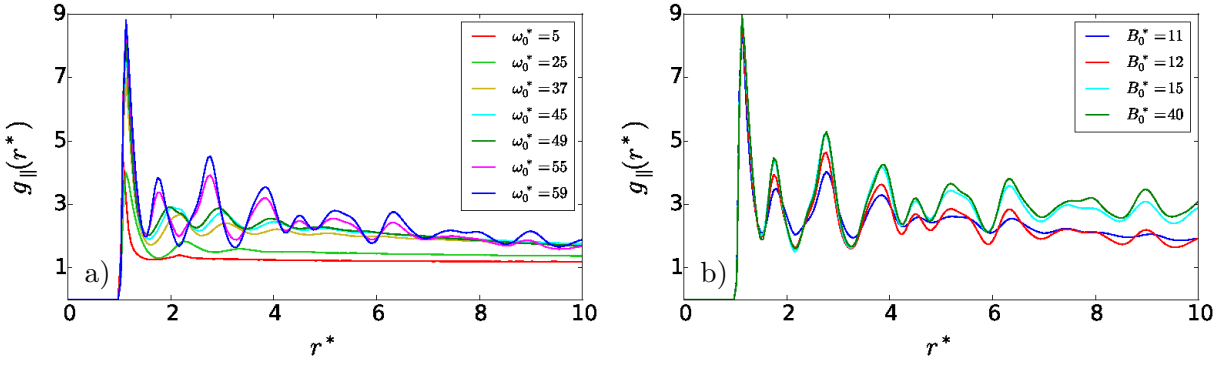


Figure 6.15.: In-plane pair correlation function for the shifted system ($\delta = 0.2$) with (a) $B_0^* = 12$ and several frequencies or with (b) $\omega_0^* = 59$ (double layered state) and several field strengths.

long-ranged translational order, even though the correlations decrease in the long distance limit.

Mean Squared Displacement The study of the pair correlation function $g_{\parallel}(r)$ in the previous paragraph suggested that the occurring double layers hold a solid-like structure in which the particles are densely organized. In order to survey whether the particles are caught in their assemblies within the double layered states, we calculate the mean squared displacement

$$\langle |\mathbf{r}(t) - \mathbf{r}(t + t')|^2 \rangle = 1/N \langle \sum_i |\mathbf{r}_i(t) - \mathbf{r}_i(t + t')|^2 \rangle \quad (6.16)$$

for several field frequencies with $B_0^* = 12$. The results are depicted in Fig. 6.16. Passing from very low to very high frequencies, the translational dynamics of the particles is decelerated up to more than one order of magnitude in the diffusive regime (see Fig. 6.16 (a)). This is consistent with the observation of a more and more concentrated organization of the particles in the layers, if the frequency is increased, involving that the particles impede each other. In addition, the mean squared displacement for $\omega_0^* = 59$ comprises a sub diffusive regime between the ballistic and diffusive regimes, namely in the range $t^* \approx 0.3 - 1$. Evidently, on the sub diffusive time scale, the particles are trapped for a while yet, as the diffusive regime is entered they are not caught, thus the double layers are not in a solid state. Insight about the origin of the trap can be gained by decomposing the mean squared displacement in its Cartesian components, depicted in Fig. 6.16 (b) for $\omega_0^* \geq 3$ and $\omega_0^* \geq 59$ and revealing that the particles are trapped in the z -direction, while the translational dynamics in the x - and y - directions are equal (yet slowed for increasing frequencies) for the whole range of frequencies of the layered states. The former can be understood by the overall layering of the particles which is the energetically favoured

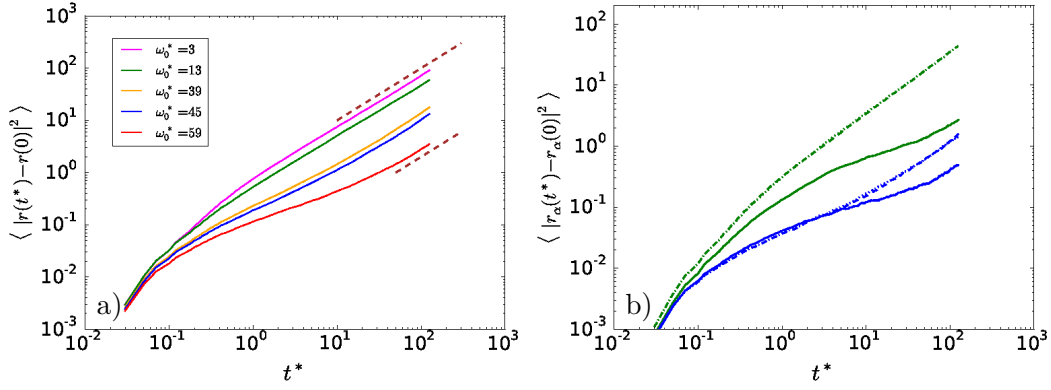


Figure 6.16.: (a) Mean squared displacement for $\delta = 0.2$ and $B_0^* = 12$. The broken lines have slope 1. (b) Its x -, y - and z -components: $\alpha = x$ (dotted line), $\alpha = y$ (broken line), $\alpha = z$ (straight line) for the frequencies $\omega_0^* = 3$ (green) and $\omega_0^* = 59$ (blue).

organization in such system, as shown and discussed earlier (see section 6.3 and Ref. [71]) and thus, once a particle has arranged in a certain layer, it stays in this layer for a while before it passes to another one. Thereby, the higher the frequency, the longer the particles are caught in their layers. Yet, within the layers, the particles freely diffuse in the x - y -plane. We note that the described effect is especially dominant in the double layered states and becomes even pronounced with increasing field strengths (not shown).

The sub diffusive regime is also observed for the moderate frequencies ($\omega_0^* \geq 39$ and $\omega_0^* \geq 45$) considered in Fig. 6.16 (a), but is less distinct, while for the lowest frequencies, the diffusive regime begins subsequently after the ballistic one.

Pair Dynamics in the Layered States So far, we examined the characteristics of the occurring layered states by considering quantities of single particles. Yet, in order to make a point about the assembly of the particles within the layered states, it is necessary to examine the relation of the particles with each other. Thus, we pass to the two-particle level, i.e. we consider dynamic quantities of pairs. Specifically, we calculate two quantities: First, we count the number of pairs as a function of time, averaged over several measurements. Thereby, as soon as all pairs once identified have dissolved, i.e. the distance of the two particles within the pair exceeds 1.3σ , a new measurement is started. Next, we calculate the autocorrelation function $C_{\hat{r}_{ij}\hat{r}_{ij}}(t^*)$ (see Eq. (6.13)) of the normalized distance vector of the identified pairs with the same procedure. We note that our analysis considers any of the nearest neighbours of a certain particle, i.e. the identified pairs can be jointed. In other words, the identified pairs themselves might be organized in a higher structure as a particle in an identified pair can at the same time form a pair with another particle. Yet, for our purpose of understanding how strong the particles are bound to each

other, the analysis on the two-particle level is sufficient.

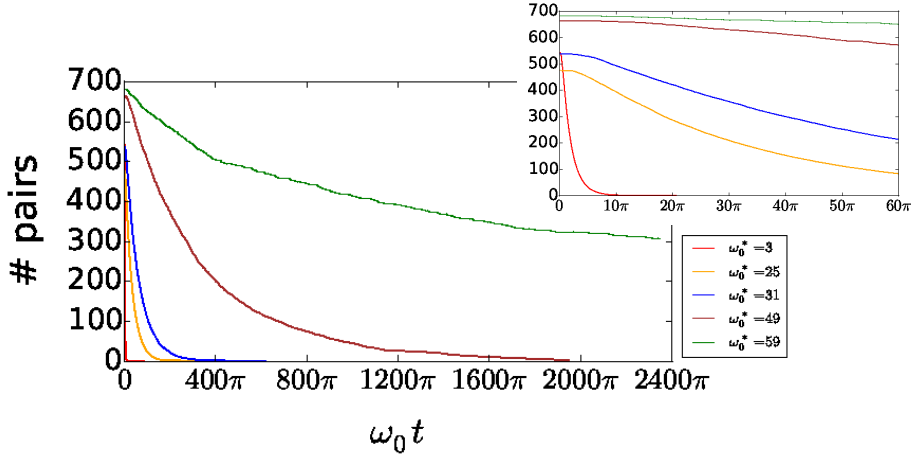


Figure 6.17.: Average number of pairs as a function of time for $B_0^* = 12$ and several frequencies. The inset shows the magnification for initial times.

In Fig. 6.17 we show the average number of pairs as a function of time for $B_0^* = 12$ and several frequencies. For all frequencies considered, this number rapidly decreases with time, however, with increasing frequency, the decay significantly slows down. Consequently, in the quasi static regime, i.e. very small frequency (e.g. $\omega_0^* = 3$), the particles rapidly reorganize within the layers during the course of field rotations, compared to higher (and increasing) frequencies. Thus, for $\omega_0^* = 3$, the particles completely reorganize every about 5 rotational periods of the field, whereas for the double layered state ($\omega_0^* = 59$), about half of the initially identified pairs persist even after more than 1000 periods. As a result, the increase of the frequency leads to more tightly bounds of the particles which involves the observed structural transition, passing to higher frequencies. Also the relative organization of the particles in a pair are highly correlated at high frequencies. Thus, the results of $C_{\hat{r}_{ij}\hat{r}_{ij}}(t^*)$ (see Fig. 6.18) for the same parameters as in Fig. 6.17 reveal an increasingly slower decay of the correlations with increasing frequency for $\omega_0^* \leq 49$. At the same time, for $\omega_0^* = 59$ (double layered state), $C_{\hat{r}_{ij}\hat{r}_{ij}}(t^*)$ shows a qualitative difference. It does not decay but take a constant value near one, meaning that the pair vector does not significantly deviate from its position at a certain time origin. However, the mean squared displacement (see Fig. 6.16) has yielded that the particles diffuse in the layered. Hence, in the double layered states, the particles form pairs, i.e. dumbbells, which are the new units of the system and which diffuses in the layering plane but does not change the orientation of their long axes.

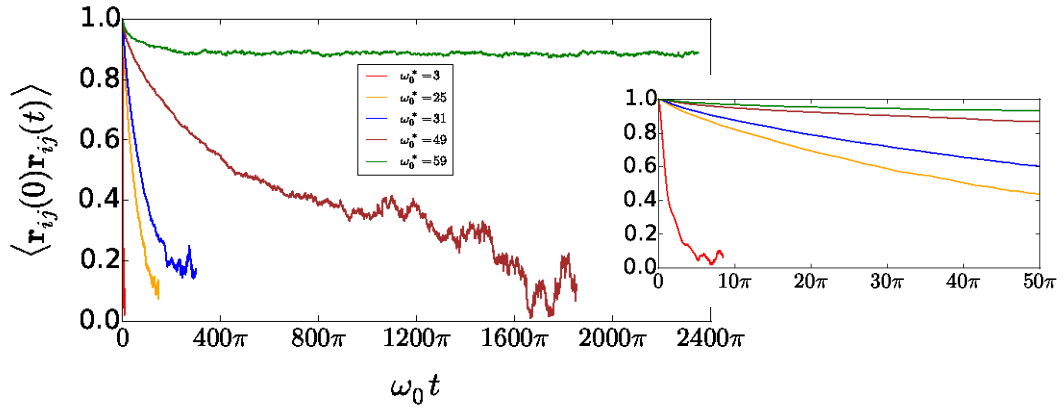


Figure 6.18.: Autocorrelation function $C_{\hat{r}_{ij}\hat{r}_{ij}}(t^*)$ for the same parameters as in Fig. 6.17. The inset shows the magnification for initial times.

6.5.1. Explanation via U^{ID}

In order to understand the formation of double layers, we turn back to the analysis of U^{ID} which was derived in section 6.1. The derivation yielded that U^{ID} of a pair of shifted dipoles depends on the parameters ϵ , Φ_i , Φ_j and θ describing the shift, the relative orientations of the shift vectors in the perpendicular-plane and the angle between the centre-to-centre distance vector and the z -axis, i.e. the polar angle.

In the following, we calculate the distributions of these quantities in the simulations for $\epsilon = \delta = 0.2$ (see sections 2.1, 6.1 and 6.2). In more detail, we count the number of close contact pairs (i.e. two particles in a distance $\leq 1.3\sigma$), $n(\Phi_i, \Phi_j)$, comprising the combination Φ_i, Φ_j

$$h(\Phi_i, \Phi_j) = \frac{\langle n(\Phi_i, \Phi_j) \rangle}{N_{pairs}}, \quad (6.17)$$

normalized by $N_{pairs} = \sum_{i,j>i} n(\Phi_i, \Phi_j)$ being the total number of close contact pairs. In the same way, we calculate the normalized histogram $n(\theta)$ (see Eq. (6.9)) of the polar angle θ of close contact pairs.

We start the discussion with the distribution of the polar angle θ , shown in Fig. 6.19. For frequencies where double layers are not yet observed, i.e. low frequencies (e.g. $\omega_0^* = 15$ in the plot), $n(\theta)$ comprises a single maximum at $\theta = 80^\circ$, indicating side by side arrangements of the particles within the layering plane (lying configuration). This single maximum splits up towards two distinctly preferred values being $\theta = 50^\circ$ and $\theta \approx 90^\circ$, if the frequency is increased, such that the particles within the pairs now additionally organise on top of each other (standing configuration), confirming the occurrence of the double layered structures. The increase of the field strength sharpens the two peaks in the distribution but does not shift their locations from the said values. Consequently, stronger fields generate

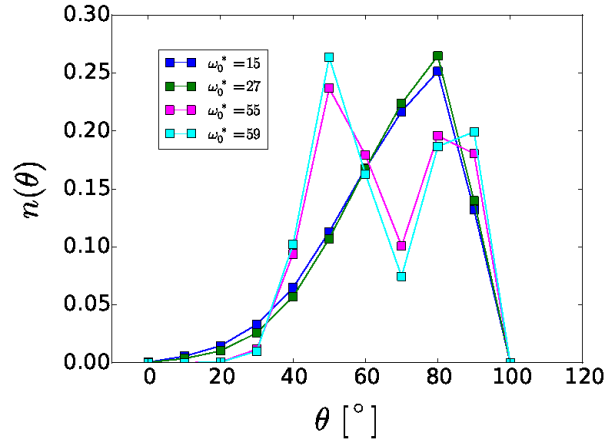


Figure 6.19.: Histogram of the polar angle θ for $B_0^* = 11$ (blue), $B_0^* = 10$ (green), $B_0^* = 15$ (magenta) and $B_0^* = 12$ (cyan). The two peaks for the high frequencies reflect the formation of double layers. The bin size is $\Delta\theta = 10^\circ$.

more distinct double layers, as was also indicated by Fig. 6.15 (b). This is of course not surprising because stronger fields dominate over the dipolar orientations to a higher degree than lower ones.

Together with the double peaks in the distribution of θ in the double layered states, the distribution of the shift vectors of these close contact pairs (see Fig. 6.20) exhibits sharp peaks at the two points $\Phi_i = \Phi_j = 90^\circ$ and $\Phi_i = 90^\circ, \Phi_j = 270^\circ$ for double layered states (e.g. $\omega_0^* = 59$ in 6.20 (b)) and progressively gets smeared out if the frequency decreases (Fig. 6.20 (a)). This behaviour of $h(\Phi_i, \Phi_j)$ is observed for all field strengths, passing from double layered states towards lower frequencies.

Comparing the simulation results with the numerical results of U^{ID} (see Fig. 6.3) for those preferred values for θ found in the simulations, yields that the configurations for Φ_i and Φ_j found in the double layered states perfectly match those ones which optimize U^{ID} . Hence, in the lying configuration, parallel ($\Phi_i = \Phi_j = 90^\circ$) shift vectors, while in the standing configuration, antiparallel ($\Phi_i = 90^\circ, \Phi_j = 270^\circ$) directed ones are energetically highly favoured. Remarkably, for these configurations, the time-dependent term in the dipolar distance r' , derived in Eq. (6.5), vanishes. Specifically, for the standing configuration, r' becomes as minimum as possible. More precisely, if θ becomes too small (which would further minimize r'), the dipolar potential in Eq. (6.6) becomes repulsive. In turn, the lying configuration results in the relation $r' = r$ such that U^{ID} acts as in the non-shifted case and the overall layering mechanism operates in the usual way.

To sum, the simulation results for the double layered states perfectly match the predictions of the averaged dipolar potential U^{ID} . Hence, U^{ID} perfectly describes the particle

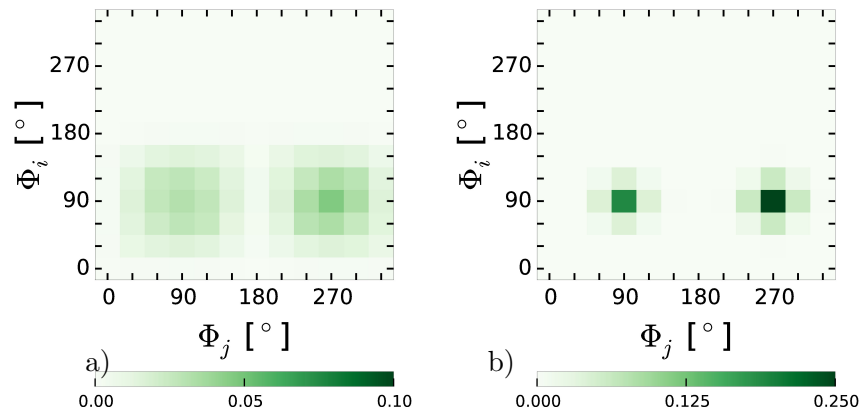


Figure 6.20.: Results of Eq. 6.17 for $\delta = 0.20$ and (a) $B_0^* = 11$, $\omega_0^* = 15$ or (b) $B_0^* = 12$, $\omega_0^* = 59$ (double layered state).

interactions in the double layered states, which thus correspond to energetically optimal configurations. Secondly, according to the simulation results, it is the increase of the frequency, which progressively directs the shift vectors towards these energetically optimal configurations.

6.5.2. Double Layer formation in Experiments

The formation of double layers in real colloidal systems consisting of magnetic Janus spheres exposed to a rotational magnetic field was recently reported by Granick *et al.* [84]. The authors prepare one hemisphere of spherical silica particles with magnetic material (nickel) in a particular way, using electron beam deposition which allows to precisely control the thickness of the magnetic material and thus the dipole offset from the particle centre (for details see the according Reference [84]). The authors state that the magnetic response of the particles is mainly in the direction parallel to the Janus interface. With this preparation, the geometry of the particles is covered by our model of laterally shifted dipoles. For the smallest coating thickness considered in the work, the authors report from the organization of the particles in double layered assemblies within which the magnetic caps of the particles point towards each other (see Fig. 2c and d in the Reference). This translational arrangement as well as the orientational arrangement of the shift vectors (the shift vectors in our model correspond to the direction from the particle centres to the magnetic caps in the real particles) perfectly coincide with our simulation and numerical results presented in the preceding sections (see sections 6.3 and 6.5.1). The experiment also shows that the double layered states only occur if the dipolar offset is sufficiently large, i.e. the shift is sufficiently high. This is also confirmed by our simulations as we do not observe double layer formation in the system with the smaller shift $\delta = 0.1$.

Different from our results is the perfect square symmetry in the experiment: Although our snap shots also indicate that there might be a (squared) lattice symmetry in the double layered states, we did not observe (yet also did not investigate in detail) *perfect* crystalline states for the parameters considered in this work. One reason for this might be that the shift used in our simulations might not perfectly match the offset due to the considered thickness of the coating in the experiment.

Nevertheless, the perfect agreement of our simulations with the experimental results in terms of the shift vectors as well as of the structural arrangements reveal that the model of laterally shifted dipoles, although very simple, very well serves for describing magnetic Janus particles in rotating fields although the magnetic response in the real particles are highly complex. The complexity stems from several facts, such as the curved surface of the hemispheres. Moreover, the response of Janus spheres used in the experiments, comprise a paramagnetic component which is assumed to be minor to the ferromagnetic one. It is known that the overall layering effect is due to the ferromagnetic response which makes the single particle rotation in a viscous medium [71, 42] crucial for the occurrence of layers and the excellent agreement of the simulation results gained with the model which does not take into account the paramagnetic component, confirms that also for the Janus particles, the crucial response is the ferromagnetic one.

6.6. Low frequency regime

The state diagram for the shift $\delta = 0.2$ (Fig. 6.5 (b)) comprises a region which is characterized by a failure of pattern formation. Specifically for field strengths $B_0^* < 12$ and low frequencies in the range $\omega_0^* \approx 3 - 25$, we do not observe any kind of translational order in the system, yet, this failure can be overcome, passing to stronger fields and or to higher frequencies. Apart from the occurrence of this "gap" in the state diagram, the question is to which extend its location near the lowest frequencies in the state diagram matters. Thus, in this section we aim at figuring out the origin of the absence of pattern formation in the said region as well as its relation to the field frequency.

Generally, the formation of layers is based on rotational and translational mechanisms, i.e., the external field governs the rotation of the particles via synchronisation and the herefrom following averaged dipolar potential directs the particles towards the specific translational order inherent in the layered states. Thus, we first examine the rotational aspect by considering the total magnetization, given in Eq. (6.8), as a function of the frequency and show the results in Fig. 6.21 for several field strengths. First of all, the value of the magnetization is rather high, i.e. above 0.85, being typical for synchronized states. However, it is clearly disturbed in the range where pattern formation is not observed whereby the disturbance is less distinct for higher field strengths. This can be understood by the fact that stronger fields clearly possess a higher ability to align and thus drive the dipoles. As a consequence,

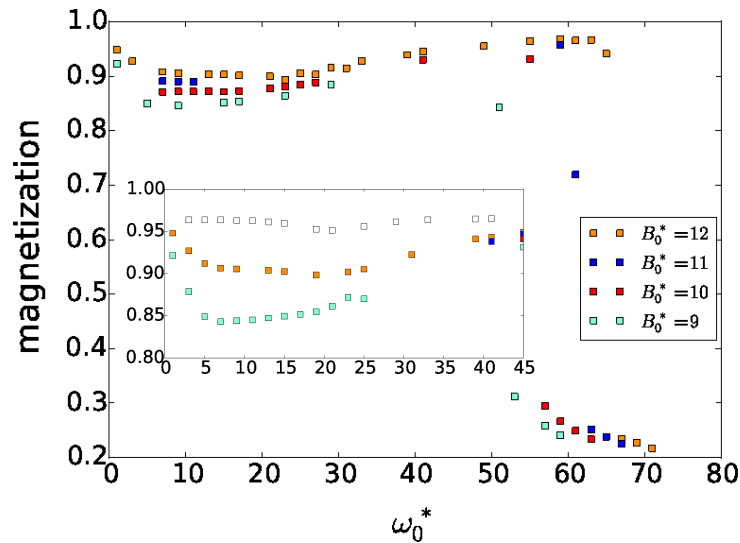


Figure 6.21.: Magnetization as a function of the frequency. The inset shows the magnification for low frequencies whereby the disturbance of the magnetization is in the range $\omega_0^* \approx 3 - 25$. The empty squares give the results of the reference system with $B_0^* = 12$.

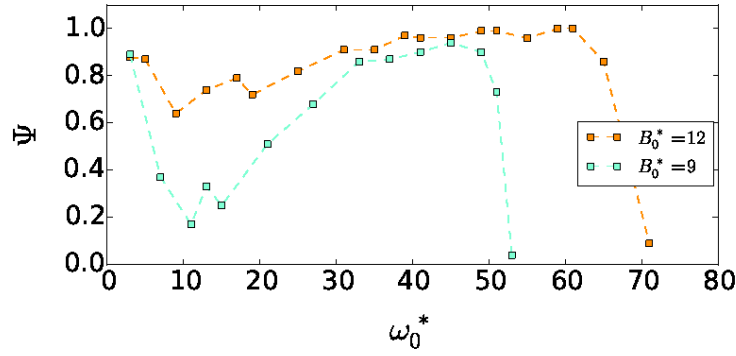


Figure 6.22.: Order parameter Ψ as a function of the frequency.

the occurring layers are either less distinct or layers do not appear at all for decreasing field strengths, as can be seen by the layering parameter Ψ , which is in the same way disturbed in the range $\omega_0^* \approx 3 - 25$ for $B_0^* = 12$ or which even falls below the limit value Ψ^{th} describing layer formation, for $B_0^* = 9$.

In a next step, we consider the translational organization of the particles, i.e. we examine the relative organization of two nearest neighbouring particles w.r.t. the direction of the external field. To this end, we determine the distribution of the angle α' between the centre-to-centre distance vector and B , for $B_0^* = 12$ and the frequencies $\omega_0^* = 3$, $\omega_0^* = 7$, $\omega_0^* = 39$ (see Fig. 6.23). For the smallest frequency the two peaks in the distribution

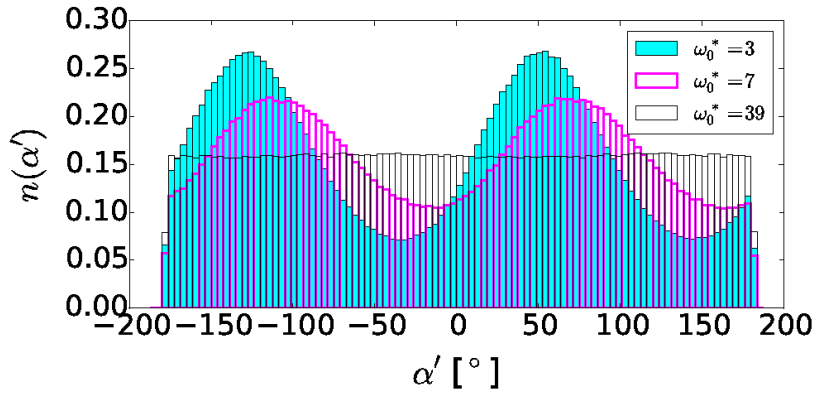


Figure 6.23.: Distribution (see Eq. 6.9) of the angle α' between the centre-to-centre distance vector of nearest neighbours and the direction of the field, with $dx = \pi/48$. For the lowest frequency, the pairs arrange in a staggered manner along a line having a fixed angle to the field, however, this cannot be maintained, passing to higher frequencies, due to frictional forces.

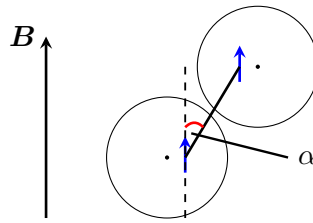


Figure 6.24.: Sketch of the staggered chain configuration. The dipolar potential of the pair becomes repulsive for $\alpha > \approx 54.74^\circ$. Rotation of the dipoles increases α , due to synchronization, however, the particles can counteract this by translation, in the quasi-static frequency regime $\omega_0^* < \approx 5.84$. In the resonant-like regime, the increase of α cannot be overcome solely by translation anymore, due to frictional hindrance, such that the two dipoles get drawn back against the field rotation in order to decrease α , if the field strength is not sufficiently high. This leads to a disturbance of synchronization and thus to a failure of pattern formation in the "gap" of the state diagram.

correspond to a staggered chain configuration, within the layers, with a fixed acute angle $\alpha' \approx 50^\circ$ resulting in an arrangement along a line which is parallel to the field direction. A sketch can be seen in Fig. 6.24. However, this configuration cannot be maintained for increasing frequency and finally, it is completely given up if the frequency passes to even higher values. In the idealized picture of the staggered chain configuration, the dipolar potential is a function of the angle α , defined in Fig. 6.24. For values larger than $\alpha \approx 54.74^\circ$, it becomes repulsive, for a fixed dipolar distance. Typical values in the simulations for very low frequencies are less than this value. Specifically for e.g. $\omega_0^* = 3$, we measure the value $\alpha \approx 30^\circ$, which we assume to be the value optimizing the dipolar potential for the staggered chain configuration. Starting from this configuration, the perfectly synchronized dipolar rotations will increase α , i.e. the dipolar potential will become less attractive, yet, the particles compensate this increase by translation to convenient positions in order to decrease the value for α and thereby prevent dipolar repulsion. Note that the particles do not keep their initial neighbours, as the examination of the pair dynamics in section 6.5 for $\omega_0^* = 3$ revealed. Thus, the particles steadily reorganise with new neighbours in the vicinity in order to reduce the angle α . This process is the origin of the two peaks in the distribution of α' and can be maintained as soon as the frequency of dipolar rotations are much smaller than the translational dynamics of the particles. If the field rotates increasingly faster, and with it the synchronized dipoles, translational reorganization of the particles has to come about faster in order to maintain the process which minimized α . However, frictional forces prevent the particles to reorganize to optimal arrangements and

thus, the according peaks in Fig. 6.23 vanish upon the increase of ω_0^* . As a measure of translational frictional hindrance, we use the Brownian relaxation time $\tau_B = m/\gamma$ [78] which is defined for non-interacting Brownian particles of mass m in a solvent with friction coefficient γ . Similar as in the effective single particle theory (sec. 6.11), which yielded very good results for the description of the high frequency border in the state diagram, using τ_B as a systems measure, we consider effectively a single particle to be in a viscous medium with friction coefficient γ . For our systems, this time is $\tau_B^* = 1/\xi_t \approx 0.074$, with $\gamma = \xi_t = k_B T/D_t$, and thus serves as a common measure for all frequencies. Further, we define the time τ to be the time during which the change in α , starting from the staggered chain configuration with $\alpha = 30^\circ$, results in $\alpha > \approx 54.74^\circ$, due to dipolar rotations. Thus $\tau = \frac{d\alpha}{\omega_0^*} = \frac{54.74^\circ - 30^\circ}{\omega_0^*} = \frac{0.14\pi}{\omega_0^*}$. Comparing τ with τ_B^* , one finds (see table 6.1) that for $\omega_0^* = 3$, translational dynamics is about twice as fast as rotational dynamics. More precisely, the dipolar rotations need twice as long to result in the configuration with $\alpha \approx 54.74^\circ$, as the particles' velocities relax. We thus identify this and comparable frequencies as the quasi-static regime. Further, for $\omega_0^* = 7$, rotation has overtaken translation and τ becomes comparable with τ_B^* , i.e., rotational and translational dynamics of the particles happen on comparable time scales. We call this region the "resonant-like" regime. In this regime, caused by frictional forces, the particles only hardly can compensate the increase of the angle α by translation. Specifically, for $\omega_0^* \approx 5.84$, $\tau = \tau_B^*$ holds and the "resonant-like"

Table 6.1.: Comparison of translational and rotational time scales for the frequencies shown in Fig. 6.23.

ω_0^*	τ/τ_B^*
3	1.95
7	0.83
39	0.15

regime is entered -while at the same time the end of the quasi-static regime is marked- which is also consistent with the onset of the disturbances of the magnetization and the order parameter, shown in Figs. 6.21 and 6.22. Now, with the help of the staggered chain picture, one also understands this disturbance of the magnetization: In the staggered chain configuration with $\alpha = 30^\circ$, we estimate the dipolar distance to be about $r' = 0.7\sigma$. The rotating field will drive the rotation of both of the dipoles, yet, it has to dominate over the dipolar potential of the pair which is optimal for $\alpha = 30^\circ$. Thus, the field strength has to be at least $B_0^* > |\mu/r'^3 \cdot (1 - 3\cos^2(\alpha))| \approx 10.93$. Indeed, layer formation for $B_0^* > 10$ is observed also in the resonant-like regime. Otherwise, the dipoles are drawn back against the field rotation in order to reduce the dipolar potential, i.e. α , which thus causes the disturbance of the magnetization. Interestingly, the crossover to the "resonant-like" regime is accompanied by a realignment of the pairwise shift vectors, discussed above, which also

pass towards configurations which are conform with double layers (Fig. 6.25). Beyond the "resonant-like" regime in the state diagram, i.e. the re-entrance to layered states, particle rotation is much more faster than translation such that the staggered chain configuration is given up in favour of configurations rather corresponding to double layers.

We conclude that in the region of the state diagram where no pattern formation is observed at all, the mentioned two effects interfere each other: On the one hand, the field strength is not sufficiently high and thus fails to perfectly align the dipoles, due to which the averaged dipolar potential does not fully operate. On the other hand, the "resonant-like" effect causes an additional disturbance such that all in all, no stable patterns can be formed. Yet, once the "resonances" are overcome, also for the smaller field strengths, layers occur anew.

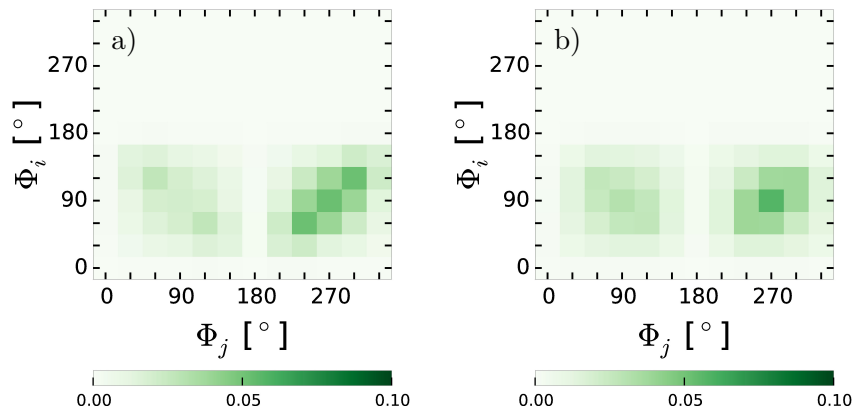


Figure 6.25.: Results of Eq. (6.17) for $\delta = 0.20$ with $B_0^* = 9$ and (a) $\omega_0^* = 3$ or (b) $\omega_0^* = 9$. The shift vectors experience a realignment across the border from the quasi-static to the resonant-like regime in the state diagram.

6.7. Comparison to radial shifts

In this final section, we study radially shifted dipoles in the same rotating fields considered in the previous parts of this work, and compare the features of radial shifts in terms of layer formation with those of lateral shifts. This comparison will allow to get insight of the influence of the specific particle geometry on layer formation.

The geometry of radially shifted dipoles is sketched in Fig. 6.26 and includes the property that the shift vector is parallel to the dipole vector, thus to the field direction, if the dipoles are synchronized with the field. This has crucial consequences on the system. Firstly, the orientation of the shift vector is uniquely determined by the field direction. Secondly, the distance vector of a pair of synchronized dipoles coincides with that of a pair of centred dipoles. Thus, the averaged dipolar potential of the pair is given by Eq. (A.2), which in turn yields the formation of conventional layers, just as centred dipoles.

In Fig. 6.27, we show snap shots of the same system studied in the previous sections, with $\delta = 0.2$ and $B_0^* = 12$ for different, increasing frequencies. The type of the occurring layers are the same as for the reference system and, noticeably, double layers are not formed, if the frequency is increased. This is confirmed by the results of the order parameter Ψ_{DL} introduced in section 6.5, which is compared to that of the lateral shift for increasing frequency in Fig. 6.28.

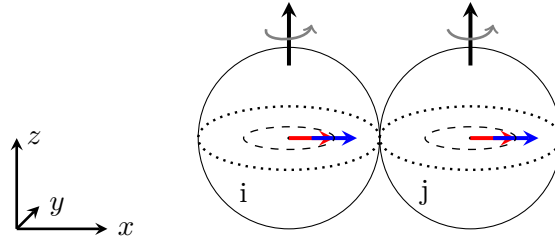


Figure 6.26.: (Colours and symbols are the same as in Fig. 6.2) Pair with radially shifted and synchronized dipoles. Their dipolar distance vector coincides with that of a pair with centred dipoles. Thus, the averaged dipolar potential is therefore the same as in the centred case, which is a result of the symmetry of the radial shift for which the orientation of the shift vector is uniquely determined by the field direction. It follows herefrom that radially shifted dipoles in a rotating field form conventional layers as in the centred case. The formation of double layers, as in the case with lateral shifts, is not possible.

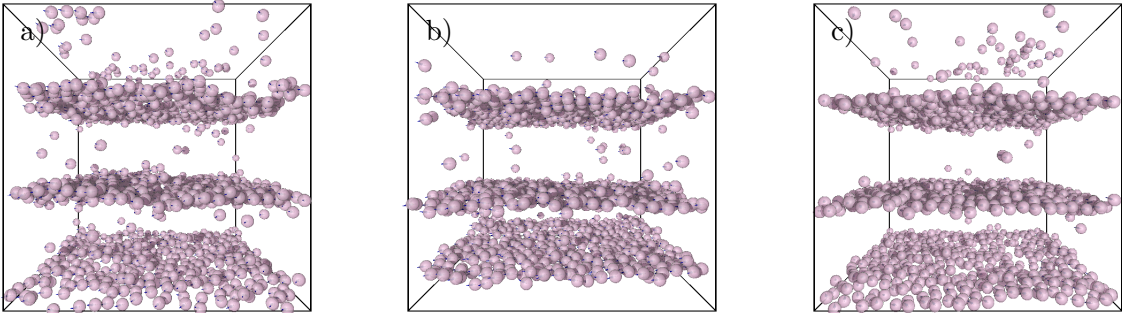


Figure 6.27.: Snapshots for radial shifts with $\delta = 0.20$ and $B_0^* = 12$. (a) $\omega_0^* = 15$, (b) $\omega_0^* = 31$, (c) $\omega_0^* = 59$. Double layers do not form for radial shifts upon the increase of the frequency.

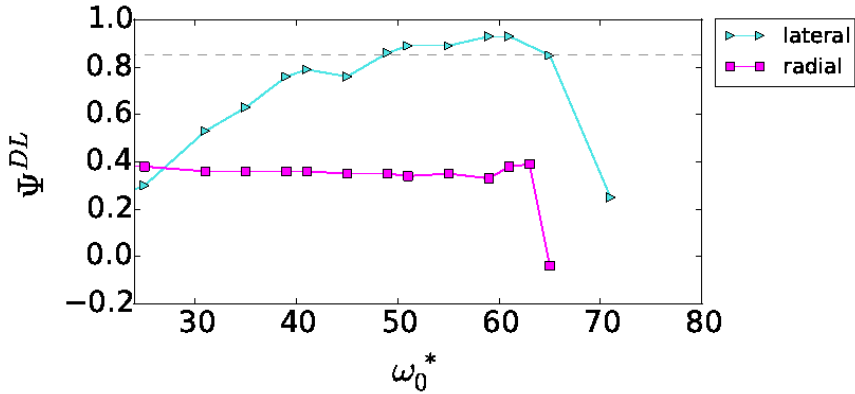


Figure 6.28.: Order parameter Ψ_{DL} as a function of ω_0^* for radial and lateral shifts with $\delta = 0.2$ and $B_0^* = 12$. The broken line marks the threshold value $\Psi_{DL} = 0.85$ for double layers.

6.8. Summary

The average dipolar potential for a pair of laterally shifted dipoles synchronized with the rotating field is complex due to the generally time-dependent dipolar distance vector of the pair and due to the additional degrees of freedom in the field perpendicular plane, which are provided by the geometry of the lateral shift.

The numerically gained results of U^{ID} yielded that the overall feature of the average dipolar potential leading to layer formation in the reference system is preserved for shifted dipoles. Apart from the confirmation of layer formation in the shifted system, computer simulations proved the existence of double layers near the high frequency border in the state diagram for the shift $\delta = 0.2$, accompanied by a transition of the shift vector orientations towards specific configurations predicted by the average dipolar potential.

Noticeably, double layer formation of magnetic Janus particles in a rotating magnetic field were recently found in experiments.

7

Conclusion and Outlook

In this work, we considered a model of spherical colloidal particles carrying a laterally shifted magnetic dipole moment. The main goal was to examine the impact of the offset of the dipole moment from the particle centre on pattern formation in 3D systems of such particles in equilibrium as well as in an external rotating magnetic field. Our model belongs to a group of models including radial shifts [43, 44] of the dipole moment or shifts with arbitrary orientations of the dipole vector within the particles [47, 67]. The interest and need for such models stem from real colloidal particles carrying a non central located dipole moment which provokes not only new types of self assembled structures, serving as building blocks for novel materials e.g., but also interesting fundamental physics such as synchronization driven pattern formation [40]. By all means, it is indispensable to understand the mechanisms of self-assembly in such systems on the level of single particles, and with our investigations, we aimed at making a contribution to the findings on this field of soft matter.

In the following, we conclude our findings of the according systems considered in this thesis and suggest the routes for further investigations.

Zero and finite temperature systems

The examination of the shift dependent ground states of systems with two, three and four hard spheres with laterally shifted dipoles yielded that the principle of energy minimization is realized primarily by the minimization of the dipolar distances, being enabled by the shift of the dipoles, because the dipolar distance contributes to the anisotropic potential with the third inverse power. In turn, this is paid with the successive renouncement of the parallel head-to-tail configuration of the dipoles (which optimizes the dipolar potential) towards

antiparallel dipolar orientations. For the cases $N > 2$, this provokes structural transitions from chainlike to triangular (for $N = 3$) or from ring to tetragonal ($N = 4$) arrangements of the particle centres. We note that our findings for $N = 3$ differ from that suggested in Ref. [67] and comprise smaller energies. Besides, they are more convenient with the principle of dipolar distance minimization. For details, see section 4.0.6. Noticeably, the case $N = 4$ is the smallest system enabling 3D structures which are only realized for sufficiently large shifts. All other structures occurring are planar, being the only geometrically possible arrangement for $N = 2$ and $N = 3$.

On all accounts, it is not only the offset of the dipole moment from the particle centre but also its orientation within the particle which fundamentally affects the forming structures. So, radial shifts e.g. show no variations of the ground state structures for shifts near the centre, which is different for lateral shifts. Thereby, the larger the shift, the dramatic is the variation of the emerging structures.

In bulk systems of laterally shifted dipoles at finite temperature, the crucial effect of shifting the dipole is reflected by the structural transition from chainlike structures for shifts near the centre to small and close-packed clusters corresponding to the ground state structures of two, three and four particles, for high shifts near the limit value $\delta = 0.33$. Clearly, this transition is driven by the increase of the dipolar coupling strength λ with increasing shifts towards values for which dipolar energy dominates over thermal energy. The effect of temperature in the bulk systems manifests itself by the existence of self-assembly structures which are not observed in the ground state configurations, such as rings of staggered chains, in the intermediate shift region. We interpret this region as a transition region between the small and large shift regimes, in which the competition of energy minimization and entropy maximization results in the coexistence of chainlike as well as close-packed aggregates, aside from large closed-ring assemblies.

The observed structural transition across the three shift regimes being small, intermediate and high, proceeds continuously such that it is very difficult, not to say not possible, to identify distinct shift values which mark the transition borders.

Overall, although the shift crucially affects the forming self-assembly structures, small shifts result in very similar structures as the centred dipoles. Thus, even if the ability to form chains is increased, reflected by longer chains, this shift regime can be regarded as a perturbation of conventional dipolar systems, while real impact of the shift becomes perceivable only for shifts larger $\delta \approx 0.2$.

So far we provided insights about the shift driven self-assembly in such 3D systems, yet did not investigate the interaction between the occurring clusters. Although our study of the net magnetization per cluster, which vanishes for high shifts, indicates that cluster interactions especially for high shifts can be neglected. Nevertheless, this interaction for smaller shifts should be examined in order to enlarge the picture of behaviour of such systems. Our investigations were limited to thermodynamic states corresponding to the isotropic state for dipolar systems with centred dipoles, and we did not get any hint for

phase transitions due to the shift. For further investigations, it would be desirable to determine a full phase diagram, especially for the relevant case $\delta \approx 0.2$, with regard to the isotropic liquid, ferroelectric and solid phases and to transitions between them, known from dipolar systems with centred dipoles [86, 16, 19]. However, also small shifts, even if their structural appearance do not yield new physics in the considered thermodynamic states, might become interesting in the low density and/or low temperature regime, in which dipolar hard spheres organise in rings, rather than in chains, or form junctions [8]. Based on dipolar interactions, the probabilities for the occurrences of chains, rings and junctions might be highly affected by the shift of the dipole.

Pattern formation in a rotating magnetic field

Driving the 3D bulk system out of equilibrium via a rotating magnetic field, steady states characterized by a layered organization of the particles are also found in the shifted systems which we limited to the cases $\delta = 0.1$ and $\delta = 0.2$. The analysis of the system for the total range of shifts is not possible and also not necessary because the value $\delta = 0.1$ is representative for small shifts, according to our experiences, while $\delta = 0.2$ belongs to values for which the shift becomes relevant.

For $\delta = 0.1$, the state diagram nearly perfectly coincides with that of the reference system, i.e. the mechanisms of pattern formation are the same and the shift does not generate any novelties beyond the known behaviour of centred dipoles in the same rotating field. Thus, small shifts can be regarded as a perturbation of the reference system.

More interesting is the case $\delta = 0.2$. For this, the averaged dipolar potential U^{ID} is highly affected by the shift which causes a time-dependent dipolar distance in a pair of synchronized shifted dipoles, and holds an additional anisotropy caused by the additional degrees of freedom, i.e. the orientations of the shift vectors in the field perpendicular plane. The numeric analysis of U^{ID} prescribes the formation of double layers as energetically favourable arrangements. These are characterized by anti parallel orientations of the shift vectors along the laboratory z -axis, of close by particles. In practice however, the behaviour of the particles is crucially determined by the frequency of the driving field due to the friction with the solvent. First of all, on the single particle level, synchronization with the external field is governed by the same mechanism as for centred dipoles which is why the high frequency border in the state diagram perfectly matches that one of the reference system. For frequencies beyond this border, rotational friction prevents synchronous rotation of the dipoles such that layer formation breaks down. The match of the high frequency borders of the centred and the shifted systems implies that synchronization as a necessary condition for layer formation is also maintained as a condition in the shifted systems.

Furthermore, the field frequency dictates the collective rotational dynamics beyond the synchronous rotations of the dipoles. More precisely, if the frequency approaches the high frequency border from lower values, the shift vectors pass from a state in which they

dynamically reorient within the field perpendicular plane, to a state in which they are locked to the orientation dictated by U^{ID} , and the arrangement of the particles pass from single to double layers. At the same time, also the collective translational dynamics experience a transition from a dynamic state at low frequencies for which the particles permanently exchange nearby particles, to a static state in the sense that the particles keep their nearest neighbours, i.e. the particles are caught within their assemblies. Thus, we differentiate between the following three types of collective dynamics and the transitions therein upon the increase of the frequency:

- (a) synchronous rotation of the dipoles: passing from quasi static to dynamic, according to the frequency
- (b) translational dynamics: passing from dynamic to static states
- (c) orientations of the shift vectors: passing from dynamic to a locked state.

Notably, rotational (referred to the dipoles) and translational dynamics evolve inversely (see Fig. 7.1).

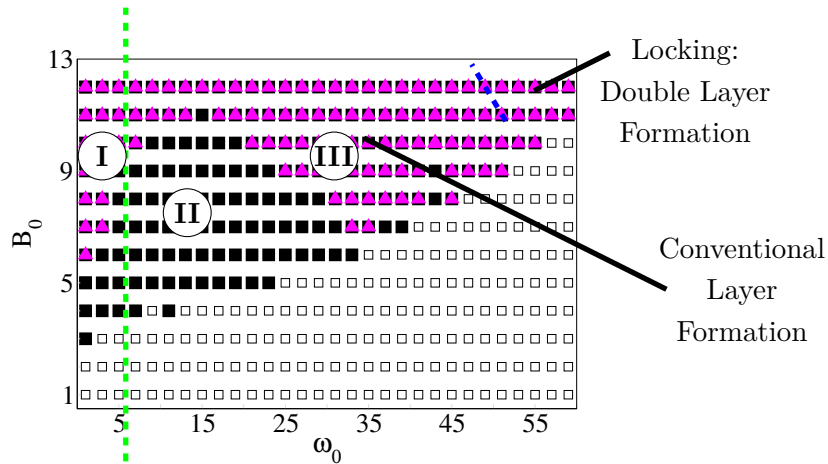


Figure 7.1.: State diagram of Fig. 6.5 (b). I: State with quasi-static dipolar rotations and dynamic translation. II: Failure of pattern formation, here rotational and translational time scales are comparable. III: Dynamic rotations and static translation in the sense that the particles hardly dissolve from their assemblies. The green dashed line marks the end of region I. The blue dashed line marks the beginning of the double layered states.

Clearly, it is the geometry of the laterally shifted dipoles which entails complexities of U^{ID} and at the same time widens its operation. Thus, for all cases considered, synchronization is a necessary condition for overall layering, and additionally, locking is a sufficient condition provoking double layer formation. An overview of the different states within the state

diagram is given in Fig. 7.1. In contrast, radial shifts show exactly the same behaviour as the reference system, hence it is not only the amount of shift but also the orientation of the dipole moment what crucially determines the systems behaviour.

The dynamic transitions discussed above are carried out continuously and are accompanied by a structural transition. Having in mind that the increase of the field frequency, and with it that of the synchronous dipolar rotations, regulates the translational dynamics of the particles, we conclude that also translational frictional forces are directly related to the increase of the field frequency. More precisely, without having checked in detail, we assume an increase of translational frictional forces with increasing frequency. Thus, the successively upcoming double layer formation can be interpreted as a response to friction which thus is eluded by confining translational as well as orientational dynamics (i.e. locking of the shift vectors). However, the double layer formation is also accompanied by a reduction of entropy because the number of accessible states of the shift vectors is reduced to two orientations. Therefore, one also might interpret the successive, rather than the abrupt, upcoming of the double layers as follows: Before entering the double layered states, the system seeks entropy maximization, while towards higher frequencies, it more and more follows the principle of energy minimization, being guided by friction, which also explains why double layer formation does not occur for lower frequencies.

Also at even lower frequencies (region labelled with 'II' in Fig. 7.1 and tentatively called 'resonant-like' regime), friction played a role in terms of layer formation. A comparison of the translational time scale, determined by the friction coefficient ξ_T , to that of rotation, determined by the field frequency, yielded that for comparable translational and rotational time scales, the particles cannot sufficiently fast translate in order to prevent configurations with repulsive dipolar potentials. This idea is supported by test simulations which we conducted with altered ξ_t . The results imply that a decrease (an increase) of ξ_t by 5% reduces (enlarges) the extent of the black region.

Striking is the fact that region 'II' (see Fig. 7.1) does not appear in the state diagram for centred dipoles. We speculate that this region and the absence of pattern formation is related to pair interactions which are obviously different than that of the centred dipoles and are highly determined by the anisotropic particle geometry in 3D. Probably, this region might constitute a transition region between the regions 'I' and 'III'.

The system of laterally shifted dipoles with sufficiently large δ in a rotating magnetic field is a highly complex system and the results in this thesis pose further open questions. To these belong the derivation of models which explain the borders of region II quantitatively. Specifically the examination of the influence of the solvent, i.e. explicitly including hydrodynamic interactions, is expected to be enlightening in this context and helpful for a description of the transitions related directly to the field frequency. This may be approached in the framework of a dynamic density functional theory including hydrodynamic interactions [93, 94, 95].

Regarding the modelling of magnetic Janus spheres, our results very well reproduces the

formation of double layers observed experimentally. However, in the simulations, we could not consider and also not confirm the bond orientational order in detail. In further works, this issue and with it the more exact modelling might be further developed. Particularly, the open question regarding the complex response of real Janus particles of Ref. [84] should be addressed more accurately.

In this thesis, we concentrated on the effect of the location and the orientation of the dipole moment on pattern formation and the underlying collective dynamical aspects for which the nonequilibrium phenomena synchronization and locking play a crucial role. Interesting would be the examination of the effect of shifting on further aspects of such systems such as thermal conductivity or viscosity of the suspension. Especially from a practical point of view these are important quantities which constitute sources of novel applications based on e.g. thermophoresis or shear melting. Furthermore, recent research considers systems in which the usually liquid solvent used in ferrofluids is exchanged by polymer networks [96] (ferrogel) or by liquid crystalline particles (usually in addition to water) [97, 98, 99, 100, 101]. As our results demonstrated, the geometry of the magnetic particles crucially dictates the systems behaviour and thus, shifting the dipole moment of the magnetic colloids in these mentioned systems offers an additional control parameter and widens the practical potential of these 'smart' materials immensely. Finally, our results contribute to the general knowledge of systems with shifted dipoles and in terms of general physics, they may be referenced as a starting point for the examination of variations of our system, achieved by e.g. triaxial or even inhomogeneous external fields. The dynamic behaviour as well as the self-assembly principles in these systems are expected to yield new patterns which are formed due to the laterally shifted geometry.

Appendices



Centred Dipoles: Layer formation in the reference system

In a rotating magnetic field $\mathbf{B} = B_0(\cos \omega_0 t, \sin \omega_0 t, 0)$, the orientations of a pair of dipoles synchronized with the external field are given by

$$\boldsymbol{\mu}_i(t) = \boldsymbol{\mu}_j(t) = \mu(\cos \omega_0 t, \sin \omega_0 t, 0). \quad (\text{A.1})$$

At any time, the dipolar distance \mathbf{r}' (see section 2.1) of non-shifted dipoles equals the center to center distance \mathbf{r} and is constant

$$\mathbf{r}' = \mathbf{r} = (r \cos \phi \sin \theta, r \sin \theta \sin \phi, r \cos \theta),$$

with $r = |\mathbf{r}|$ (see Fig. A.1). Followingly, the time average of the dipolar potential over one rotational period gives the averaged dipolar potential

$$U^{ID} = \tau^{-1} \int_{t_0}^{t_0+\tau} u_D(\mathbf{r}, \boldsymbol{\mu}_i(t), \boldsymbol{\mu}_j(t)) dt = -\mu^2(1 - 3 \cos^2 \theta)/(2r^3) \quad (\text{A.2})$$

whith $\tau = 2\pi/\omega_0$ being the rotational period of the field. The value for the angle θ between the z -axis and the distance vector \mathbf{r} is decisive for U^{ID} to be attractive (if $\cos^2 \theta < 1/3$) or

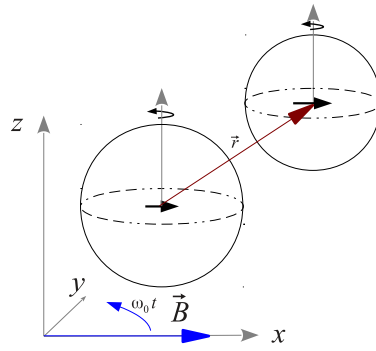


Figure A.1.: Two non-shifted synchronized dipoles have a constant dipolar distance $\vec{r}' = \vec{r} = (r \cos \phi \sin \theta, r \sin \theta \sin \phi, r \cos \theta)$. The averaged dipolar pair potential in this case is given by Eq. (A.2).

repulsive (if $\cos^2 \theta > 1/3$). Thus, two particles either attract and arrange in the same layer or the orientation of their distance vector results in a repulsive interaction and they organize in different layers for appropriate field strengths and frequencies. A state diagram separating layered from non-layered states was computed among others in previous works [71].

Bibliography

- [1] A. Einstein, "Über die von der molekularkinetischen Theorie der Wärme geforderte Bewegung von in ruhenden Flüssigkeiten suspendierten Teilchen," *Annalen der Physik*, vol. 322, no. 8, pp. 549–560, 1905.
- [2] R. E. Rosensweig, *Ferrohydrodynamics*. Cambridge University Press, 1985.
- [3] Odenbach, "Ferrofluids," *Handbook of Magnetic Materials*, Ed. K.H.J. Buschow, vol. 16, 2006, Elsevier B. V.
- [4] S. Odenbach, "Ferrofluids - magnetically controlled suspensions," *Colloids and Surfaces A: Physicochemical and Engineering Aspects*, vol. 217, no. 1–3, pp. 171 – 178, 2003, symposium C of the E-MRS 2002 Spring Meeting in Strasbourg, France.
- [5] J. Chomoucka, J. Drbohlavova, D. Huska, V. Adam, R. Kizek, and J. Hubalek, "Magnetic nanoparticles and targeted drug delivering," *Pharmacological Research*, vol. 62, no. 2, pp. 144 – 149, 2010, towards clinical applications of nanoscale medicines.
- [6] M. Bañobre-López, A. Teijeiro, and J. Rivas, "Magnetic nanoparticle-based hyperthermia for cancer treatment," *Reports of Practical Oncology & Radiotherapy*, vol. 18, no. 6, pp. 397 – 400, 2013.
- [7] C. Felton, A. Karmakar, Y. Gartia, P. Ramidi, A. S. Biris, and A. Ghosh, "Magnetic nanoparticles as contrast agents in biomedical imaging: recent advances in iron- and manganese-based magnetic nanoparticles," *Drug Metabolism Reviews*, vol. 46, no. 2, pp. 142–154, 2014, pMID: 24754519.
- [8] L. Rovigatti, J. Russo, and F. Sciortino, "No evidence of gas-liquid coexistence in dipolar hard spheres," *Phys. Rev. Lett.*, vol. 107, p. 237801, Nov 2011.
- [9] M. J. Stevens and G. S. Grest, "Phase coexistence of a stockmayer fluid in an applied field," *Phys. Rev. E*, vol. 51, pp. 5976–5984, Jun 1995.
- [10] J. Bartke and R. Hentschke, "Phase behavior of the stockmayer fluid via molecular dynamics simulation," *Phys. Rev. E*, vol. 75, p. 061503, Jun 2007.
- [11] J. Caillol, "Search of the gas-liquid transition of dipolar hard spheres," *The Journal of Chemical Physics*, vol. 98, no. 12, pp. 9835–9849, 1993.

- [12] M. S. Wertheim, "Exact solution of the mean spherical model for fluids of hard spheres with permanent electric dipole moments," *The Journal of Chemical Physics*, vol. 55, no. 9, pp. 4291–4298, 1971.
- [13] P. G. de Gennes and P. A. Pincus, "Pair correlations in a ferromagnetic colloid," *Physik der kondensierten Materie*, vol. 11, no. 3, pp. 189–198, 1970.
- [14] M. E. van Leeuwen and B. Smit, "What makes a polar liquid a liquid?" *Phys. Rev. Lett.*, vol. 71, pp. 3991–3994, Dec 1993.
- [15] A.-P. Hynninen and M. Dijkstra, "Phase behavior of dipolar hard and soft spheres," *Phys. Rev. E*, vol. 72, p. 051402, Nov 2005.
- [16] S. Klapp and F. Forstmann, "Stability of ferroelectric fluid and solid phases in the stockmayer model," *EPL (Europhysics Letters)*, vol. 38, no. 9, p. 663, 1997.
- [17] P. J. Camp, J. C. Shelley, and G. N. Patey, "Isotropic fluid phases of dipolar hard spheres," *Phys. Rev. Lett.*, vol. 84, pp. 115–118, Jan 2000.
- [18] D. Levesque and J.-J. Weis, "Stability of solid phases in the dipolar hard sphere system," *Molecular Physics*, vol. 109, no. 23-24, pp. 2747–2756, 2011.
- [19] S. H. L. Klapp, "Dipolar fluids under external perturbations," *Journal of Physics: Condensed Matter*, vol. 17, no. 15, p. R525, 2005.
- [20] A. Yethiraj and A. van Blaaderen, "A colloidal model system with an interaction tunable from hard sphere to soft and dipolar," *Nature*, vol. 421, pp. 513–517, Jan 2003.
- [21] K. Butter, P. Bomans, P. Frederik, G. Vroege, and A. Philipse, "Direct observation of dipolar chains in iron ferrofluids by cryogenic electron microscopy," *Nature Materials*, vol. 2, pp. 88–91, Jan 2003.
- [22] J. Jordanovic, S. Jäger, and S. H. L. Klapp, "Crossover from normal to anomalous diffusion in systems of field-aligned dipolar particles," *Phys. Rev. Lett.*, vol. 106, p. 038301, Jan 2011.
- [23] J. E. Martin and A. Snezhko, "Driving self-assembly and emergent dynamics in colloidal suspensions by time-dependent magnetic fields," *Reports on Progress in Physics*, vol. 76, no. 12, p. 126601, 2013.
- [24] J. F. Douglas, "Membrane magic," *Nature Materials*, vol. 463, pp. 302–303, Jan 2010.
- [25] N. Osterman, I. Poberaj, J. Dobnikar, D. Frenkel, P. Zihlerl, and D. Babić, "Field-induced self-assembly of suspended colloidal membranes," *Phys. Rev. Lett.*, vol. 103, p. 228301, Nov 2009.

- [26] P. I. C. Teixeira, J. M. Tavares, and M. M. T. da Gama, "The effect of dipolar forces on the structure and thermodynamics of classical fluids," *Journal of Physics: Condensed Matter*, vol. 12, no. 33, p. R411, 2000.
- [27] C. Holm and J.-J. Weis, "The structure of ferrofluids: A status report," *Current Opinion in Colloid & Interface Science*, vol. 10, no. 3–4, pp. 133–140, 2005.
- [28] A. Walther and A. H. E. Müller, "Janus particles: Synthesis, self-assembly, physical properties, and applications," *Chemical Reviews*, vol. 113, no. 7, pp. 5194–5261, 2013.
- [29] A. Perro, S. Reculosa, S. Ravaine, E. Bourgeat-Lami, and E. Duguet, "Design and synthesis of janus micro- and nanoparticles," *J. Mater. Chem.*, vol. 15, pp. 3745–3760, 2005.
- [30] I. Schick, S. Lorenz, D. Gehring, S. Tenzer, W. Storck, K. Fischer, D. Strand, F. Laquai, and W. Tremel, "Inorganic janus particles for biomedical applications," *Beilstein J. Nanotechnol.*, vol. 5, pp. 2346–2362, 2014.
- [31] S. Sacanna, L. Rossi, and D. J. Pine, "Magnetic Click Colloidal Assembly," *J. Am. Chem. Soc.*, vol. 134, no. 14, pp. 6112–6115, APR 11 2012.
- [32] S. C. Glotzer and M. J. Solomon, "Anisotropy of building blocks and their assembly into complex structures," *Nature Materials*, vol. 6, no. 8, pp. 557–562, AUG 2007.
- [33] P. F. Damasceno, M. Engel, and S. C. Glotzer, "Predictive self-assembly of polyhedra into complex structures," *Science*, vol. 337, no. 6093, pp. 453–457, 2012.
- [34] E. Jankowski and S. C. Glotzer, "Screening and designing patchy particles for optimized self-assembly propensity through assembly pathway engineering," *Soft Matter*, vol. 8, pp. 2852–2859, 2012.
- [35] L. Cademartiri and K. J. M. Bishop, "Programmable self-assembly," *Nature Materials*, vol. 15, no. 14, pp. 2–9, 2016.
- [36] Étienne Duguet, C. Hubert, C. Chomette, A. Perro, and S. Ravaine, "Patchy colloidal particles for programmed self-assembly," *Comptes Rendus Chimie*, vol. 19, no. 1–2, pp. 173 – 182, 2016, emerging Chemistry in France.
- [37] P. Tierno, "Recent advances in anisotropic magnetic colloids: realization, assembly and applications," *Phys. Chem. Chem. Phys.*, vol. 16, pp. 23 515–23 528, 2014.
- [38] S. Sacanna, D. J. Pine, and G.-R. Yi, "Engineering shape: the novel geometries of colloidal self-assembly," *Soft Matter*, vol. 9, pp. 8096–8106, 2013.
- [39] D. Zerrouki, J. Baudry, D. Pine, P. Chaikin, and J. Bibette, "Chiral colloidal clusters," *Nature*, vol. 455, no. 7211, pp. 380–382, SEP 18 2008.

- [40] J. Yan, M. Bloom, S. C. Bae, E. Luijten, and S. Granick, "Linking synchronization to self-assembly using magnetic janus colloids," *Nature*, vol. 491, no. 7425, pp. 578–581, NOV 22 2012.
- [41] B. Ren, A. Ruditskiy, J. H. K. Song, and I. Kretzschmar, "Assembly behavior of iron oxide-capped janus particles in a magnetic field," *Langmuir*, vol. 28, no. 2, pp. 1149–1156, 2012, pMID: 22149478.
- [42] J. Yan, S. C. Bae, and S. Granick, "Rotating crystals of magnetic janus colloids," *Soft Matter*, vol. 11, pp. 147–153, 2015.
- [43] S. Kantorovich, R. Weeber, J. J. Cerda, and C. Holm, "Magnetic particles with shifted dipoles," *Journal of Magnetism and Magnetic Materials*, vol. 323, no. 10, pp. 1269 – 1272, 2011, proceedings of 12th International Conference on Magnetic Fluid.
- [44] —, "Ferrofluids with shifted dipoles: ground state structures," *Soft Matter*, vol. 7, pp. 5217–5227, 2011.
- [45] M. Klinkigt, R. Weeber, S. Kantorovich, and C. Holm, "Cluster formation in systems of shifted-dipole particles," *Soft Matter*, vol. 9, pp. 3535–3546, 2013.
- [46] L. Baraban, D. Makarov, M. Albrecht, N. Rivier, P. Leiderer, and A. Erbe, "Frustration-induced magic number clusters of colloidal magnetic particles," *Phys. Rev. E*, vol. 77, p. 031407, Mar 2008.
- [47] A. I. Abrikosov, S. Sacanna, A. P. Philipse, and P. Linse, "Self-assembly of spherical colloidal particles with off-centered magnetic dipoles," *Soft Matter*, vol. 9, pp. 8904–8913, 2013.
- [48] M. R. Khadilkar and F. A. Escobedo, "Heuristic rule for binary superlattice coassembly: Mixed plastic mesophases of hard polyhedral nanoparticles," *Phys. Rev. Lett.*, vol. 113, p. 165504, Oct 2014.
- [49] B. Liu, T. H. Besseling, A. van Blaaderen, and A. Imhof, "Confinement induced plastic crystal-to-crystal transitions in rodlike particles with long-ranged repulsion," *Phys. Rev. Lett.*, vol. 115, p. 078301, Aug 2015.
- [50] A. S. Karas, J. Glaser, and S. C. Glotzer, "Using depletion to control colloidal crystal assemblies of hard cuboctahedra," *Soft Matter*, vol. 12, pp. 5199–5204, 2016.
- [51] C. R. K. Windows-Yule, B. J. Scheper, W. K. den Otter, D. J. Parker, and A. R. Thornton, "Modifying self-assembly and species separation in three-dimensional systems of shape-anisotropic particles," *Phys. Rev. E*, vol. 93, p. 020901, Feb 2016.
- [52] R. Li, J. Zhang, R. Tan, F. Gerdes, Z. Luo, H. Xu, J. A. Hollingsworth, C. Klinke, O. Chen, and Z. Wang, "Competing interactions between various entropic forces

- toward assembly of pt3ni octahedra into a body-centered cubic superlattice," *Nano Letters*, vol. 16, no. 4, pp. 2792–2799, 2016.
- [53] G. Odriozola and M. Lozada-Cassou, "Entropy driven self-assembly in charged lock–key particles," *The Journal of Physical Chemistry B*, vol. 120, no. 26, pp. 5966–5974, 2016, pMID: 27031174.
- [54] S. Dussi, S. Belli, R. van Roij, and M. Dijkstra, "Cholesterics of colloidal helices: Predicting the macroscopic pitch from the particle shape and thermodynamic state," *The Journal of Chemical Physics*, vol. 142, no. 7, 2015.
- [55] S. Dussi and M. Dijkstra, "Entropy-driven formation of chiral nematic phases by computer simulations," *Nature Communications*, vol. 7, p. 11175, 2016.
- [56] Y. Zhou, R. L. Marson, G. van Anders, J. Zhu, G. Ma, P. Ercius, K. Sun, B. Yeom, S. C. Glotzer, and N. A. Kotov, "Biomimetic hierarchical assembly of helical superparticles from chiral nanoparticles," *ACS Nano*, vol. 10, no. 3, pp. 3248–3256, 2016.
- [57] A. V. Arzola, P. Jákł, L. Chvátal, and P. Zemánek, "Rotation, oscillation and hydrodynamic synchronization of optically trapped oblate spheroidal microparticles," *Opt. Express*, vol. 22, no. 13, pp. 16 207–16 221, Jun 2014.
- [58] S. H. Simpson, D. B. Phillips, O. Brzobohaty, M. Antognozzi, S. Hanna, and P. Zemanek, "Shape adapted optical forces and interactions," in *Optics in the Life Sciences*. Optical Society of America, 2015, p. OtM4E.3.
- [59] S. H. Simpson, L. Chvátal, and P. Zemánek, "Synchronization of colloidal rotors through angular optical binding," *Phys. Rev. A*, vol. 93, p. 023842, Feb 2016.
- [60] I. Kavre, A. Vilfan, and D. c. v. Babič, "Hydrodynamic synchronization of autonomously oscillating optically trapped particles," *Phys. Rev. E*, vol. 91, p. 031002, Mar 2015.
- [61] D. Urzagasti, D. Becerra-Alonso, L. M. Pérez, H. L. Mancini, and D. Laroze, *Hyper-Chaotic and Chaotic Synchronisation of Two Interacting Dipoles*. Cham: Springer International Publishing, 2016, pp. 261–272.
- [62] M. P. Allen and D. J. Tildesley, *Computer Simulation of Liquids*. Oxford Science Publications, 1986.
- [63] R. Evans, "The nature of the liquid-vapour interface and other topics in the statistical mechanics of non-uniform, classical fluids," *Advances in Physics*, vol. 28, no. 2, pp. 143–200, 1979.
- [64] U. M. B. Marconi and P. Tarazona, "Dynamic density functional theory of fluids," *The Journal of Chemical Physics*, vol. 110, no. 16, pp. 8032–8044, 1999.

- [65] —, “Dynamic density functional theory of fluids,” *Journal of Physics: Condensed Matter*, vol. 12, no. 8A, p. A413, 2000.
- [66] A. J. Archer and M. Rauscher, “Dynamical density functional theory for interacting brownian particles: stochastic or deterministic?” *Journal of Physics A: Mathematical and General*, vol. 37, no. 40, p. 9325, 2004.
- [67] E. V. Novak, E. S. Pyanzina, and S. S. Kantorovich, “Behaviour of magnetic janus-like colloids,” *Journal of Physics: Condensed Matter*, vol. 27, no. 23, p. 234102, 2015.
- [68] J. E. Martin, R. A. Anderson, and C. P. Tigges, “Simulation of the athermal coarsening of composites structured by a biaxial field,” *The Journal of Chemical Physics*, vol. 108, no. 18, pp. 7887–7900, 1998.
- [69] —, “Thermal coarsening of uniaxial and biaxial field-structured composites,” *The Journal of Chemical Physics*, vol. 110, no. 10, pp. 4854–4866, 1999.
- [70] F. Smallenburg and M. Dijkstra, “Phase diagram of colloidal spheres in a biaxial electric or magnetic field,” *The Journal of Chemical Physics*, vol. 132, no. 20, 2010.
- [71] S. Jäger and S. H. L. Klapp, “Pattern formation of dipolar colloids in rotating fields: layering and synchronization,” *Soft Matter*, vol. 7, no. 14, pp. 6606–6616, 2011.
- [72] J. E. Martin, E. Venturini, J. Odinek, and R. A. Anderson, “Anisotropic magnetism in field-structured composites,” *Phys. Rev. E*, vol. 61, pp. 2818–2830, Mar 2000.
- [73] M. E. Leunissen, H. R. Vutukuri, and A. van Blaaderen, “Directing colloidal self-assembly with biaxial electric fields,” *Advanced Materials*, vol. 21, no. 30, pp. 3116–3120, 2009.
- [74] T. C. HALSEY, R. A. ANDERSON, and J. E. MARTIN, “The rotary electrorheological effect,” *International Journal of Modern Physics B*, vol. 10, no. 23n24, pp. 3019–3027, 1996.
- [75] S. H. L. Klapp and M. Schoen, *Reviews in Computational Chemistry, Volume 24*, T. R. C. Kenny B. Lipkowitz, Ed. John Wiley & Sons, Inc., 2007.
- [76] D. Frenkel and B. Smit, *Understanding Molecular Simulation, Second Edition*. Elsevier, 2002.
- [77] D. Fincham, “Leapfrog rotational algorithms,” *Molecular Simulation*, vol. 8, no. 3-5, pp. 165–178, 1992.
- [78] J. Dhont, *An Introduction to Dynamics of Colloids, First Edition*. Elsevier Science, 1996.

-
- [79] Z. Wang, C. Holm, and H. W. Müller, "Molecular dynamics study on the equilibrium magnetization properties and structure of ferrofluids," *Phys. Rev. E*, vol. 66, p. 021405, Aug 2002.
- [80] N. Metropolis, A. W. Rosenbluth, M. N. Rosenbluth, A. H. Teller, and E. Teller, "Equation of state calculations by fast computing machines," *The Journal of Chemical Physics*, vol. 21, no. 6, pp. 1087–1092, 1953.
- [81] J. A. Moreno-Razo, E. Diaz-Herrera, and S. H. L. Klapp, "Computer simulations of strongly interacting dipolar systems: performance of a truncated Ewald sum," *Molecular Physics*, vol. 104, no. 18, pp. 2841–2854, SEP 20 2006.
- [82] T. A. Prokopieva, V. A. Danilov, S. S. Kantorovich, and C. Holm, "Ground state structures in ferrofluid monolayers," *Phys. Rev. E*, vol. 80, p. 031404, Sep 2009.
- [83] J. Donaldson, E. Pyanzina, E. Novak, and S. Kantorovich, "Anisometric and anisotropic magnetic colloids: How to tune the response," *Journal of Magnetism and Magnetic Materials*, vol. 383, pp. 267 – 271, 2015, selected papers from the sixth Moscow International Symposium on Magnetism (MISM-2014).
- [84] J. Yan, S. C. Bae, and S. Granick, "Colloidal superstructures programmed into magnetic janus particles," *Advanced Materials*, vol. 27, no. 5, pp. 874–879, 2015.
- [85] D. Wei and G. N. Patey, "Orientational order in simple dipolar liquids: Computer simulation of a ferroelectric nematic phase," *Phys. Rev. Lett.*, vol. 68, pp. 2043–2045, Mar 1992.
- [86] ———, "Ferroelectric liquid-crystal and solid phases formed by strongly interacting dipolar soft spheres," *Phys. Rev. A*, vol. 46, pp. 7783–7792, Dec 1992.
- [87] P. G. Kusalik, "Computer simulation results for the dielectric properties of a highly polar fluid," *The Journal of Chemical Physics*, vol. 93, no. 5, pp. 3520–3535, 1990.
- [88] M. J. Stevens and G. S. Grest, "Structure of soft-sphere dipolar fluids," *Phys. Rev. E*, vol. 51, pp. 5962–5975, Jun 1995.
- [89] A. Pikovsky, M. Rosenblum, and J. Kurths, *Synchronization: A Universal Concept in Nonlinear Sciences*. Cambridge University Press, New York, 2001.
- [90] S. H. Strogatz, *Nonlinear Dynamics And Chaos: With Applications To Physics, Biology, Chemistry, And Engineering*. West View Press, 2001.
- [91] M. E. Tuckerman, *Statistical Mechanics: Theory and Molecular Simulation*. Oxford University Press, USA, 2010.

- [92] M. Mazars, "Bond orientational order parameters in the crystalline phases of the classical yukawa-wigner bilayers," *EPL (Europhysics Letters)*, vol. 84, no. 5, p. 55002, 2008.
- [93] M. Rex and H. Löwen, "Dynamical density functional theory for colloidal dispersions including hydrodynamic interactions," *The European Physical Journal E*, vol. 28, no. 2, pp. 139–146, 2009.
- [94] B. D. Goddard, A. Nold, N. Savva, G. A. Pavliotis, and S. Kalliadasis, "General dynamical density functional theory for classical fluids," *Phys. Rev. Lett.*, vol. 109, p. 120603, Sep 2012.
- [95] B. D. Goddard, A. Nold, N. Savva, P. Yatsyshin, and S. Kalliadasis, "Unification of dynamic density functional theory for colloidal fluids to include inertia and hydrodynamic interactions: derivation and numerical experiments," *Journal of Physics: Condensed Matter*, vol. 25, no. 3, p. 035101, 2013.
- [96] R. Weeber, S. Kantorovich, and C. Holm, "Deformation mechanisms in 2d magnetic gels studied by computer simulations," *Soft Matter*, vol. 8, pp. 9923–9932, 2012.
- [97] S. D. Peroukidis, K. Lichtner, and S. H. L. Klapp, "Tunable structures of mixtures of magnetic particles in liquid-crystalline matrices," *Soft Matter*, vol. 11, pp. 5999–6008, 2015.
- [98] V. Yannopapas, S. H. Klapp, and S. D. Peroukidis, "Magneto-optical properties of liquid-crystalline ferrofluids," *Opt. Mater. Express*, vol. 6, no. 8, pp. 2681–2688, Aug 2016.
- [99] S. D. Peroukidis and S. H. L. Klapp, "Orientational order and translational dynamics of magnetic particle assemblies in liquid crystals," *Soft Matter*, vol. 12, pp. 6841–6850, 2016.
- [100] K. May, A. Eremin, R. Stannarius, S. D. Peroukidis, S. H. L. Klapp, and S. Klein, "Colloidal suspensions of rodlike nanocrystals and magnetic spheres under an external magnetic stimulus: Experiment and molecular dynamics simulation," *Langmuir*, vol. 32, no. 20, pp. 5085–5093, 2016, pMID: 27119202.
- [101] S. D. Peroukidis and S. H. L. Klapp, "Spontaneous ordering of magnetic particles in liquid crystals: From chains to biaxial lamellae," *Phys. Rev. E*, vol. 92, p. 010501, Jul 2015.